Plasma actuators for separation control – design and application

by

Julie A. Vernet

November 2014
Technical Reports from
Royal Institute of Technology
KTH Mechanics
SE-100 44 Stockholm, Sweden

Akademisk avhandling som med tillstånd av Kungliga Tekniska Högskolan i Stockholm framlägges till offentlig granskning för avläggande av teknologie licentiatsexamen den 19 december 2014 kl 10.30 i sal E2, Lindstedsvägen 3, Kungliga Tekniska Högskolan, Stockholm.

TRITA-MEK 2014:25
ISSN 0348-467X
ISRN KTH/MEK/TR-14/25-SE
ISBN 978-91-7595-354-0

Universitetsservice US–AB, Stockholm 2014

To my grandfather

who taught me his own interpretation of the Archimedes principle
"A body immersed or partially immersed in water ... gets wet!"

Julie A. Vernet 2014, **Plasma actuators for separation control – design and application**

Linné Flow Centre, KTH Mechanics, SE–100 44 Stockholm, Sweden

Abstract

This thesis deals with the experimental realisation of an active flow control technique, that utilises dielectric barrier discharge (DBD) plasma actuators, to re-energise boundary layers subjected to adverse pressure gradients. The ultimate goal of the research is to delay flow separation occurring on the A-pillar of trucks tractors within the Flow Research on Advanced and Novel Control Efficiency (FRANCE) project.

The first part of the project consists of the development of manufacturing techniques for in-house built DBD plasma actuators and to evaluate their performance when placed on a curved surface. The behaviour and parameter dependence of the electric wind in quiescent air were investigated by means of Laser Doppler velocimetry (LDV). The electric wind was found to develop similar to a wall jet and the results of the parametric study are in agreement with the literature, *viz.* increase of wind velocities with increasing driving voltage and frequency and with decrease of dielectric sheet thickness. The measured evolution of the induced wall jets served also as a benchmark data base for a companion numerical project. Furthermore, during the two half-periods (strokes) of the alternating current, the electric wind was investigated through phase-resolved LDV data, which revealed that while the velocity during both strokes remains positive, it differs in magnitude with nearly a factor of two between the strokes. Since the phase dependence of the electric wind is observed only in the vicinity of the actuator, the assumption of a steady induced force in simulations seems to be justified.

For the second part of the project, a double DBD plasma actuator was used to control flow separation occurring on a cylindrical bump approached by a turbulent boundary layer. The uncontrolled flow that develops on the flat plate upstream the bump, separating on the half-cylinder geometry and reattaching on the downstream flat plate was characterised using hot-wire anemometry. Finally, detailed pressure measurements at the wall and in the wake of the cylinder showed that the double actuator was able to reduce the reattachment length downstream the cylindrical bump which resulted in a drag reduction up to 30% when the actuator was placed a few millimetres upstream the separation point. However, drag reduction was observed for a wide range of actuator positions and it is hypothesised that the measured reduction could be due to different mechanisms, either as a re-energising of the shear-layer or as addition of momentum close to the wall thereby delaying separation and increasing the base pressure on the backside of the half-cylinder.

Descriptors: electric wind, drag reduction, wind-tunnel experiments

Julie A. Vernet 2014, **Plasmaaktuatorer för separationskontroll – design och tillämpning**

Linné Flow Centre, KTH Mekanik, SE–100 44 Stockholm, Sweden

Sammanfattning

En undersökning av strömningskontroll med sk DBD plasmaaktuatorer för att påverka avlösningen av ett turbulent gränsskikt i en positiv tryckgradient har utförts. Det slutgiltiga målet för forskningen är att försena eller i bästa fall förhindra avlösning av strömningen vid A-stolpen på en långtradares dragbil och forskningen görs som en del inom projektet FRANCE (Flow Research on Advanced and Novel Control Efficency).

En tillverkningsteknik tagits fram för att bygga DBD plasmaaktuatorer som kan placeras på en krökt yta. Den elektriska vind som aktuatorerna ger upphov till har bestämts med laser Doppler velocimetri (LDV) i stillastående omgivande luft och hastighetsfältet längs den krökta ytan kartlagts. Resultaten visar att vinden uppför sig likartat med vad som tidigare rapporterats i litteraturen, nämligen en ökning av hastigheten med ökande drivspänning och frekvens och också en ökning när tjockleken av det dielektriska materialskiktet minskas. Fasupplösta mätningar med LDV visade att både de positiva och negativa halvperioderna av den drivande växelspänningen ger samma riktning av vinden, dock med en skillnad i den maximala hastigheten med en faktor två. Vindens fasberoende observerades dock bara i närheten av aktuatorerna och i simuleringar antas en stationär inducerad kraft vilket därför kan anses vara en god approximation. Resultaten har också använts för att kalibrera en modell för aktuatorerna i ett parallellt numeriskt projekt inom FRANCE

Två plasmaaktuatorer i en dubbel (tandem) konfiguration har använts för att påverka avlösningen på en halvcylinder som anströmmas längs en plan yta med ett turbulent gränsskikt. Basströmningen, dvs strömningen utan kontroll, framför, över och nedströms cylindern, har kartlagts med hjälp av varmtrådsanemometri. Detaljerade tryckmätningar på ytorna och i vaken nedströms cylindern visade att med strömningskontroll kunde längden på det avlösta området minskas, bastrycket på nedströmssidan av cylindern ökas och det totala motståndet minskas med 30% för den bästa placeringen av aktuatorn (ett par mm uppströms avlösningslinjen). Minskningen kunde emellertid observeras för ett brett intervall av positioner och uppvisade två områden med lokalt maximal effekt. En hypotes är att detta kan bero på att två olika mekanismer är verksamma, i ena fallet genom att aktuatorn ger extra rörelseenergi till själva strömningen utan att direkt påverka avlösningen, och i andra fallet genom att tillföra rörelsemängd nära ytan och som förskjuter avlösningen på cylindern nedströms och därmed minskar det avlösta området.

Nyckelord: elektrisk vind, motståndsminskning, vindtunnel experiment

Preface

In this licentiate thesis, the capability of Dielectric Barrier Discharge plasma actuators to control flow separation is experimentally investigated. The thesis is divided into two parts. The first part gives an introduction and motivations for the project together with prerequisite concepts concerning plasma actuators. The different experimental setups and measurement techniques employed are also described together with a summary of the results. Finally, a conclusion section with discussion of the results and plans for the next two years is ending this part. The second part consists of three papers giving more details to the reader about the observations made and results obtained during this project.

November 2014, Stockholm
Julie A. Vernet

Contents

Part I

Overview and summary

CHAPTER 1

Introduction

Put next to each other one electron and a 36 tons truck-trailor combination. Can you imagine that accelerating this electron is actually gonna be able to improve the aerodynamics of the truck? Crazy, right?

1.1. Motivations

Bradley (2000) stated in the technical report from the US department of Energy that reducing the aerodynamic drag of heavy-trucks (36 tons tractor-trailer combination with american-type tractor driving on a level road at 105 km/h) of 20% would imply 4% saving of their fuel consumption considering that the total losses of such type of trucks is due to:

- engine losses (60%),
- aerodynamic losses (21%),
- rolling resistances (13%),
- other losses (6%) such as driveline and accessories losses.

In the case of a European 40 tons tractor-semitrailer combination at 85 km/h on level road, the numbers are similar as it is 18% of the total energy losses that accounts for the aerodynamic losses (aerodynamic drag)[1].

The Flow Research on Advanced and Novel Control Efficiency (FRANCE) project has been initiated with the final aim of decreasing the aerodynamic drag of heavy-duty trucks. This study is about experimental work on control methods to reduce the aerodynamic drag while a companion project aims at using Large Eddy Simulations (LES) to model the control and simulate the flow case.

1.2. Flow separation and control

Flow separation is a common term for describing the flow when the external streamlines depart from the surface of a body. Two general types of separation can be distinguished, separation on a surface without abrupt geometry changes under an adverse pressure gradient (APG) or when a flow separates at a sharp corner (geometry induced separation). There are also combinations of these two

[1]Personal communication with Dr. Per Elofsson, Senior Technical Manager, Aerodynamics, Scania CV AB.

effects such as the separation on a circular cylinder, where both the curvature and the adverse pressure gradient play a role.

The pressure term on the right-hand side of the Navier-Stokes equation comes from the fact that a difference of pressure in a flow is exerting a force on that flow. In case of a pressure decrease along the streamwise direction – a so called Favorable Pressure Gradient (FPG) – the flow is accelerated and thus gains in kinetic energy (Barnard 2009). In the case of a pressure increase – Adverse Pressure Gradient (APG) – the flow instead looses kinetic energy and may separate from the surface (Simpson 1996). The flow close to the surface is then driven by the pressure gradient and thus moves in the opposite direction to the external flow. In case of a turbulent boundary layer the mixing between the higher and lower velocities in the boundary layer provides more kinetic energy to the boundary layer making it more resistant to the APG and thus separating further downstream than an equivalent laminar boundary layer. If the separation region extends up to a FPG, the flow is accelerated again and gains back the kinetic energy; the flow is thus reattaching, all flow particles are again flowing in the positive streamwise direction.

In this work we are mainly interested in the combination of geometry and pressure-gradient induced separation and are exploring possible methods to reduce separation and thereby reduce drag in practical applications. There are several methods that are possible to use to delay separation or to shorten the reattachment length. One such method is to use suction at the surface (see e.g. Fransson *et al.* 2004), another method uses vortex generators or blowing at the wall (see e.g. Lögdberg *et al.* 2010) to create streamwise oriented vortices that increase the vertical mixing in the region close to the surface. A third method works by adding streamwise momentum at the wall itself through a wall slot as a wall jet or, as will be described in the present work, through an electric wind, created by a plasma actuator.

1.3. Heavy trucks aerodynamics

Tractor-trailer combination trucks are undoubtedly bluff bodies due to their large frontal area and large base area. Their rectangular shape was developed to optimize their capacity for the purpose of goods transportation within the overall vehicle length regulations.

One of the main contributor to the aerodynamic drag of a tractor-trailer combination is the pressure loss at the base of the trailer due to the strong separation occurring there and resulting in a large wake with a low pressure (responsible for 25% of the total aerodynamic drag according to Wood 2006). Other projects are nowadays investigating the structure of the wake of bluff bodies and developing techniques to reduce the induced drag and noise (as an example see Trip 2014).

Interaction of vortices created by the airflow separating around the wheel and the wheel housing as well as the underbody flow of the truck is the most important source of aerodynamic drag (30% according to Wood 2006) and has been studied to optimize for instance the shape of the wheel housing (Söderblom *et al.* 2009). The rotation of the wheels and the relative movement between the truck underbody and the ground (*i.e.* the moving ground cannot be neglected here) makes this flow particularly complex to investigate (Söderblom *et al.* 2012).

Finally the remaining 45% of the aerodynamic drag are induced by the tractor and the flow in the gap between the tractor and the trailer (Wood 2006). The unavoidable geometric separation between the tractor and the trailer is obviously creating a strong separation and thus drag which is nowadays reduced using cab deflectors for instance (Choi *et al.* 2014).

In the 1980's, the sharp corners forming the A-pillars and corner panels were changed for rounded corners, which later evolved in the shape that can be found on today's trucks (see figure 1.1). Indeed, while in presence of a sharp corner, the flow will automatically separate at the location of the corner if it has not separated earlier as explained above. With the rounded corners, aerodynamicists were able to control to some extent the separation but also

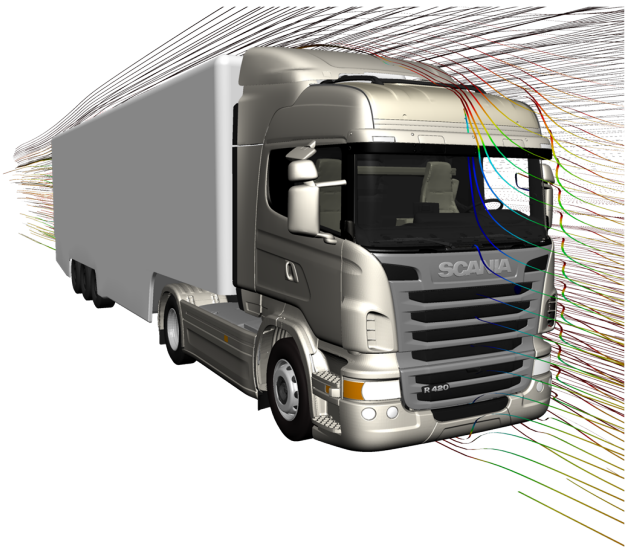

FIGURE 1.1. Velocity streamlines on a truck cabin. Personal communication with Guillaume Mercier, Senior Engineer, Aerodynamics, Scania CV AB.

make the pressure distribution around the front better from the point of view of form drag. A complication is that the flow approaching the truck usually is not oriented along the longitudinal axis of the vehicle; the angle between the vehicle axis and the wind direction is called the yaw angle. Moreover, the direction or the intensity of the wind might not be uniform along the vertical direction and that may also make the yaw angle change with the height of the vehicle. Passive control techniques – techniques that do not need input of energy to work – as for instance the rounded corners cannot adapt to changes of the yaw angle and are developed for optimised control in case of zero or small yaw angles (Barnard 2009). The use of active flow control techniques – techniques that do require energy to work – open the possibility for feedback control (called reactive control by Gad-el Hak 2000) could allow aerodynamicists to adapt the separation control for a wider variation of the yaw angle.

For the first part of this project a geometric model with a half-cylinder protruding from a flat plate will be used. This model was chosen as the separation is triggered by a curved surface and no vortex shedding is induced downstream the half-cylinder due to the presence of the flat plate as in the case of the A-pillar. Dielectric Barrier Discharge (DBD) plasma actuators have shown interesting results for separation control on generic geometries such as cylinders and airfoils (see chapter 2) and will be used here to reduce the separation occurring on the half-cylinder.

1.4. Layout of the thesis

This thesis is organized in two parts. The first part starts with a description of plasma actuators and a review on both the electric wind they induce as well as previous studies realized on separation control by means of DBD plasma actuation (chapter 2). Chapter 3 summarizes the experimental setup and experimental techniques used to investigate the electric wind induced by the in-house built DBD plasma actuators on the surface of a cylinder. The baseline case of the flow separation occurring on a half-cylinder protruding from a flat plate and the results on the separation region reduction using a double DBD plasma actuator on top of the half-cylinder as well as the experimental setup and techniques employed are discussed in chapter 4. Conclusions about the achievements of the first part of this project as well as future work planned for the second part of the project are given in chapter 5. The second part of the thesis contains papers, with two of them submitted to journals, following the order of the first part with Paper 1 investigating mean and phase-averaged measurements of the induced electric wind. Paper 2 is the study of the effect of the flow developing upstream, on top and downstream a cylindrical bump, while Paper 3 shows the achievement of drag reduction by reduction of the separation region downstream the half cylinder.

CHAPTER 2

History, principle and review of plasma actuators

It is Langmuir (1928) who first used the term plasma to identify the fourth state of matter consisting in an ionized gas. He identified this matter as containing an almost equal number of ions and electrons and hence being nearly zero space charged[2]. He thought about a medium thus entraining ions, electrons and other neutral atoms and that reminded him of the blood plasma which is the fluid entraining the blood cells. Nowadays the analogy can not be made anymore as it was identified that there is no entraining medium, but the term plasma remained (Bellan 2008). Plasma is found in nature as it composes most of the stars of the Universe, lightning flashes during thunderstorms and northern lights for example. It is also broadly used in the industry and studied in laboratories for applications as ozone production, welding, sterilization, plasma TVs ... and nowadays flow control.

In the presence of a high-electric field, electrons can be directly extracted from metallic surfaces – electrodes – due to the quantum-mechanical effect called tunneling[3] as explained by Fridman (2008). These electrons are the primary electrons. Then, the most common gas ionization process is the so-called direct ionization by electron impact: electrons ionize neutral molecules by colliding with them and providing energy to one of their valence electrons. The valence electron becomes more excited and if the amount of energy is high enough it is released hence forming two electrons and a positively charged ion. When more and more electrons are produced by successive collisions, it is a discharge (so called Townsend[4]) mechanism or electron avalanche (Moreau 2007). Other mechanisms of ionization are present in the plasma as well as phenomena of electron attachments producing then negatively charged ions.

[2]The space charge of a space region is the resulting electric charge of the region considering the number of positively charged species, as positively charged ions, and negatively charged species, as negatively charged ions and electrons.
[3]The barrier keeping electrons in the atomic state known as the work function, here of the metallic material of the electrode, becomes thinner in presence of the high electric field and electrons tunnel though the barrier. This is called a cold emission or field emission as opposed to the thermionic emission for which the electrode temperature is strongly increased and the thermal energy of the electrons becomes high enough for them to cross the barrier. The Schottky emission is a combination of the field and thermionic emissions.
[4]From Sir John Sealy Edward Townsend (1868–1957).

2.1. Plasma actuators for flow control?

The two most common plasma actuators used for low-speed flow control purposes are the corona plasma actuator and the Dielectric Barrier Discharge (DBD) plasma actuator. Such actuators have the particularity to transform electrical power into mechanical power without the need for moving mechanical parts.

These actuators produce a plasma often characterized as non-thermal, weakly ionized plasma. The temperature of the electrons is much higher than that of the ions and usually expressed in electron volts (eV) which is a measure of the energy contained in the electron charge (1 eV $\sim 1.6\times10^{-19}$ J). To be converted to an actual temperature unit, as Kelvin (K), the Boltzmann constant (k_B) is used: 1 eV/k_B $\sim$ 11605 K. When colliding with an ion, the electron transmits part of its energy thus increasing the temperature of the ion, while decreasing its own. Because its mass is much smaller than that of the ions only a small part of its energy, *i.e.* temperature, is transmitted. Thus, to be able to reach a temperature equilibrium between the electrons and ions, multiple collisions are needed and the bulk temperature of the plasma can reach several thousands Kelvin. If the discharge is too short in time, there will not be enough collisions happening to reach the temperature equilibrium between the ions and the electrons and the plasma will be classified as a non-thermal plasma; the temperature of the electrons remaining much higher than that of the ions.

When the ionization degree of the plasma is low, *i.e.* the concentration of ions and electrons is low compared to the concentration of neutral particles, the plasma is qualified as a weakly ionized plasma. Then, in the case of a non-thermal, weakly ionized plasma, the concentration of electrons and ions is smaller than the concentration of neutral particles and the temperature of the ions remains low and close to the neutral particles temperature which are at room temperature. Thus the bulk temperature of the plasma is actually only a few degrees higher than the surrounding room temperature.

Jukes *et al.* (2008) measured an increase of the plasma temperature up to 108°C using a thermal camera. During this project an infrared camera has been used to evaluate the temperature of the plasma induced by our in-house plasma actuators described in chapter 3 after the actuator was used continuously for five minutes (see figure 2.1). The maximum temperature was noticed in the plasma region and was approximately 18 K above the room temperature. Moreover, the temperature of air and surface only few centimeters away from the plasma region remained equal to the ambient temperature.

Corona plasma actuators and DBD plasma actuators will be presented here in their most common shape, the straight shape using straight electrodes.

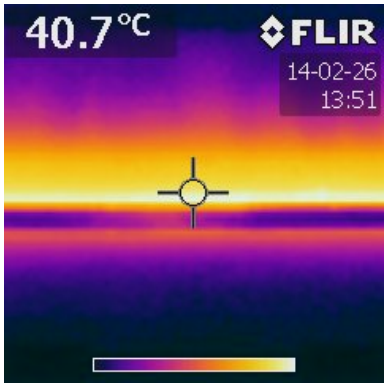

FIGURE 2.1. Photography taken with an infrared camera 5 minutes after turning the DBD plasma actuator on. The crosshair is on top of the plasma region, the plasma expanding towards the top of the picture. The colour scale represents temperatures from 23 to 41°C.

2.1.1. *Corona plasma actuators*

The first type of plasma actuator, so-called corona plasma actuator, consists of two electrodes directly disposed on the surface of the geometrical model for which the flow control study is conducted (see figure 2.2*a)*).

A plasma discharge – called corona discharge – is produced between the electrodes by applying a high-voltage direct current (DC). If the difference of potential between the two electrodes is high enough to overcome the electrical insulation resistance of the medium (usually atmospheric air) above the plate, the air breaks down and becomes a conductor. Electrons are extracted from the cathode – electrode exposed to a high-negative voltage – as explained above and start to travel towards the anode – higher voltage exposed electrode or grounded electrode – to close the electrical circuit. The plasma appears steady but is actually created by a succession of short time-scale discharges. The movement of electons from one electrode to the other creates a movement of positive ions in the opposite direction which is by convention the direction of the electric current. Because the plasma is weakly-ionised as explained above, the induced current is small. Although a high-voltage is needed to initiate and sustain the plasma, the power consumption of such actuators therefore remains low. Finally, during their travel the electrons induce direct ionizing of the neutral particles of air close to the model surface by electron impact and thus repulsing ions. As the mass of ions is much higher than the electrons mass, it is their movement that is inducing momentum to the air close to the surface creating a flow similar to a wall jet; called the electric wind or ionic wind. Velocities of the induced electric wind up to 3 m/s were recorded by

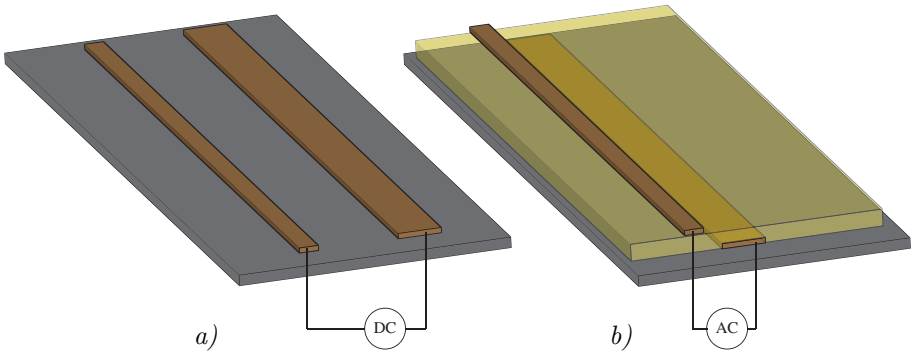

FIGURE 2.2. Schematic of *a)* a plate-to-plate corona plasma actuator and *b)* a plate-to-plate dielectric barrier discharge actuator. The grey plate is a representation of the model surface on which the actuator is applied to. The brown plates are the plate-electrodes and the yellow part in *b)* is the dielectric sheet.

Mestiri *et al.* (2010). The force produced by the actuator is thus qualified as an electrohydrodynamic (EHD) force (Moreau *et al.* 2013).

The electrodes can consist of two plate electrodes – plate-to-plate arrangement – as in figure 2.2*a)* but also in a wire-to-plate or wire-to-wire arrangement. In the case of corona plasma actuators the relative size between the electrodes has a great influence on the electric wind produced and it is usually chosen to have a smaller – in height for plate electrodes or in diameter for wired electrodes – anode than the cathode to get essentially positive ions traveling, in opposite direction to the electrons, and hence an electric wind oriented from the small to the large electrode (Labergue 2005).

Laminar boundary layer control was achieved by Velkoff & Ketcham (1968) as they used corona wires and delayed the transition position by 0.15 ft (46 mm). Leger *et al.* (2001) showed drag reduction by reducing the wake size and thus controlling a separated flow using a wire-to-plate corona plasma actuator on an inclined flat plate. Few years later Labergue *et al.* (2004) investigated the influence of the EHD force on the flow above an inclined plate downstream a flat plate. They were able to reattach a naturally detached flow but also detach a naturally attached flow. The corona actuator was even more effective in detaching attached flows than attaching detached flows as it could be achieved for higher freestream velocities. This effect was realized by applying electric wind in either the same direction than the freestream flow or in the reverse direction thus accelerating or decreasing velocities at the wall (Moreau *et al.* 2006).

The number of publications about flow control studies with corona plasma actuators is relatively small since those actuators have the disadvantages of being unstable. Indeed as the voltage difference between the electrodes is increased, a filamentary regime leading to spark formations between the electrodes is easily reached. As a consequence, the actuator loses in efficiency as heat losses increase and damages of the actuator can occur. However, by placing a dielectric sheet between the electrodes improves the stability of the actuator discharge by preventing sparks. Such plasma actuators are called Dielectric Barrier Discharge (DBD) plasma actuators (see figure 2.2*b)*) and are the subject of the following part. For more details about the corona discharge and their use, the reader is referred to the extended review of Moreau (2007).

2.1.2. *Dielectric barrier discharge plasma actuators*

A common single DBD actuator is made of two electrodes asymmetrically disposed on the top and below a dielectric material (see figure 2.2*b)*). A dielectric material is an isolator which also has the property of being polarized when placed in an electric field, *i.e.* the electric charges inside the material will slightly move under the influence of the electric field, causing them to be polarized. The two important parameters of a dielectric material are thus its isolation property, *i.e.* its dielectric strength, which is the maximal voltage the material can sustain before the current goes through the material and its polarization property, *i.e.* its relative permittivity also called the dielectric constant (usually referred as ϵ_r).

Usually the actuator is placed on a geometrical model and the top electrode is thus named the exposed electrode while the second one is the embedded electrode. In that case, the plasma will form in the vicinity of the dielectric surface from the edge of the exposed electrode on the side where the bottom electrode is present. In the case where the actuator is not applied on a surface, a plasma will form on both sides of the dielectric sheet.

To sustain the plasma formation, contrary to the corona actuator, a high-frequency, high-voltage alternating current (AC) needs to be provided to one electrode – usually the exposed one then denoted as the active electrode – while the other electrode is grounded. During one half-period (stroke) of the AC current, the exposed electrode is fed with a negative voltage (negative-going cycle or forward stroke), electrons are released from the exposed electrode due to the tunneling effect as explained earlier and are attracted towards the grounded electrode because of the potential difference. They ionize the neutral particles on their way in a similar way than for the corona actuator (Townsend discharge) and are stopped by the presence of the dielectric material. This discharge phenomenon is usually called a glow or corona discharge since, although it is due to a succession of very short time-scale discharges, the plasma appears to have a uniform glow. As the electrons depose on the dielectric surface the space becomes negatively charged, hence the difference of potential with the

exposed electrode is reduced and after a succession of discharges the mechanism stops. Then, during the second stroke, a positive voltage is applied to the exposed electrode (positive-going cycle or backward stroke) and the electrons are pulled back towards the electrode. This phenomenon is called the secondary emission and thus also creates a plasma with ions moving in the vicinity of the actuator. This discharge phenomenon is usually referred to as a streamer discharge in contrast to the glow discharge. For both types of discharges, in a similar way than for the corona actuator, the plasma is weakly ionized and the current is small keeping the power consumption of the actuator low, although the range of current is slightly different between the two discharges with the streamer discharge producing higher currents than the glow discharge (Debien *et al.* 2012).

With the aim of developing efficient in-house built DBD plasma actuators, a study of the literature was necessary. The following section summarizes literature results on the mean and time-resolved electric wind produced by DBD plasma actuators while the last section shows that interesting results were obtained previously using DBD plasma actuation for flow control on separated flow on geometries such as inclined plates, cylinders and airfoils. For a more detailed review on DBD plasma actuators, their physics and their applications the reader is referred to Moreau (2007), Corke *et al.* (2010) and Benard & Moreau (2014).

2.2. Review of studies on the electric wind induced by DBD plasma actuators

2.2.1. *Optimization of the mean electric wind*

In the following a few examples of the on-going studies of the time-averaged electric wind and/or force produced by DBD plasma actuators are described. Ranges of velocities and thus EHD forces as well as spatial evolutions of the electric wind (wall jet) differ from one study to another due to differences in geometry, driving current parameters and material of the actuators used by the different research groups but the results are usually in agreement.

One of the most extensive and earliest study on the parameters influencing the formation of the electric wind has been performed by Forte *et al.* (2007). Their measurements allow them to optimize the driving current as well as geometrical parameters and produce electric winds with velocities up to 7 m/s in the case of a single DBD and 8 m/s for multiple actuator configurations. They conclude that it is preferential to increase the driving voltage rather than the driving frequency as they noticed that the increase of the electric wind maximum velocity reaches a plateau once the frequency gets too high. Indeed, when the driving frequency is too high, the heat losses in the dielectric material become too important and streamers are noticeable in the discharge plasma.

Thomas *et al.* (2009) measured the thrust produced by actuators at different voltages. They noticed that at low voltages the thrust is linked to the voltage through a power law with a coefficient of 3.5 but as the voltage increases, the coefficient decreases to 2.3. Finally above a certain value – that they denote the saturation voltage – streamers appear in the discharge and only the power consumption of the actuator keeps increasing whereas the thrust remains nearly constant. They also investigated the impact of the dielectric constant – not to be confused with the dielectric strength which should be chosen as high as possible – and showed that actuators built with material with a smaller dielectric constant would have a higher saturation voltage. Those results were confirmed by Soloviev (2012) using a phenomenological model based on the body force induced by the actuator due to the movement of the different species of electrons and ions, negative and positive. Decreasing the dielectric constant would increase the concentration of negative ions which are the main responsible for the body force production.

Kotsonis *et al.* (2011) compared balance measurements to thrust evaluation from velocity measurements and confirmed the power law relation between the thrust and the driving voltage, but a linear relation between the thrust and the driving frequency applied to the actuator also implying that increasing the voltage makes the actuators more efficient than increasing the frequency. The later was also demonstrated by Giepman & Kotsonis (2011), where the efficiency of the actuators defined as the ratio of the mechanical power production to the electrical power consumption of the actuator was studied for different driving voltages and frequencies. In the matter of evaluating different methods to evaluate the thrust production from Particle Image Velocimetry (PIV) measurements, Kriegseis *et al.* (2013) show that both the plasma extend and the force domain grow with the driving voltage.

From the literature study, it appears that four geometrical parameters are important to consider in a matter of increasing the efficiency of classical DBD plasma actuators:

- the thickness of the active electrode,
- the width of the grounded electrode,
- the horizontal gap or overlap between the electrodes and
- the dielectric sheet thickness.

Enloe *et al.* (2004) showed that the plasma is directly responsible for the body force induced by the actuator and thus studied the influence of the electrode geometry on the plasma generation. They compared the thrust from DBD plasma actuators with different diameters of the active electrode using wire electrodes and showed that smaller diameters induce a higher force for the same dissipated power. Active electrodes made of flat tapes with lower thicknesses than the wire electrodes are responsible for even higher thrust generation. They also compared the maximum velocities of the electric wind produced by DBD

actuators with grounded electrodes of different widths and showed that the plasma extension and thus the electric wind can be limited by this parameter. However, as the width of the grounded electrode keeps increasing, the expansion of the plasma reaches a plateau and using a larger grounded electrode can be seen as a waste of space while considering arrangements with several actuators in series.

Forte *et al.* (2007) confirm these results and completed them by studying the influence of the gap or overlap of the electrodes. They showed that an actuator with a gap of 5 mm between the electrodes induces the highest velocities of the electric wind, even though the velocity variations for gap configurations between 0 and 5 mm do not differ much. Post & Corke (2004) suggest a small overlap (less than a millimeter) between the electrode do ensure a more uniform plasma formation along the electrodes. Finally, Forte *et al.* (2007) also investigated the effect of the dielectric thickness on the induced electric wind and concluded that a thicker dielectric material can be used for higher driving voltages (as its isolation property is then stronger), but at equal voltage they produce electric winds with lower velocities than thinner dielectrics except at low driving voltages.

Finally, the impact of atmospheric temperature and pressure changes on the plasma actuator performances has also been investigated by Versailles *et al.* (2010), whereas Erfani *et al.* (2012) assessed the influence of the dielectric temperature on the induced flow field.

2.2.2. *Time-resolved studies of the electric wind and understanding of the ions entities role*

As mentioned earlier, an alternating current (AC) high-voltage signal – usually a sine-wave or sawtooth wave – is necessary to sustain the plasma discharge for DBD plasma actuators. This AC voltage is thus a periodic signal, each period divided into two strokes, one stroke during which the voltage is positive – the exposed electrode is the anode – and the other during which a negative voltage is provided to the plasma actuator – the exposed electrode is the cathode. This periodicity has an effect on the plasma discharge, hence the induced electric wind is considered as unsteady and periodic.

Early experimental results on the time-resolved electric wind showed a positive velocity during both the forward and the backward strokes of the driving voltage cycle (Enloe *et al.* 2004). However, simulation studies gave contradictory results at first since only nitrogen gas was considered in the surrounding of the plasma actuator (Boeuf *et al.* 2007). Thus only positive ions were thought to be responsible for the momentum transfer and these are mainly present during the backward stroke. Kim *et al.* (2007) and Leonov *et al.* (2010) compared electric wind speeds during the two strokes in the presence of air or only nitrogen gas and showed the importance of the negative ions in

the momentum transfer action of the plasma actuators. Indeed, in the case of only nitrogen gas, production of negative ions is not possible, positive ions are mainly produced during the backward stroke and almost no momentum is transferred to the surrounding during the forward stroke. When the medium is air, the forward stroke appears to produce more momentum than the backward stroke highlighting the importance of the negative ions in high concentration during that phase. Simulations of Boeuf *et al.* (2009) confirm those results showing that there are more negative ions during the forward stroke and more positive ions during the backward strokes. Experiments of Thomas *et al.* (2009) and simulations of Soloviev (2012) also highlight the importance of the role of the negative ions in the momentum production process. The results of those studies explain that even though the electrons are moving in different directions during the two strokes, the electric wind production is due to ions with different polarities and thus always in the same direction.

A new challenge of the study of the electric wind is to determine if, even though the electric wind always flows in the same direction, the body force, the so-called EHD force induced by the electric wind, is always in the same direction. Most groups working on that question utilize the definition of Corke *et al.* (2010) to characterise the body force induced by their plasma actuators in the streamwise direction: the force is characterised by a 'push' if it is directed in the positive streamwise direction, thus away from the exposed electrode, and as a 'pull' if it is in the negative streamwise direction. Two types of actuator behaviours emerged from recent studies, although there seem to be a consensus that the forward stroke is producing a strong 'PUSH' – where the capital letters emphasize the fact that the amplitude of the force is stronger – they disagree whether the backward stroke is producing a 'push' or a 'pull'. The studies of Leonov *et al.* (2010) and Neumann *et al.* (2012) show a PUSH-pull behavior, whereas Debien *et al.* (2012) compared DBD plasma actuators built with different electrode geometries and concluded that the type of EHD force produced by the plasma is dependent on the top electrode shape: plate-shape exposed electrodes induce a PUSH-pull force while a wire-shape exposed electrode yields a PUSH-push behavior. Moreover, they notice that in the case of the wire-to-plate configuration, the PUSH is produced during the positive-going stroke of the AC voltage. Kotsonis & Ghaemi (2011) show that the type is dependent on the driving voltage waveform, obtaining a PUSH-push force in the case of a sine wave and a positive sawtooth signal, a PUSH-pull force for the square wave and a PUSH-none force for the negative sawtooth signals. Many other studies, both experimental and numerical classified their actuators as a PUSH-push behavior as *e.g.* Likhanskii *et al.* (2008), Enloe *et al.* (2009) and Nishida *et al.* (2012). For a summary of some of the most important studies on the induced force behavior of DBD plasma actuators, see table 1.

Author(s) (year)	Measurement technique	Measured quantities	Induced streamwise force	
Forte *et al.* (2007)	LDV	u_e, v_e	PUSH-push*	
Likhanskii *et al.* (2008)	Simulation		PUSH-push	
Boeuf *et al.* (2009)	Simulation		PUSH-push	
Enloe *et al.* (2009)	Laser interferometry	$\theta^{(1)}$	PUSH-push	
Leonov *et al.* (2010)	Time-res. Pitot	p	PUSH-pull*	(classic DBD)
			PUSH-pull*	(only Nitrogen gas)
			PUSH-push*	(electrode with tip)
Kotsonis & Ghaemi (2011)	PIV	u_e, v_e	PUSH-push	(sine, pos. sawtooth)
			PUSH-none	(neg. sawtooth)
			PUSH-pull	(square wave)
Debien *et al.* (2012)	PIV	u_e, v_e	PUSH-push	(wire-to-plate)
			PUSH-pull	(plate-to-plate)
Neumann *et al.* (2012)	LDV-profile sensor	u_e, v_e, $a_{e,x}$, $a_{e,y}$	PUSH-pull	
Nishida *et al.* (2012)	Simulation		PUSH-push	
Benard *et al.* (2013)	PIV	u_e, v_e	PUSH-push	

TABLE 1. Previous studies on the behaviour of the force induced in the streamwise direction by DBD plasma actuators where u_e and v_e denote the velocity components in the streamwise and wall-normal direction, respectively, and $a_{e,x}$ and $a_{e,y}$ the acceleration in the streamwise and wall-normal direction, respectively. The superscript * indicates that the direction of the force is not stated explicitly in the respective paper, but had to be inferred from the results. $^{(1)}\theta$ represents here the angular position of the pendulum studied by Enloe *et al.* (2009).

2.3. Applications of DBD plasma actuators to flow control

As Roth (2007) illustrates, interest in flow control using plasma actuators has been exponentially growing during the past twenty years, in particular in the aeronautical community.

Before reviewing some of those numerous studies, it is important to know that among the studies two different geometries of DBD plasma actuators have mainly been used for flow control: DBD plasma actuators or DBD plasma-array actuators with the plasma oriented in the spanwise direction and DBD plasma-array actuators for which plasma are oriented in the streamwise direction as can been seen in figure 2.3.

Moreover, DBD plasma actuators can be used in steady or pulsed mode. The steady mode term is used when the AC high-voltage is fed to the active electrode continuously. As seen before the electric wind produced by the actuator is then unsteady but its frequency is higher than flow-related frequencies, *i.e.* the flow experiences the actuation as a steady actuation. The pulsed mode consists in multiplying the high-frequency AC waveform to a waveform (usually a square wave) with a lower frequency (called the modulation or pulsed frequency f_m) producing an ON/OFF effect of the actuation. When starting a DBD plasma actuator with electrodes along the spanwise direction, it first produces a vortex (with its axis in the spanwise direction) called the starting vortex (Jukes *et al.* 2006; Kotsonis *et al.* 2011) and after few periods of the high-frequency AC voltage, the electric wind evolves into a wall jet in the streamwise direction as described before. The actuation in pulsed mode which consists in turning the actuator ON or OFF with the frequency f_m usually involves using the starting vortex for the control mechanism rather than the wall jet.

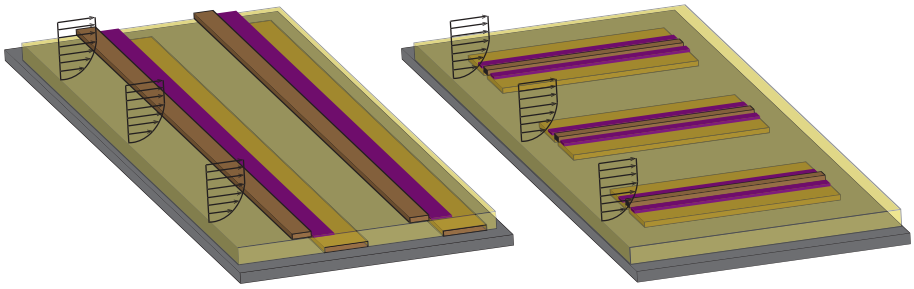

a) *b)*

FIGURE 2.3. Example of *a)* a DBD plasma-array actuator – here double DBD plasma actuator – with plasmas oriented in the spanwise direction and *b)* a DBD plasma-array actuator with plasmas in the streamwise direction.

2.3.1. *DBD plasma actuators for separation control*

In the following some of the important studies utilizing the aforementioned common geometries of DBD plasma actuators and modes of operations are reviewed and summarized in table 2 to ease the overview.

Hultgren & Ashpis (2003) used a DBD plasma array – with electrodes oriented in the streamwise direction as depicted in figure 2.3*a)* – to control the separation occurring on a flat plate. Using a specially shaped top wall, the flow over the plate experiences a pressure gradient similar to the one on the suction side of a low-pressure turbine airfoil. The plasma actuation is tested for different Reynolds numbers and two freestream turbulence intensities. Results show a clear reduction of the separation bubble for the low intensity turbulence level, *i.e.* when the boundary layer separates while still laminar. The authors conclude that transition to turbulence of the shear layer flow above the separation bubble – induced by the plasma actuator – helps the boundary layer to reattach earlier than in the uncontrolled case.

Post & Corke (2004) investigated DBD plasma actuators to increase the lift to drag ratio of two stalled NACA66_3-018 airfoils with different cord lengths. The actuator placed at the leading edge gave the best control effect. Even though the lift increase saturated when increasing the actuation strength, the drag kept decreasing and a 400% increase in the lift to drag ratio was achieved. Their pressure measurements showed a higher pressure recovery using plasma actuators than the passive control via vortex generators. Later on, Huang *et al.* (2006) conducted a similar project to delay separation occurring on a turbine blade. For that study, they concluded that both DBD plasma actuators and passive vortex generators showed efficiency in delaying the separation, but the later produced drag when they are not in use, while DBD actuators are free of parasitic effects. The plasma actuator, upstream but closest to the separation position, showed a better effect than the more upstream actuator, hence the closer the actuator is placed upstream the separation point, the more effective it is.

Greenblatt *et al.* (2012) studied the control of a separated flow on a stalled flat-plate airfoil. The DBD plasma actuator is placed at the leading edge of the airfoil and used in a pulsed mode. The simulations were realized using a body force model calibrated against laser Doppler velocimetry data of the electric wind produced by the plasma actuator. Force balance measurements as well as simulations show an increase of the lift force on the airfoil when the pulse frequency of the actuator is equal to one of the sub-harmonic frequencies of the airfoils vortex shedding frequency. Using particle image velocimetry measurements, the authors explain the lift enhancement phenomenon as a result of the induced electric wind vortex severing the leading-edge vortical layer which merges then with the downstream trailing-edge vortex.

Jukes *et al.* (2012) showed reduction of the drag coefficient of a NACA0024 airfoil by using DBD plasma actuation with the plasma oriented in the spanwise direction. The addition of momentum close to the surface from the actuators reduced the size of the separated wake and the highest control effect was reached for an angle of attack of 12° with a reduction of 71% in the drag coefficient. In addition they were also able to delay the stall angle to 16°.

Jukes *et al.* (2013) compared the capability of streamwise oriented DBD plasma array actuators (producing co-rotating vortices as well as counter-rotating vortices) and double spanwise oriented DBD plasma actuators to increase the lift-to-drag ratio of a NACA4418 airfoil under two different Reynolds number conditions. They were able to substantially decrease the separation and even reattach the flow for angles of attack up to 18° for the low Reynolds number case. The efficiency of the counter-rotating DBD plasma actuator was slightly above the one producing co-rotating vortices. More importantly they show that for such cases, where the separation position is unknown or unstable, streamwise oriented DBD actuators are able of a better control as compared to spanwise oriented ones.

Jukes & Choi (2009*a*) studied the effect of a short pulse produced by a DBD plasma actuator on the surface of a cylinder – with plasma along the spanwise direction – on the unsteady separation and the vortex shedding street. Parametric studies of the position of the actuator, timing of the actuation compared to the vortex shedding period, strength and duration of the pulse allowed them to reach results with an increase of the lift on the cylinder of up to 300% (however, also inducing an increase of the drag by 25%). The PIV measurements give a better insight on the mechanism involved in mixing of the shear layer induced by the starting vortex resulting in the separation delay. In a parallel study using the same experimental setup, Jukes & Choi (2009*b*) tested the effect of the DBD plasma actuation on the separation and the vortex street using instead a pulsed mode. They showed the relation between the pulsed or modulation frequency of the actuation and the shedding frequency of the uncontrolled flow case. For non-dimensional pulsed frequencies (f_m) above 0.6 (uncontrolled Strouhal number equal to 0.22) the actuation delays the separation, suppresses the vortex shedding resulting in a reduction of the lift and drag fluctuations. On the other hand, for lower f_m the vortex shedding locked on a multiple of f_m increasing then the lift and drag fluctuations.

Benard & Moreau (2013) placed two DBD plasma actuators on a cylinder upstream (±50° from the upstream stagnation point) the separation point of the laminar boundary layer. They show that the actuation induces transition from laminar to turbulent of the boundary layer and thus delays the separation from the cylinder surface. Moreover, the use of the pulsed mode, called burst modulation in that paper, particularly influences the lock-on regime; irregularities in the vortex shedding street downstream the cylinder are decreased using

modulation frequencies equal to harmonics of the shedding frequency of the uncontrolled flow.

Author(s) (year)	Geometry	Flow parameters			DBD actuation parameters				
	type	U_0 [m/s]	$Re \cdot 10^3$	St	Dir.	V_d [kV]	f_d [kHz]	f_m [Hz]	Power [W]
Hultgren & Ashpis (2003)	turbine airfoil		50–300		Z	3.84	4	49–199	
Post & Corke (2004)	NACA66$_3$-018	10–30	77–460		Z	1.5–6	5		20
Huang *et al.* (2006)	turbine blade		50		Z	2.5	5		20
Greenblatt *et al.* (2012)	plate airfoil		3–20	0.182	Z	3–6	2–7	1–20	50–150
Jukes *et al.* (2013)	NACA4418	5.3–14.3	35–95		X, Z	2.4–3	6.4–7.1		
Jukes *et al.* (2012)	NACA0024	10	53		Z	4	9		
Jukes & Choi (2009*a*)	cylinder		15	0.22	Z	2.6–3.7	32.5	single pulse of 2.78–55.6 ns	
Jukes & Choi (2009*b*)	cylinder		15	0.22	Z	3.5	33	9–180	
Benard & Moreau (2013)	cylinder	15.6	40	0.2	Z	12–18	St num of 0.25–2.5	St num of 0.1–0.4	

TABLE 2. Previous studies on separation control by means of DBD plasma actuation, where U_0 and Dir. denote the freestream velocity and the direction of the electrodes of the plasma actuator, respectively.

CHAPTER 3

Design of DBD plasma actuators and study of the induced electric wind in quiescent air

The first step of the project was to develop a manufacturing technique of the DBD plasma actuators and verify their proper functioning. In this chapter we will describe the geometry of the DBD plasma actuators used during the project as well as the materials employed and the power supplies used to feed the actuators. Then follows an introduction to Laser Doppler Velocimetry (LDV) with its application to the electric wind study and description of the full setup. Finally the main results on the study of the electric wind in quiescent air are summarized as detailed in Paper 1 and some additional results are presented.

3.1. Design and construction of DBD plasma actuators

As the review in Chapter 2 highlighted, some geometric, material and electric parameters of plasma actuators are more important than others. A parametric study has thus been conducted in order to evaluate the electric wind induced by our in-house built plasma actuators but also in order to optimize them. Additionally, some data were also shared with the companion numerical project to develop a model of the body force produced by the plasma actuators.

3.1.1. *Geometry and material of the in-house built DBD plasma actuators*

Following is a description of the different geometrical parameters and materials tested and for an easier understanding the geometrical parameters are defined in figure 3.1. Table 3 summarises these for all actuators employed for tests during this project. Actuators A to E have been used for the study of the induced electric wind, while actuator F was developed for the flow control study. The listed remarks below concern actuators A to E, while a special paragraph is dedicated to actuator F:

- For the electric wind study, there was no limitation for the width of the embedded electrode (b) and thus a value of $b = 13$ mm was set as it was much wider than the plasma length, thus not limiting the plasma expansion. This can be seen in figure 3.2; the expansion length of the plasma is shorter than the width (b) of the embedded (bottom) electrode.

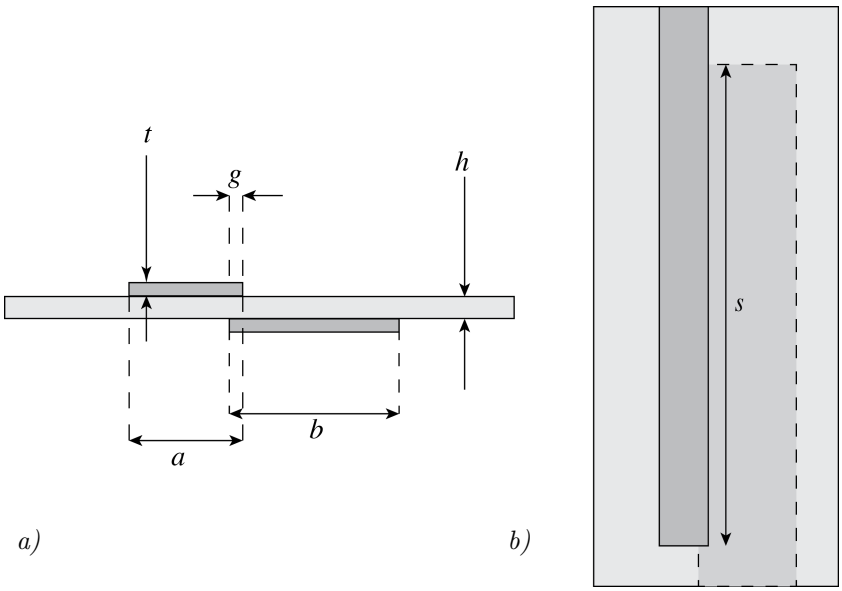

FIGURE 3.1. *a)* Side view and *b)* top view of a schematic of a single DBD plasma actuator and definition of the geometrical parameters.

Parameter	Value for actuators					
	A	B	C	D	E	F
Electrode material	Copper					Copper
Electrodes thickness (t) [μm]	66					66
Exposed electrode width (a) [mm]	6					3
Embedded electrode width (b) [mm]	13					8
Electrodes overlap (g) [mm]	0.5					0.5
Dielectric material	K+M	K+M	K	T	K+T	K+T
Dielectric thickness (h) [μm]	390	490	396	396	434	396
Actuation length (s) [mm]	140					260

TABLE 3. Geometrical parameters and materials of in-house built DBD plasma actuators used during the project. For the dielectric material, K stands for Kapton, M for Mylar and T for Teflon.

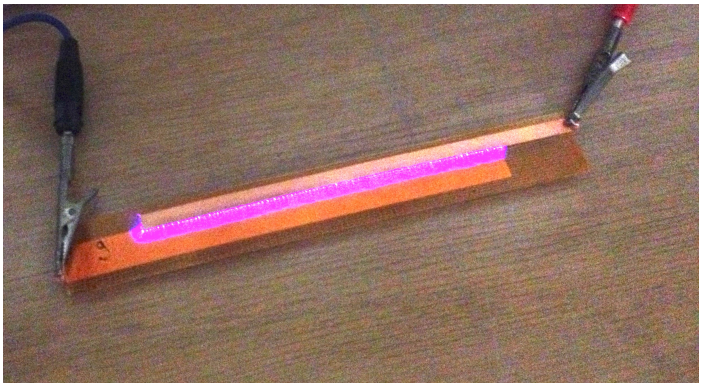

FIGURE 3.2. Photograph of the plasma produced by an in-house built single DBD plasma actuator built on the model of actuator A but with an actuation length s shorter than 140 mm.

- Following the advice of Post & Corke (2004), the electrodes overlapped in the spanwise direction with a small overlap of $g = 0.5$ mm to get a more uniform plasma in the spanwise direction.
- At first, a combination of polyethylene terephthalate (PET commonly called Mylar[5], M in table 3) and polyimide (Kapton, K) were used to build the dielectric sheet (for actuator A and B) as it was used with success by a group helping us to start with DBD plasma actuators[6]. Later on a study was conducted to compare electric winds produced with actuators dielectric sheets made of different materials (actuators C, D and E) using also there polytetrafluoroethylene (PTFE, Teflon, T). For a better understanding of the differences between the different dielectric materials, table 4 summarizes their relevant properties.
- The dielectric thickness effect on the electric wind was also studied when using actuators A and B. The dielectric sheet of both actuators was made of Mylar and Kapton. A 250 micron thick Mylar sheet was used for actuator A, while it was 350 micron thick for actuator B.

For the design of actuator F, the geometric constraints were more challenging as we aimed to have two actuators F mounted in tandem close to each other thereby forming a double DBD plasma actuator. In that configuration a third plasma can be generated between the exposed electrode of the most downstream actuator and the grounded electrode of the upstream actuator and this

[5]Mylar is actually a trademark registered by the company DuPont as for Kapton and Teflon
[6]Personal communication with Professors Andrea Cristofolini, Alessandro Talamelli and Gabriele Neretti as well as Alessandro Rossetti, Luca Ginepri and Matteo Motecchia from the University of Bologna, Italy.

Dielectric material	Common name	Dielectric strength [kV/mm]	Dielectric constant (ϵ_r)
Polyethylene terephthalate (PET)	Mylar (M)	17	3.0
Polyimide	Kapton (K)	200	3.9
Polytetrafluoroethylene (PTFE)	Teflon (T)	102	2.1

TABLE 4. Name and electrical properties of dielectric materials used for this study.

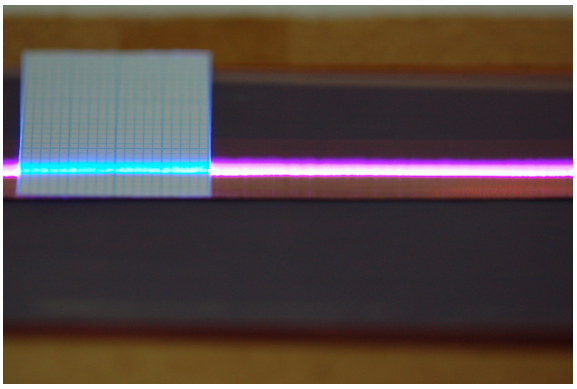

FIGURE 3.3. Photograph of the plasma produced by an in-house built single DBD plasma actuator built on the model of actuator F.

would produce an electric wind in the opposite direction than generated by the two other plasmas (Forte *et al.* 2007). Thus the first step was to reduce the width of actuator F. The width of the exposed electrode was reduced to $a = 3$ mm as that parameter is known not to influence the plasma formation and the width of the grounded electrode was also decreased to $b = 8$ mm. To ensure that the latter did not limit the plasma expansion, images were taken as shown in figure 3.3 and the plasma were measured not to exceed 5 mm using millimeter graduated paper. Furthermore a distance between the two actuators of 6 mm was also found to be sufficient in order to prohibit the have generation of the parasitic plasma (see figure 3.4).

3.1.2. *Power supply for the DBD plasma actuators*

During the first part of the project, the DBD plasma actuators were only used in steady mode meaning that a high-frequency high-voltage signal provided to the actuator was not coupled to a pulsed or modulation frequency.

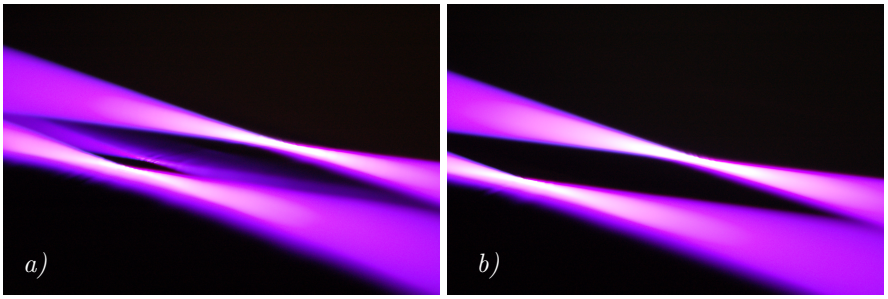

FIGURE 3.4. Photograph of plasma produce by the double DBD actuator with *a)* a parasitic third plasma generated and *b)* no parasitic third plasma generated.

To produce the high-frequency high-voltage alternating current needed to feed the DBD plasma actuators, a combination of a low-amplitude signal generator and a high-voltage amplifier was used first (see figure 3.5). The low-amplitude signal generator output was a high frequency sine wave of the desired driving frequency (f_d). Then the amplifier increased the voltage amplitude with a gain of 2000. The present amplifier was able to deliver voltages up to 20 kV_{p-p}. However, the driving frequency was limited by its slew rate to values lower than or equal to 2 kHz when used to output driving voltages (V_d) of several kilovolts. Finally, the amplified high-voltage output was connected to the exposed electrode of the plasma actuator whereas the covered electrode was grounded. This electrical arrangement was used for the study of the electric wind with actuators A and B where driving voltages (V_d) between 4 and 18 $kV_{p-p}$with driving frequencies from 0.5 to 2 kHz were tested.

Although the couple signal generator with amplifier offers advantages such as the freedom to chose the signal waveform, it was nonetheless preferred to acquire a high-voltage generator of type *Minipuls2* (*GBS Elektronik*), since the previous amplifier was borrowed from KTH School of Electrical Engineering. This choice was justified by the competitive price of the device but also mainly by its small size and weight as can be seen in figure 3.6. The *Minipuls2* was used here with a laboratory low-voltage generator but it can also be used with a battery for on-road tests. This solution provided a high-frequency sine-like wave with an amplitude of several kilovolts to the exposed electrode (the embedded electrode was grounded). Moreover, the laboratory low-voltage generator indicates the voltage and current provided to the *Minipuls2* hence giving an indication of the power consumption of the circuit containing the *Minipuls2*, the electrical cables and the DBD plasma actuator. Additionally, a high-voltage probe (*Pintek Electronics HVP-39PRO*) connected to an oscilloscope (*Tektronix TDS 2014C*) was used to monitor the sine-wave amplitude and frequency between

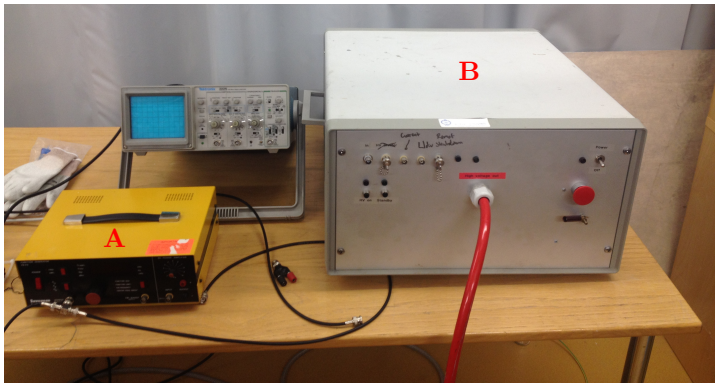

FIGURE 3.5. Photograph of the first power supply arrangement used for the DBD plasma actuators. **A** is the low-amplitude signal generator and **B** is the voltage amplifier.

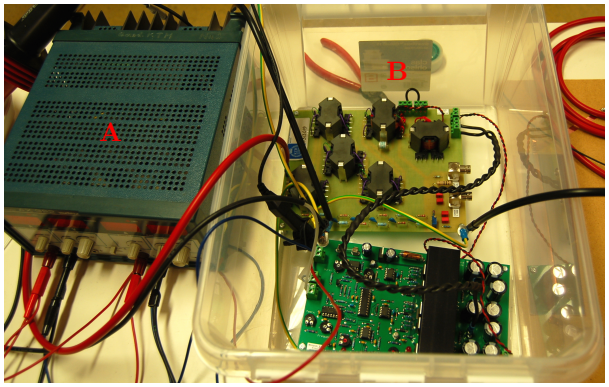

FIGURE 3.6. Photograph of the second power supply arrangement used for the DBD plasma actuators. **A** is the low-voltage generator and **B** is the high-voltage generator type *Minipuls2*.

the high-voltage generator and the exposed electrode. This electrical arrangement does not output driving frequencies as low as the previous arrangement and thus tests realized with the *Minipuls2* were conducted with voltages between 6 and 10 kV_{p-p} at a driving frequency of 6 kHz as it was observed that the temperature of the dielectric increased while using higher frequencies than 6 kHz indicating that the heat losses in the dielectric became substantial.

3.2. Electric wind measurement setup

3.2.1. *Laser Doppler Velocimetry measurement technique*

Laser Doppler Velocimetry (LDV) was employed to record the electric wind velocity using a single-component Dantec Dynamic LDV FlowLite system with a Burst Spectrum Analyzer (BSA 60) processor. LDV is an advantageous technique as it is non-intrusive, can measure instantaneous velocities with high frequency response of the flow and it can sense to the direction of the flow. LDV actually does not measure the velocity of the flow but the velocity of tracers contained in the flow, thus the choice of tracers is important, they must accurately follow the flow to acquire accurate measurements.

In the case of a single-component LDV, a laser beam is split in two by the succession of a beam splitter and a Bragg cell resulting in two high-frequency oscillating laser beams with a wavelength (λ) and a fixed frequency shift (f_{sh}) between them. The output of the Bragg cell of the FlowLite system were two 632.8 nm wavelength laser beams with a nominal beam diameter of 1.68 mm and a frequency shift of 40 MHz. The laser beams transmitted to the LDV laser head, pass through an optical lens which focuses the two beams. The ellipsoidal measurement volume is thus created by the intersection of the incident laser beams. For this study the nominal focal length of the optics was 160 mm, the beam spacing at the exit of the lens was 38 mm and the resulting measurement volume can be estimated to have a diameter of 0.08 mm and a length of 0.64 mm.

In the measurement volume, the intersection of the two laser beams produces a fringe pattern (light planes) moving at a constant velocity (U_{sh}) due to the frequency shift between the beams. The distance between two fringes (Δ_x) is a function of the incident laser wavelength and the intersection angle between the two beams (Θ). Based on the Doppler effect, a tracer crossing the measurement volume will scatter light with another frequency, f_D, that is linearly linked to the velocity of the tracer. A photodetector, also placed in the laser head, transmits the waveform of the light scattered by the tracer to the signal processor which extracts f_D and evaluates the velocity of the tracer (u_t) as:

$$u_t = \frac{\lambda}{2\sin(\Theta/2)} f_D. \tag{3.1}$$

The sensitivity of LDV to the direction of the flow is possible because of the interaction of the two incident beams creating moving fringes. Indeed, if the fringes were not moving, tracers moving with a velocity lower than zero, meaning moving in the reverse direction, would scatter light with f_D smaller than zero but the processor would not be able to distinguish negative from positive frequencies so the LDV would not be sensitive to the flow direction. In the case of moving fringes, tracers moving in the opposite direction to the fringes

are considered to have a positive velocity and scatter light with f_D higher than f_{sh} while particles moving with a negative velocity scatter light with a positive f_D but smaller than f_{sh} (Dynamics 2011).

Diethylhexylsebacate (DEHS) droplets with a nominal diameter of about 1 μm and density of 912 kg/m^3, produced by an atomizer were used as flow tracers also called seeding particles. As mentioned in chapter 2, the electric wind can experience fluctuations with a frequency up to the driving frequency of the DBD plasma actuators, hence to ensure accurate measurements of the flow, the seeding particles need to be able to follow such high-frequency changes. The highest frequency change resolvable by a certain particle is a function of its size (diameter d_p) and its density (ρ_p) defining the relaxation time of a particle (τ_0) in a certain fluid by:

$$\tau_0 = \frac{\rho_p d_p^2}{18\mu}, \tag{3.2}$$

with μ being the dynamic viscosity of the fluid. Then the cut-off frequency f_c up to which the particle can follow flow oscillations with a slip (s) smaller than 1% (equivalent to a particle response of 99%) is defined as (Albrecht *et al.* 2003):

$$f_c = \frac{1}{2\pi\tau_0}\sqrt{\frac{1}{(1-s)^2} - 1}. \tag{3.3}$$

The relaxation time of DEHS droplets was found to be around 2.7 μs allowing the particles to follow flow oscillations at frequencies higher than 8 kHz with a particle response of 99%. The calculations were conducted with room temperature and higher temperature (up to 41°C) to consider the effect of the increased temperature in the plasma region (see chapter 2) and showed that this temperature change did not have any significant influence on the relaxation time and cut-off frequency.

Finally, when averaging LDV data, weighted-average methods need to be employed to obtain accurate results because the sampling is not based on a constant frequency sampling method but on the recording of the velocity of single tracers. Considering a high flow velocity during a certain period T, more particles will pass through the measurement volume and will transmit instantaneous velocity data to the processor than for lower flow velocities. Additionally, those particles will be present in the measurement volume during a shorter time (shorter transit time). Thus, using a classical ensemble average of the particles velocities to determine the mean velocity (and other statistical values) will lead to an overestimation of the mean velocity, hence the use of a weighted-average method is then necessary. For this project the transit-time weighting method was used to evaluated statistics of the flow with the weighting coefficient of the

particle i being defined as:

$$\eta_i = \frac{t_i}{\sum_{j=1}^{N} t_j}, \tag{3.4}$$

with t_i being the transit time of the particle in the measurement volume and N being the total number of particles crossing the measurement volume during the period over which the statistics are evaluated. Thus a faster particle will have a smaller weighting coefficient than a slower particle and the mean (U) and rms (u') of the velocity are calculated though:

$$U = \sum_{i=1}^{N} \eta_i u_i, \tag{3.5}$$

$$u' = \sqrt{\sum_{i=1}^{N} \eta_i (u_i - U)^2}, \tag{3.6}$$

u_i being the instantaneous velocity of the particle i.

3.2.2. *Measurement setup*

This part describes the two setups used for the measurements of the electric wind produced by the in-house built DBD plasma actuators.

For the first set of experiments on the electric wind, a half cylinder made of Plexiglas with a radius of 50 mm was used since this geometry was relevant for the forthcoming separation control experiments (see chapter 4). The single DBD plasma actuator was mounted on top of the model and the edge of the exposed electrode producing the plasma coincided with the highest position of the half-cylinder as shown in figure. 3.7. The covered electrode was thus embedded between the dielectric and the cylinder surface. The cylinder was placed inside a large Plexiglas box in order to reduce disturbances from the surroundings on the electric wind.

The LDV laser head was mounted to a vertical axis of an ISEL C142-4 traversing system that could be controlled with the measurement software recording the velocity. In order to measure several profiles at different downstream locations, the box containing the model and the actuator was translated horizontally (in the x-direction) using a manual traversing table with a precision of 0.05 mm. The side of the box separating the laser head from the plasma actuator was built in glass in order to minimize optical distortions. The DEHS droplets were continuously fed into the box, which was emptied and cleaned from particles after each profile measurement.

This setup was used to record electric wind profiles using DBD actuators A and B and the first power supply arrangement (with the amplifier) and thus study the downstream development of the electric wind, investigate the effect of

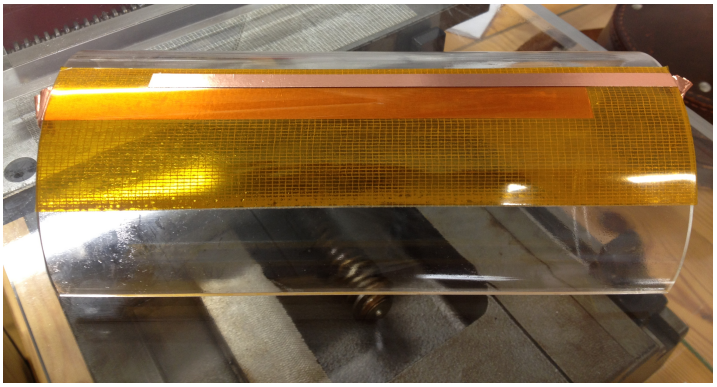

FIGURE 3.7. Photograph of the single DBD plasma actuator placed at the top of the plexiglas half-cylinder.

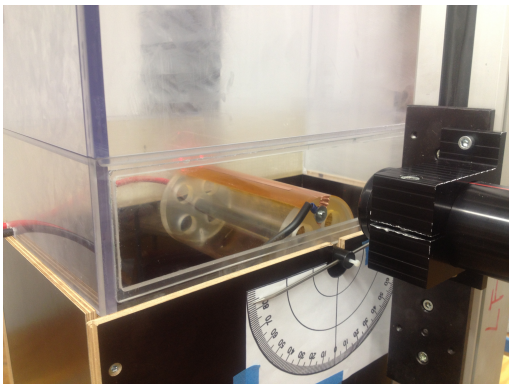

FIGURE 3.8. Photograph of the second setup. The single DBD plasma actuator is mounted on a full cylinder which could be rotated around its centre and placed inside the Plexiglas box.

changes of the driving frequency, driving voltage and thickness of the dielectric sheet on the mean velocities and observe variations of induced velocities during one period of the driving current looking at the phase-averaged velocities.

Unfortunately, recording velocities very close to the surface of the model was only possible for streamwise locations close to the apex of the half-cylinder, when moving downstream one of the two incident LDV laser beam was interrupted by the model making the measurement impossible at low vertical positions. To be able to access measurement points closer to the surface of the cylinder for downstream positions, a second setup was thus developed. Instead of a half-cylinder, the single DBD plasma actuator was mounted on a full cylinder with a diameter of 100 mm (see figure 3.8). The cylinder could be rotated

around its centre in order to change the angular position of the actuator. Then, by recording the wall-normal velocity profile, *i.e.* azimuthal component, at the apex of the cylinder using the vertical traversing system for different angular positions of the actuator, the downstream development of the electric wind could be mapped.

This second setup was used to study the electric wind produced by the DBD plasma actuators C, D and E using the second power supply arrangement with the *Minipuls2* and thus map the development of the electric wind for different dielectric materials.

3.2.3. *Data analysis*

At each measurement point 50000 samples were recorded with an average sampling rate of around 2000 samples/sec. The transit-time weighting method described above was employed to evaluate statistical quantities. Due to the high frequency of the driving voltage and the limitations of the sampling rate of the LDV system, only few samples could be collected for each cycle or period of the driving current so for the phase-averaging, a phase reconstruction method similar to the one used by Kotsonis & Ghaemi (2011) was employed.

When studying the data it was found a few of the data points could be considered as outliers. For the phase, *i.e.* ensemble, averages, the period was divided into 200 bins. For each of the bins, the Chauvenet's criterion was applied (Coleman & Steele 2009) to remove eventual outliers; less than 1% of the samples was discarded by the criterion.

3.3. Results

3.3.1. *Summary of results detailed in Paper 1*

- A driving voltage of 4 kV_{p-p} did not induce any electric wind and no plasma could be observed visually on the surface of the dielectric material leading to the conclusion that the voltage was inferior to the breakdown threshold voltage of air at atmospheric conditions.
- The in-house built plasma actuators are able to produce electric winds that are similar to wall jets with velocities of several meters per second. The wall jet initiates at the edge of the exposed electrode to the side of the embedded electrode and develops downstream. The electric wind development was studied on the surface of a cylinder and results show that it stays attached to the cylinder surface. This is probably due to the actuator adapting to the shape of the geometrical model and is clearly an advantage for the separation control with DBD plasma actuation.
- The parametric study showed that the driving voltage and the driving frequency increases the velocity of the wall-jet-like electric wind. Although thinner dielectrics are producing higher velocities for the range

of driving voltages we are interested in accordance with the work of Forte *et al.* (2007).

- The electric wind induced by the DBD plasma actuator is directed away from the exposed electrode during both strokes of the AC period.
- The bi-modal behavior of the probability density function (pdf) of velocities of the electric wind was observed and was due to the fact that one stroke of the AC period induced higher velocities than the other (twice as much). Moreover an increase of the velocity (thus a positive acceleration) was observed during both strokes showing that in the present configuration, the DBD plasma actuator behaved according to the PUSH-push mechanism.
- The bi-modal character transitions to a uni-modal for measurement positions far from the exposed electrode, even though the electric wind was still observable, confirming that the force produced by the actuator can be assumed to be steady. The pulsations of the electric wind are visible along a longer distance downstream the exposed electrode for high driving voltages and low frequencies.

3.3.2. *Additional results*

Comparison of different dielectric materials. Using the second setup, comparisons of the electric wind produced by actuators with dielectrics made of different materials were made. Figure 3.9 shows the evolution of the azimuthal component of the mean velocity of the electric wind produced by actuators C, D and E in the streamwise direction. Comparing the electric wind produced by the DBD plasma actuators C and D, it can be concluded that actuator D with a dielectric made of Teflon (with a dielectric constant of $\epsilon_r = 2.1$) induces higher velocities than actuator C for which the dielectric is made of Kapton ($\epsilon_r = 3.9$, see also table 4). However it was observed that actuator D was damaged more frequently than actuator C by an electric arc passing throughout the dielectric material. This is probably due to the fact that the dielectric strength of Teflon is lower than the one of Kapton and it was decided to build an actuator made of both Kapton and Teflon (actuator E). As can be seen in figure 3.9*c)*, this actuator produces an electric wind with an amplitude similar to actuator D.

Degradation of the actuators. One unfortunate feature of DBD plasma actuators that could be observed during this project is that the dielectric material degrades and after some utilization time, an electric arc can go through the dielectric and the actuator needs then to be rebuilt. Figure 3.10*a)* shows patterns that are appearing on the dielectric while using the actuator, those patterns become more and more visible with time and ultimatively the actuator "burns" after few hours of use (a "burned" actuator can be seen in figure 3.10*b)*).

A lifetime study of the double DBD plasma actuator used for the separation control study (see chapter 4) made of two single DBD actuators type F placed

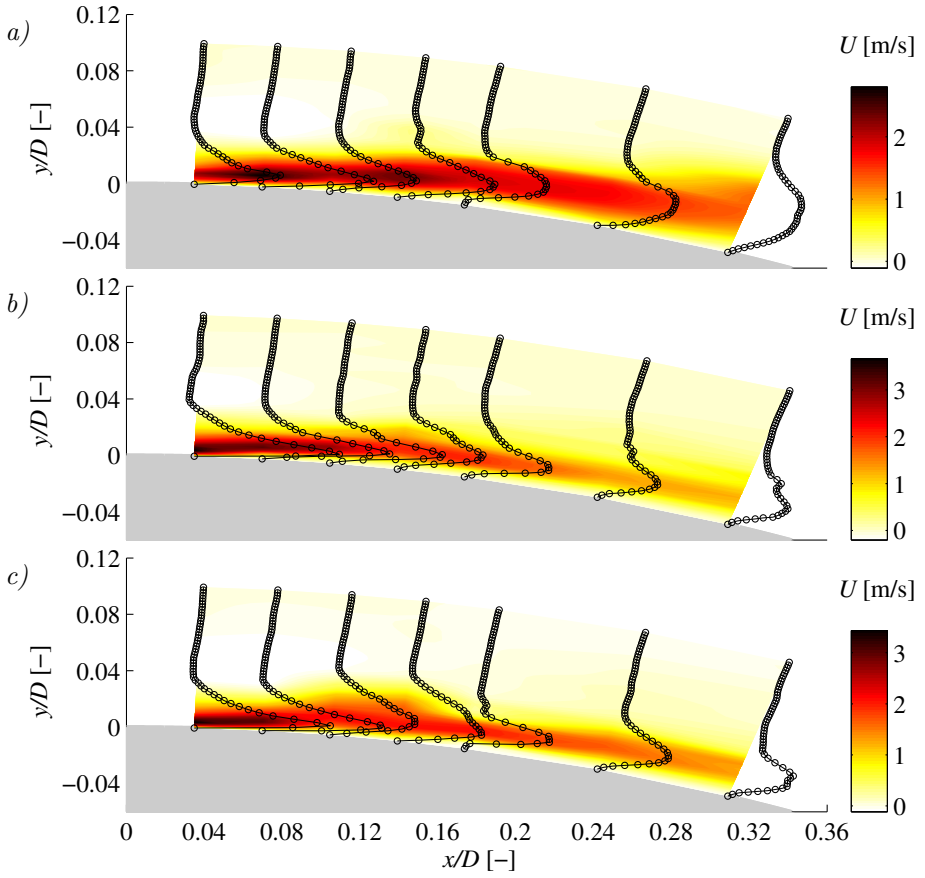

FIGURE 3.9. Contour plot of the mean electric wind – azimuthal component – induced by the DBD plasma actuator *a)* C, *b)* D and *c)* E in quiescent air using a driving voltage of 8 kV_{p-p} and a driving frequency of 6 kHz. The grey area represents the cylinder. The edge of the actuator producing the plasma is at $x = 0$ mm, $y = 0$ mm.

in tandem was conducted. The actuator was mounted on top of a half-cylinder protruding from a flat plate in the test section of an open-circuit wind tunnel running with an inlet freestream velocity of 5 m/s. A glass Pitot tube was used to record the total pressure 600 mm downstream the actuator. For more details on the setup, the reader is referred to chapter 4. In parallel, the voltage and current provided by the laboratory low-voltage generator to the *Minipuls2* was monitored in order to evaluate the power consumption of the actuator

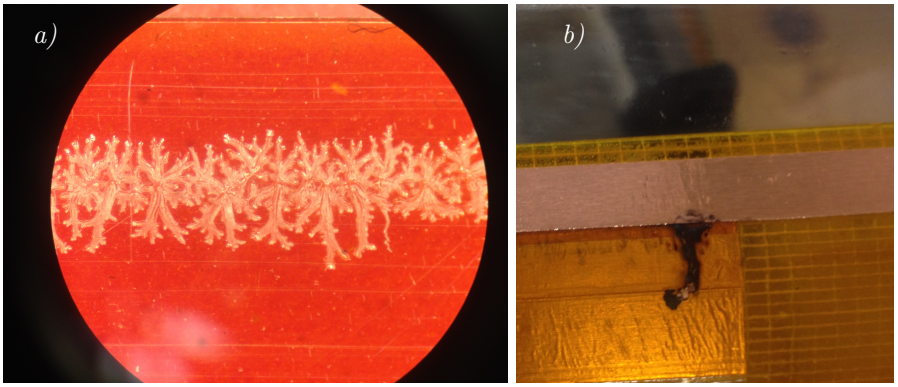

FIGURE 3.10. *a)* Photograph of the patterns appearing in the dielectric material at the edge of the exposed electrode after some time using a DBD plasma actuator. *b)* Photograph of the a damaged actuator after an electric arc went through the dielectric sheet.

and was at time zero $Power_0 = 38$ W including the power consumption of the *Minipuls2*, the power consumption of the actuator (two times 260 mm of actuation) and the power dissipated in the electric cables.

Figure 3.11 shows the evolution of the total pressure and the power consumption during the lifetime of the actuator which "burned" after more than two hours. It can be observed that the pressure varies within 20% during the lifetime of the actuator and the variations are followed by variations of the power consumption, which varies within 30%. While the electrical power consumption increases at high rate, the total pressure seems to be almost constant from the time 3000 sec to 6550 sec. This could suggest that adjusting the power could help to keep the force induced by the plasma actuators constant. Hanson *et al.* (2014) started to investigate this phenomenon and highlighted strong dependence between the evolution of the capacitances (effective and cold) and the power consumption of the actuators together with the degradation of the dielectric material and suggested than monitoring only the driving voltage and driving frequency input to the actuator was not sufficient to provide a constant output from the actuators.

Further investigations are needed to make the actuators more robust and to monitor the electrical power consumption of the actuators to keep a constant output.

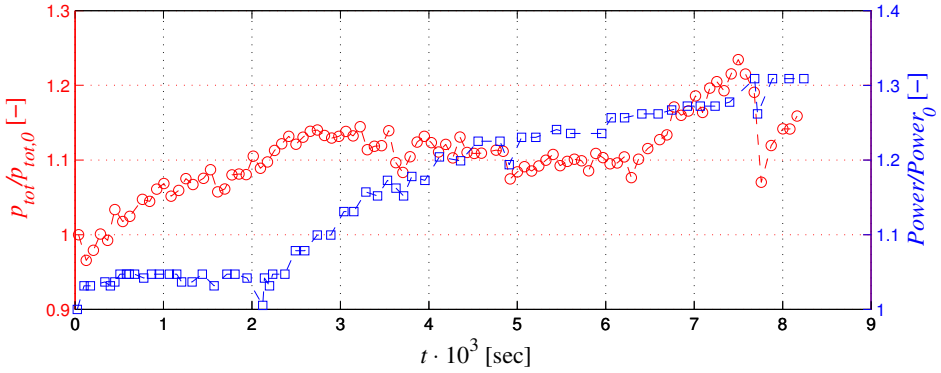

FIGURE 3.11. Monitored total pressure and electric power consumption during the lifetime of a double DBD plasma actuator.

CHAPTER 4

Flow separation control and drag reduction study

This chapter describes the experimental setup and measurement techniques used to investigate the baseline case as well as the separation control study using the DBD plasma actuators and the resulting drag reduction.

4.1. Flow separation control setup

The experiments were conducted in an open-circuit wind tunnel (NT2011, KTH Fluid Physics Laboratory) with a 1.5 m long test section and a cross-sectional area of 0.5 m $\times$ 0.4 m (height $\times$ width).

The chosen flow case is a turbulent boundary layer developing upstream a two-dimensional (2D) cylindrical bump with a diameter $D = 0.10$ m. The boundary layer separates while passing over the bluff body and reattaches on the flat plate further downstream. A photograph of the test section, including the flat plate with the cylindrical bump, can be seen in figure 4.1. The 20 mm thick Plexiglas flat plate is 1.5 m long, 0.4 m wide and was mounted 0.2 m above the bottom wall of the test section allowing access for the pressure tubings and electric cables from below. A schematic of the setup is shown in figure 4.2 defining the coordinate system employed for the study. The origin of the system is defined at the top of the plate for the wall normal direction (y-axis) and at the "leading edge" of the half-cylinder for the streamwise direction (x-axis). Cross-sectional measurement planes are also visible in the schematic: measurements in planes A_1 and A_2 were conducted to evaluate the drag as described in section 4.2 and measurements in plane A_3 helped characterizing the velocity profile approaching the bump.

The experiments were realized at two Reynolds numbers, Re_D (based on the diameter of the bump D). The development of the baseline flow case was investigated for $Re_D = 50000$ and 100000 setting the freestream velocity U_0 equal to 8 and 16 m/s, respectively, while the flow control study with plasma actuation was realized at $Re_D = 33000$, corresponding to $U_0 = 5$ m/s.

To ensure the development of a turbulent boundary layer upstream the bump, tripping tape was fixed on the elliptic leading edge of the flat plate to trigger transition at a fixed streamwise location. The tape was *DYMO* tape with the letter "V" (apex oriented in the flow direction) and was fixed parallel to the leading edge. In the case of the lowest Reynolds number ($Re_D = 33000$),

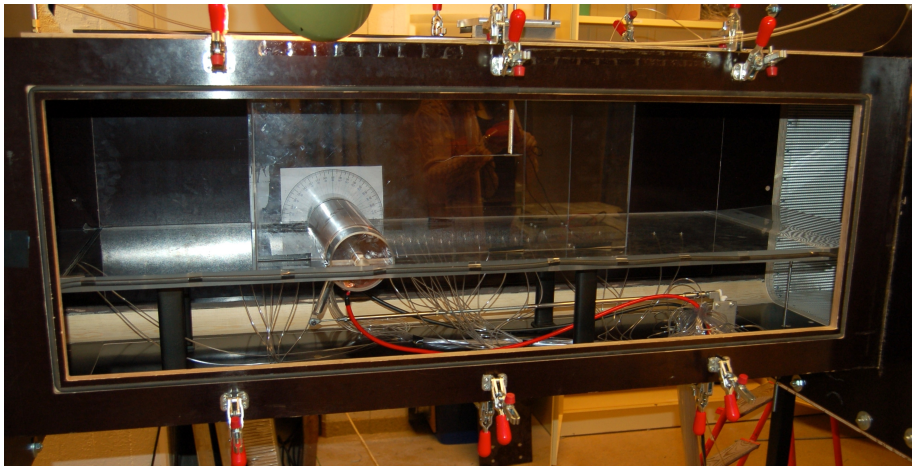

FIGURE 4.1. Photograph of the test section including the setup used for the separation control study. The flow is from left to right.

the tripping tape turned out to be insufficient, hence a wire with a diameter of 0.26 mm was fixed just upstream the tripping tape, approximately 0.5 mm above the flat plate, the tripping tape breaking down an eventual vortex shedding induced by the wire.

Although the bluff body was chosen to be a half cylinder, it was constructed from a full cylinder that enabled a change in the position of the double DBD plasma actuator (to be described in section 4.1.3) by rotating the cylinder around its centre in a similar manner as for the electric wind measurements (see chapter 3). The centre of the cylinder is thus located 0.55 m downstream the leading edge of the plate in a way that its axis is at the same level than the top surface of the flat plate to obtain a half-cylindrical bump protruding out from the plate. Rectangular end-plates (separated by 0.26 m in the spanwise direction) made of Plexiglas were mounted on each side of the active part of the double actuator, as visible in figure 4.1, in order to improve the two-dimensionality of the flow. To avoid abrupt changes along the spanwise direction, dummy half-cylinders with a radius of 50 mm were placed between the end-plates and the test-section walls.

4.1.1. *Hot-wire anemometry*

Constant-temperature hot-wire anemometry was used to perform streamwise velocity measurements of the baseline, *i.e.* uncontrolled, flow case. Vertical profiles of the streamwise velocity component were recorded at different streamwise locations to study the evolution of the flow upstream, on top and downstream the half-cylinder bump. Special focus was given to the profile recorded at the

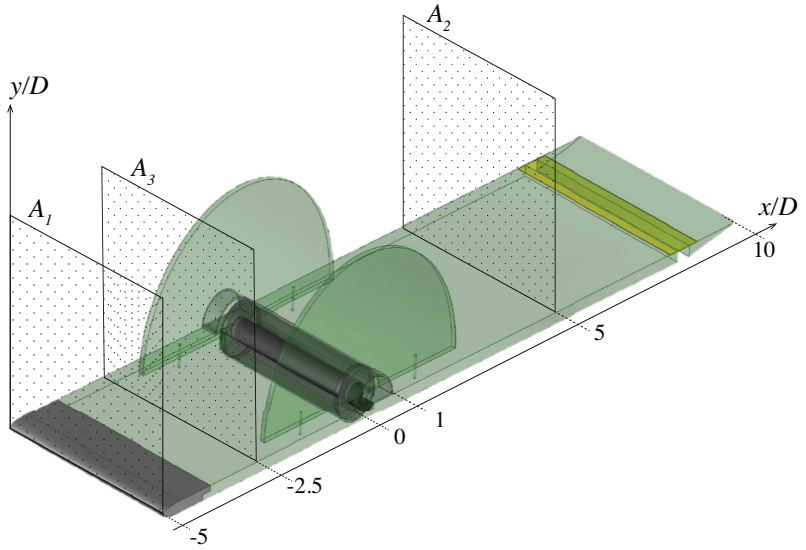

FIGURE 4.2. Schematic of the setup used for the separation control experiment. The dotted wall-normal planes A_1, A_2 and A_3 are virtual cross-sectional planes.

position $x/D = -2.5$ (cross-sectional area A_3 in figure 4.2) in order to document the turbulent boundary layer approaching the cylindrical bump.

The hot-wire anemometry technique is a single-point, intrusive measurement technique based on convective heat transfer between the flow and a heated wire. It allows instantaneous velocity measurements with a high frequency response. A small wire (here made of tungsten or platinum) with a certain temperature-sensitive resistance $R(T)$ is mounted on so-called prongs (welded or soldered) and placed in the flow and normal to the flow direction at the position the velocity needs to be measured. The wire, through the prongs and a cable, is connected to the anemometer containing a wheatstone bridge and a servo amplifier which forms an electrical circuit. In this configuration, with one small wire – which accounts for most of the resistance – mounted between the prongs, only the component of the velocity perpendicular to the axis of the wire can be measured. Geometrical and material characteristics of the in-house built hot-wire used for this study are summarized in table 5.

For this study the anemometer with the constant temperature (CT) mode was used. Another method to conduct hot-wire measurements is to use an anemometer in constant current (CC) mode. In the first mode of operation, as the name indicates, the temperature of the wire is kept constant by the anemometer while in the second it is the current passing along the wire that is kept constant. The CT mode offers a better frequency response than the

Parameter	Value for hot-wire	
	HW_1	HW_2
Material	Tungsten	Platinum
Wire length ℓ [μm]	750	300
Wire diameter Ø [μm]	2.5	1.3
Attached method	welded	soldered
Over-heat ratio OH [%]	80	
Low-pass (LP) filter [kHz]	10	30
Sampling frequency (f_s) [kHz]	20	60
Sampling time (T_s) [sec]	20 to 40	

TABLE 5. Geometrical parameters and material of in-house built hot-wires as well as operating parameters of the constant temperature anemometry used during the project.

CC mode and is thus generally chosen for velocity measurements of turbulent flows as they contain high-frequency fluctuations that need to be resolved for accurate measurements (Bruun 1995).

When used in the CT mode, the wire is heated at a constant relative temperature (T_w) compared to the reference flow temperature (T_0) defined by the overheat ratio (OH):

$$OH = \frac{R(T_w) - R(T_0)}{R(T_0)}. \tag{4.1}$$

Here, the hot-wire anemometer system used is a *Dantec SteamLine* 90N10 frame in conjunction with a 90C10 constant temperature anemometer module operated at a resistance overheat of 80%.

The flow around the wire is cooling it down and thus changes its temperature which is linearly related to its resistance. The anemometer adapts the voltage amplitude in the circuit in order to compensate and keep the wire temperature constant. The changes in voltage provided by the anemometer are then directly linked to the changes of the instantaneous velocity (u) of the flow. One limitation of single hot-wire measurements in that the wire is not sensitive to the direction of the flow, *i.e.* it allows measurements of the velocity component perpendicular to its axis but cannot determine the direction of the flow as any direction normal to it would result in the same heat transfer from the wire and thus yields the same resistance change.

The relation between the instantaneous velocity and the voltage can be expressed *e.g.* though a modified version of the classical King's law (Johansson

& Alfredsson 1982) defined as follow:

$$U = k_1 \left(E^2 - E_0^2\right)^{1/n} + k_2 \left(E - E_0\right)^{1/2}, \tag{4.2}$$

where E is the output voltage of the anemometer for the calibration velocity U, E_0 is the voltage in case of zero velocity and k_1, k_2 and n are the calibration constants determined together with E_0 during the calibration step prior to the measurements.

The calibration must be realized over the range of velocities that will be measured later on. This is usually realized for wind tunnel experiments *in situ* in the freestream against a Pitot-static pressure probe. Prior to turning on the wind-tunnel, E_0 is measured, then varying the speed of the wind tunnel, the flow velocity measured by the pressure probe and the voltage from the anemometer are plotted against each other to determine the calibration constants. This method was used for the calibration of the hot-wire measurements in this study with the Pitot-static tube connected to a micromanometer of type *Furness Controls Limited FC012* (full scale 2 kPa), which was also used to monitor the freestream velocity during the experiments.

The calibration as well as the measurements should in theory be realized at the same temperature T_0 to get accurate results, however, this is usually hard to achieve while doing measurements for instance in wind tunnels that do not have a heat exchanger for temperature control. In that case monitoring the temperature during calibration (T_0) and measurements (T_a) and using a temperature compensation method is a solution to correct the results using the following relation:

$$E_c^2 = \left(1 - \frac{T_a - T_0}{OH/\alpha_0}\right)^{-1} E^2, \tag{4.3}$$

where E_c is the corrected voltage and α_0 is the temperature coefficient of resistivity of the wire (Jørgensen 2002).

In order to avoid aliasing of the signal, the sampling frequency of the measurements should be at least twice the highest frequency in the signal to fulfill the Nyquist sampling criterion. For hot-wire measurements a low-pass (LP) filter can be set through the anemometer at the highest frequency that needs to be resolved. For the present studies a LP filter was set at 10 kHz while measuring the flow with the inlet Reynolds number of 33000 and 30 kHz for higher Reynolds number cases. Then a sampling frequency of 20 kHz and 60 kHz was used, respectively, for the two LP settings.

Another important parameter for hot-wire measurements of turbulent flows is the spatial resolution which should be commensurate with the smallest eddies present in the flow. This parameter is directly linked to the length of the wire, hence a shorter wire will resolve smaller scales than a longer wire. A spatial correction method suggested by Smits *et al.* (2011) was also employed to assess the underestimation in the measured turbulence intensity. This method

consists in correcting the rms of the velocity (u') with the following equation:

$$u_c'^{+} = \sqrt{M \cdot f(y^+) + 1}\; u_m'^{+}, \tag{4.4}$$

where $u_m'^{+}$ is the measured rms in wall units indicated by the superscript +, *i.e.* using the friction velocity u_τ determined from a Clauser chart method (Clauser 1956) for the Re_D equal to 50000 and 100000 cases and from a fit to a law of the wall description (Örlü *et al.* 2010) for Re_D =33000. $u_c'^{+}$ is the corrected rms and M and $f(y^+)$ are two functions of the correction method defined as:

$$M = 0.0091\; \ell^+ - 0.069, \tag{4.5}$$

$$f(y^+) = \frac{15 + \ln(2)}{y^+ + \ln(\exp^{(15-y^+)} + 1)}, \tag{4.6}$$

where ℓ^+ is the wire length in wall units.

Although one should reduce the length of the wire as much as possible in order to reduce the effect of spatial resolution, it is required to keep the length-to-diameter ratio of the wire above 200 in order to reduce the effect of heat conduction to the prongs (Ligrani & Bradshaw 1987).

Finally, to allow traversing in the vertical direction, the hot-wire probe was mounted at the bottom of a sting attached to a traversing system that was fixed on the roof of the test section. Traversing was performed using a lead screw traverse driven by a stepper motor yielding a minimum step size of around 2 micron. The wall position was determined using the "mirror image technique" (Örlü *et al.* 2010). A photograph was taken of the probe at a position close to the wall with two gauge heights (of 0.5 mm and 1 mm) next to it with a high definition camera as can be seen in figure 4.3. Through image

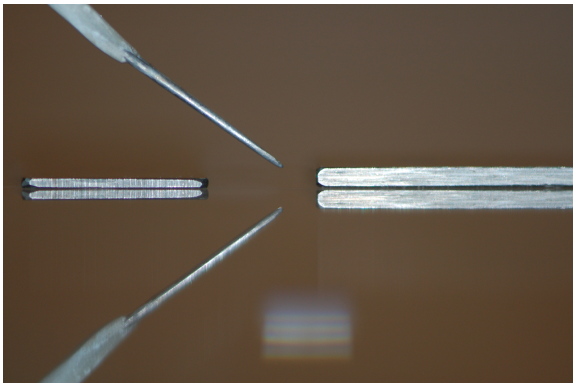

FIGURE 4.3. Photograph of the prong of the in-house built hot-wire with the gauge heights used for the "mirror image technique" to determine the wall position.

processing, the real dimension of one pixel could then been determined with the gauge heights and the height from the wall to the probe was then assessed.

4.1.2. *Pressure measurements*

Both for the uncontrolled and controlled cases, the streamwise evolution of the static pressure at the wall was read using 46 pressure taps:

- 7 on the flat plate upstream the cylinder,
- 25 downstream the cylinder and
- 14 pressure taps on the cylinder.

The number of pressure taps on the cylinder was limited by the presence of the double actuator but their position could be varied by rotating the cylinder and only 8 taps at a time were exposed to the flow. The pressure taps were connected through vinyl tubings to a 48 channels mechanical *Scanivalve*. The pressure from the *Scanivalve* was in turn fed to a high accuracy *MKS 120S Baratron* pressure transducer (full scale 10 Torr) against the atmospheric pressure with a sampling time of 8 to 14 sec depending on streamwise position after a settling time of 5 sec.

The measured static wall pressure data were used to evaluate the evolution of the pressure coefficient C_p at the wall, defined as

$$C_p = \frac{p_i - p_1}{\frac{1}{2}\rho U_0^2}\,, \tag{4.7}$$

where p_i denotes the static pressure at the pressure tap number i, hence p_1 is the pressure at the most upstream pressure tap ($x/D = -3.2$), ρ is the air density and U_0 is the freestream velocity monitored by the Pitot-static probe at the inlet of the test section.

Pressure measurements were also made in the wake of the cylinder for both the uncontrolled and the controlled cases to acquire data for the drag evaluation (see section 4.2). A glass Pitot probe was manufactured in order to conduct measurements close to the DBD plasma actuator without igniting sparks between the actuator and the probe. This probe was built using a glass capillary tube with an inner diameter of 0.56 mm and outer diameter of 0.80 mm.

Scanning of the total pressure close to the wall at different streamwise positions downstream the cylinder in the uncontrolled case was used to check that the flow was reattached at the position $x/D = 5$: there was no back flow and the velocity profile could thus be measured my means of pressure measurements. However, the boundary layer did not entirely recover, *i.e.* the boundary-layer approximation stating that the static pressure can be considered constant along the wall-normal direction is not applicable here. Figure 4.4 shows a comparison between the aforementioned velocity profiles.

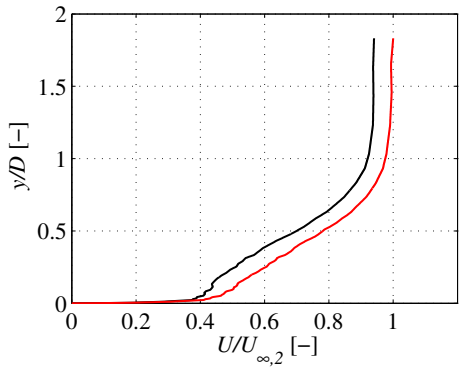

FIGURE 4.4. Streamwise component of the wall-normal velocity profile at $x/D = 5$ using the differential pressure based on total pressure measurements and assuming that the static pressure in the wake is equal to the value at the wall (black curve, 1), and employing the measured static pressure profile (red curve, 2).

It can be seen that the variations of the static pressures cannot yet be neglected here as the static pressure is higher at the wall than in the freestream, thus considering a constant static pressure from wall leads to an underestimation of the velocities. Since no risk of spark had been ensured at that streamwise position, a metallic Pitot-static probe could be used to record the static pressure profile.

The same traversing system as for the hot-wire measurements was used to traverse the pressure probes in the wall-normal direction. The pressure from both tubes was also read by the high accuracy *MKS 120S Baratron* pressure transducer against the atmospheric pressure with a sampling time of 32 sec.

4.1.3. *The double DBD plasma actuator*

In a proof-of-concept study it was found that a single DBD actuator could give a moderate control effect on the separation but in order to achieve a stronger effect, a double DBD actuator was used for the flow separation control study. The design of the in-house built double actuator is described in detail in chapter 3 and it consists simply of two single actuators (type F) mounted in tandem as can be seen in figure 4.5. The double actuator was placed along the spanwise direction producing an electric wind in the streamwise direction, although the dielectric was applied all around the cylinder preventing any modification of the flow behavior that could be induced by a step at the cylinder surface. As mentioned previously, the position of the actuator could be varied by rotating the cylinder. The downstream edge of the downstream actuator – henceforth

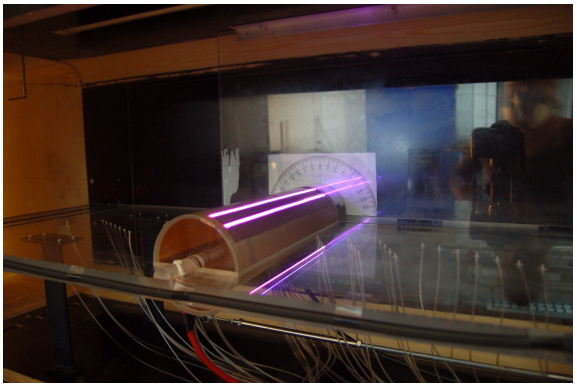

FIGURE 4.5. Photograph of the double DBD plasma actuator mounted on the cylinder. Flow is from left to right. Note that the magenta color on the plate is a reflection of the plasma light.

denoted as Actuator 1 – is at the angle θ from the leading edge of the cylinder. The downstream edge of the upstream actuator – Actuator 2 – is at the position $\theta - 20°$. The actuator was activated for most of the studies with a driving voltage of 10 kV_{p-p} and a driving frequency of 6 kHz resulting in a power consumption of about 40 W (including the power consumption of the actuator as well as the high-voltage generator type *Minipuls2* and the electric cables).

One of the difficulties encountered when using DBD plasma actuators is the electromagnetism they produce and electrical spikes induced in the ground loop of the electrical system when they happen to "burn" (*i.e.* when an electric arc goes through the dielectric material). These effects appeared strong enough to damage the driver of the traversing system used for this study even though no direct electric arc was produced from the plasma to the traverse or the probe mounted on the traverse. A solution was to isolate sensible devices, such as the driver and motor of the traverse from the electric main[7]. The drive was thus controlled from the measurement computer through an optical USB isolator plugged in between the USB port of the computer and the USB cable of the drive. Furthermore, a battery was used as power supply to the traverse avoiding connection with the electric main.

4.2. Drag evaluation

A common indirect way to estimate drag on a body is to evaluate the momentum loss of the flow across a body. We will here derive the drag based on such

[7]Personal communication with Tomas Modéer, Department of Electrical Energy Conversion, KTH.

an analysis for the two-dimensional case that has been used to estimate the drag with and and without control for the flow cases studied in this thesis.

We consider a control volume (CV) where the upstream control cross-sectional area (A_1), as seen in figure 4.2, is normal to the plate and has its origin at the leading edge of the plate. The downstream control cross-sectional area (A_2) is also vertical and placed at some downstream distance from the cylinder where the flow is assumed to be reattached. The control volume is closed with a curve following a streamline far from the plate and cylinder, and the bottom surface of the control volume is the impermeable horizontal wall and cylinder. Within the control volume the mass is conserved which can be expressed for incompressible flow as

$$U_1 A_1 = \int_{A_2} U_2 dA, \tag{4.8}$$

where U_1 is the constant and uniform streamwise velocity at the upstream side and U_2 is the velocity at the downstream side.

The momentum balance of the fluid inside the control volume can be expressed as the difference in flow momentum entering the CV through A_1 and the outflow of momentum through A_2, which entirely should be due to frictional and pressure forces acting on the boundaries of the CV. If we assume that the upper boundary of the CV is far away from the lower boundary such that the static pressure is constant (and equal to p_1) we can write the following expression describing the momentum conservation

$$p_1 A_2 + \rho U_1^2 A_1 = \int_{A_2} p_2 dA + \int_{A_2} \rho U_2^2 dA + D_x, \tag{4.9}$$

where D_x is the total drag force acting on the lower surface in the negative x-direction. This force includes both the friction drag on the flat surface and the cylinder as well as the pressure drag on the cylinder in the x-direction. We now introduce the dynamic pressure $q_1 = \frac{1}{2}\rho U_1^2$ and the momentum conservation can be rewritten as

$$\int_{A_2} \frac{p_1 - p_2}{q_1} dA + 2\int_{A_2} \frac{U_2}{U_1} dA = 2\int_{A_2} \frac{U_2^2}{U_1^2} dA + \frac{D_x}{q_1}, \tag{4.10}$$

where we also have used the mass conservation equation (4.8) to replace A_1 with the integral as shown by the second term on the left-hand side. Adding now the dynamic pressure q_1 to p_1 we obtain the total pressure $p_{tot,1} = p_1 + q_1$ and similar for $p_{tot,2} = p_2 + q_2$ we obtain after some algebra

$$\int_{A_2} \frac{p_{tot,1} - p_{tot,2}}{q_1} dA - \int_{A_2} \left(1 - \frac{U_2}{U_1}\right)^2 dA = \frac{D_x}{q_1}.$$

From an experimental point of view this is a convenient expression since the total pressure can easily be measured with a total pressure probe whereas the second integral needs accurate determination of the downstream velocity profile. A complication in the present experiments is that the extension of the test section of the wind tunnel in the direction normal to the plate is limited and therefore the assumption of constant pressure of the streamline forming the upper closing contour of the CV is not exact. However, we use this expression to compare the drag of the uncontrolled and controlled flow case, and thus the error, of same amplitude, is contained in both quantities.

Furthermore, the flow in this study is assumed two-dimensional, hence it is sufficient to do the integration in the direction normal to the plate, from the wall ($y = 0$) to some position y_2 far away from the plate. The drag per unit span (d_x) is then expressed as

$$\frac{d_x}{q_1} = \int_0^{y_2} \frac{p_{tot,1} - p_{tot,2}}{q_1} dy - \int_0^{y_2} \left(1 - \frac{U_2}{U_1}\right)^2 dy,$$

and we denote the drag coefficient as

$$C_d = \frac{d_x}{q_1(D/2)},$$

i.e. where the normalisation of C_d is made with the height of the bump.

However, one should be aware of that the streamwise momentum provided by the electric wind itself is not taken into account in the calculation.

4.3. Results

4.3.1. *Study of the baseline flow – Summary of results from paper 2*

- The turbulent character of the boundary layer developing upstream the cylindrical bump at $x/D = -2.5$ was verified. Comparison with Direct Numerical Simulation (DNS) data indicates that at that streamwise position there is a small favorable pressure gradient.
- A criterion based on the study of the mean streamwise component of the velocity measured by means of hot-wire anemometry was developed to identify the region were the flow is separated, *i.e.* the region with instantaneous back-flow. This criterion is based on observations that the location of the inflection point of the mean velocity coincides with the location of the maximum of the rms and the zero-crossing of the skewness at the upper limit of the separated region.
- The impact of the insensibility to the flow direction of hot-wire anemometry on the velocity spectra was observed and analyzed using a synthetic signal. Results show that a shift towards higher frequencies of the energy contained in the low frequencies in the separation region was a direct effect of measurement of back-flow with a hot-wire.

- The boundary layer separates on the cylindrical bump and comparison of the two cases with different inlet velocities ($U_0 = 8$ and 16 m/s and $Re_D = 50000$ and 100000, respectively) shows that the flow with the lower Reynolds number separates over a longer distance than for the higher Reynolds number case. The evolution in the streamwise direction of the flow velocity at the highest position from the wall was studied and showed a similar development for both Reynolds number cases up to the top of the cylinder position suggesting that blockage effects are not responsible for different behaviours between the two flow cases in the separation region.
- The development of an internal boundary layer could be observed at the top of the cylinder and appeared to be thinner for the higher Reynolds number.

4.3.2. *Drag reduction by separation control – Summary of results from paper 3*

- A parametric study showed that a double DBD plasma actuator with a driving voltage of 10 kV_{p-p} was necessary to impact control on the boundary layer separating from the half-cylinder bump at a Reynolds number of 33000.
- Results showed that the relative position of the actuator to the separation point is important, the best results were obtained close to $\theta = 105°$ for the present baseline flow. The actuator should be close enough, *i.e.* not too upstream or downstream as in the first case the electric wind produced will separate from the cylinder surface and only energize the shear layer and in the latter case the actuator is not able to reattach the flow. The results showed a drag reduction when the shear layer was energised as the upper part of the boundary layer at $x/D = 5$ was accelerated compared to the uncontrolled case but the C_p evolution showed that the separation region was not shorter. In the case when the actuator is situated close to the separation point, the base pressure of the half-cylinder bump is increased and the reattachment point moved upstream.
- The design of the actuator – two single DBD plasma actuators placed in tandem – needs also to be taken into account to interpret the results as two positions seem to be optimal for the flow control, one with both actuators upstream the separation point ($\theta = 95°$) and the second with the separation point being in between the two actuators but close enough from the most upstream actuator ($\theta = 115°$). In those two configurations, a drag reduction of about 30% was achieved.

CHAPTER 5

Outlook

The first step of this project was to learn about DBD plasma actuators and the physical aspects of the electric wind as well as to develop a manufacturing technique for in-house plasma actuators and demonstrate that they can be used to delay flow separation.

The results on the electric wind induced by the in-house DBD plasma actuators show that they produce an electric wind of several meters per second and respond to parameters variations, geometrical as well as electrical, in a similar manner as actuators built by other research groups. In still air we show that the actuators show potential for flow separation control on convex surfaces by introducing streamwise momentum since the electric wind (wall jet) follows the curved surface of a cylinder.

The control of flow separation from a half-cylinder bump protruding from a flat plate was achieved using a double DBD plasma actuator with the electrodes along the spanwise direction and thus the electric wind in the streamwise direction. Drag reduction was noticed by increasing the base pressure at the rear part of the bump if the actuator was placed close to the separation point. However, in this configuration, the plasma actuators were only able to reduce the length of the separation region for small Reynolds numbers. This limitation is of course related to the smallness of the momentum that is introduced through the plasma actuators close to the surface relative to the momentum of the separated flow itself. If this type of actuators should be successfully used on the A-pillars of trucks control must also be possible at higher Reynolds numbers (velocities).

Wall suction, vortex generators (both physical generators or blowing/suction from holes) or slots providing wall jets are all methods that can provide separation control. However, the plasma actuators have several advantages as compared to these, passive and active, control methods, *e.g.* they do not have any moving parts, they are not protruding from the surface and they can be shut off when not needed. However, the strength of the electric wind may not be large enough to provide enough momentum for successful control at high Reynolds numbers.

In an outlook for the continuation of the present project we are contemplating using plasma actuators in other actuator configurations for flow separation

control. Indeed, using a plasma array with electrodes oriented in the streamwise direction thereby inducing streamwise vortices seems to be a promising technique to delay separation in a similar way as has been shown by surface mounted vortex generators[8]. The mechanism in work for this configuration is to set up streamwise vortices that will mix high velocity fluid from the outer part of the boundary layer into the low velocity region close to the wall. If such vortices can be initiated by the actuators, the so called lift-up effect will start to work (see *e.g.* Landahl 1980) and even the rather small amount of momentum produced by the actuators will in this case not be a limiting factor.

Moreover, some complementary work will be done to develop more robust actuators to limit the degradation of the dielectric material and ensure a constant output from the actuators.

Finally, this first set of experiments confirmed the low power consumption of such actuators (about 40 W for 520 mm of actuation) but a quantitative study of the efficiency of the actuator to control the separation without overcoming the power reduction by its own power consumption is necessary to justify the use this active technique.

[8]A truck cannot use surface-mounted vortex generators protruding from *e.g.* the A-pillars since they could be dangerous for people at standstill or at low velocities. This is in contrast to aircraft where for instance Boeing regularly uses vortex generators on the wings for separation control at high angles of attack at start and landing.

CHAPTER 6

Papers and authors contribution

Paper 1

Phase-averaged measurements of the electric wind induced by a Single Dielectric Barrier Discharge plasma actuator
J. A. Vernet (JV), R. Örlü (RÖ), & P. H. Alfredsson (HAL)
submitted for journal publication.

This work is of experimental character and investigates the time-resolved electric wind produced by a Single Dielectric Barrier Discharge (SDBD) plasma actuator. Both the experimental setup and the measurements were performed by JV under supervision of RÖ and HAL, whereas the data analysis was performed by JV with support from RÖ. The writing was done by JV, with comments from RÖ and HAL. Parts of this work have been published in or (will be) presented at:

> *Flow control by means of plasma actuation – a study of the electric wind*
> J. Vernet, R. Örlü & P. H. Alfredsson
> **Svenska Mekanikdagar**
> 12–14 June 2013, *Lund, Sweden.*
>
> *Experimental study of the electric wind induced by a dielectric barrier discharge plasma actuator.*
> J. Vernet, R. Örlü, G. Efraimsson & P. H. Alfredsson
> **Proc. 4th Int. Conf. on Jets, Wakes and Separated Flows (ICJWSF–4)**
> 17–21 September 2013, *Nagoya, Aichi, Japan.*
>
> *On the pulsating electric wind of a Single Dielectric Barrier Discharge (SDBD) plasma actuator.*
> J. Vernet, R. Örlü & P. H. Alfredsson
> **67th Annual Meeting of the APS Division of Fluid Dynamics**
> 23–25 November 2014, *San Francisco, CA.*

Paper 2

A turbulent boundary layer with pressure gradient, curvature and separation – results from hot-wire measurements
J. A. Vernet (JV), R. Örlü (RÖ) & P. H. Alfredsson (HAL)
Technical Report.

This work is of experimental character and investigates the mean flow and turbulence statistics of a turbulent boundary layer under pressure gradient and curvature effects. Both the experimental setup and the measurements were performed by JV under supervision of RÖ and HAL, whereas the data analysis was performed by JV with support from RÖ. The writing was done jointly by JV and RÖ, with comments from HAL. Parts of this work have been presented at and are submitted for publication in:

> *Turbulent boundary layer upstream, over and downstream a cylindrical 2D bump*
> J. Vernet, R. Örlü & P. H. Alfredsson
> **Progress in Turbulence VI, Proceedings of the iTi Conference in Turbulence**
> 21–24 September 2014, *Bertinoro, Italy.*

Paper 3

Flow separation delay on trucks A-pillars by means of Dielectric Barrier Discharge plasma actuation
J. A. Vernet (JV), R. Örlü (RÖ) & P. H. Alfredsson (HAL)
submitted for journal publication.

This work is of experimental character and investigates the feasibility of Dielectric Barrier Discharge (DBD) plasma actuation for the purpose of flow separation delay on a generic model of a trucks A-pillar. Both the experimental setup and the measurements were performed by JV under supervision of RÖ and HAL, whereas the data analysis was performed by JV. The writing was done by JV, with comments from RÖ and HAL. Parts of this work have been presented at:

> *Flow separation delay on trucks A-pillars by means of Dielectric Barrier Discharge plasma actuation*
> J. Vernet, R. Örlü, P. H. Alfredsson & P. Elofsson
> **1st Int. Conf. Num. and Exp. Aerodyn. Road Vehicles and Trains, AEROVEHICLES 1**
> 23–25 June 2014, *Bordeaux, France.*

Acknowledgements

The project is financially supported by the Swedish Energy Agency within the project Flow Research on Active and Novel Control Efficiency (FRANCE), project number 34186-1, which is greatly acknowledged. The scholarship from the Foundation Erik Petersohns Minne which allowed me to participate to the iTi conference is very much appreciated.

First of all, I wish to express my deepest gratitude to my supervisor Prof. P. Henrik Alfredsson for giving me the opportunity to work with him on this doctoral project. Thank you for always taking the time to teach me (sometimes several times) the things I do not understand with always the same patience and enthusiasm, for the interesting discussions (about work or not) and putting so much effort to build a lab with such a good environment through the years. A special thanks goes also to my co-supervisor Dr. Ramis Örlü for his invaluable help and time he puts in every steps of this project, for always being available and show concern whenever problems are encountered and for his precious support in the mood-challenging periods. I am not always being fair under pressure but you never hold hard feelings! I also want to express my gratitude to you both for always showing confidence in my capacities even when I usually miss it myself.

I also would like to acknowledge the fruitful and always encouraging comments of my co-supervisor Prof. Gunilla Efraimsson. Together with Romain Futrzynski, Dr. Per Elofsson and Guillaume Mercier you have helped to the development of this thesis and I am thankful to be part of FRANCE with you.

Many thanks to Prof. Alessandro Talamelli for his interesting comments and advices on this licentiate thesis but also for always considering my comments when working together to the good development of the vehicle aerodynamics lab. I am also very thankful for giving me the opportunity to spend one week in Forli to follow the experiments you were running with plasma actuation when I started my PhD; this project could not have started on such good bases without this experience. Professors Andrea Cristofolini and Gabriele Neretti as well as Alessandro Rossetti, Luca Ginepri and Matteo Motecchia and are

also acknowledged for sharing their knowledge of plasma actuators design and wind tunnel experiments.

Dr. Hans Edin and Dr. Nathaniel Taylor from KTH School of Electrical Engineering are acknowledged for lending to us the high-voltage amplifier and being helpful with the setup of the electrical circuit. A special thanks to Tomas Modéer from KTH Electrical Energy Conversion who figured out the problems of spikes in the electric main and saved the automatic traverse 2.0 saving me from doing all measurements with a manual traverse...

Thanks to Dr. Nils Tillmark and Dr. Bengt Fallenius for keeping an order in the lab and being of great help whatever the question is; office, setup, material or physics! Nils, thanks for sharing the enthusiasm I have for my native country and bringing back to me whenever you can some very appreciated "home-reminder".

Our skillful toolmakers, Joakim Karlström, Göran Rådberg, Rune Lindfors and Jonas Vikström deserve a special thanks as running experiments would not be possible without their expertise and original ideas in designing and building setups.

Thank you Malin Landin for always being smiling and helpful whatever the subject or the problem is related to.

I wish to emphasize here the patience of Shintaro Imayama who had to share an office with a non-so-always-calm-even-sometimes-singing roommate... you definitely deserved the window side! Thanks Shintaro for all the fun moments we shared, I am looking forwards the new adventures of unstable guy and plasma girl in the US!

Last but not the least I wish to thank my past and present coworkers for creating such a friendly atmosphere at the lab, this is probably one of the main reason I like coming to work. I had so much fun experiencing science but also food diets and sport trainings with you! You have been an invaluable help, support and source of joy for the two and a half past years.

References

Albrecht, H.-E., Borys, M., Damaschke, N. & Tropea, C. 2003 *Laser Doppler and phase Doppler measurement techniques*. Springer-Verlag Berlin Heidelberg.

Barnard, R. H. 2009 *Road vehicle aerodynamic design - An introduction*, 3rd edn. MechAero Publishing, United Kingdom.

Bellan, P. M. 2008 *Fundamentals of plasma physics*. Cambridge University Press.

Benard, N., Debien, A. & Moreau, E. 2013 Time-dependent volume force produced by a non-thermal plasma actuator from experimental velocity field. *J. Phys. D: Appl. Phys.* **46**, 245201.

Benard, N. & Moreau, E. 2013 Response of a circular cylinder wake to a symmetric actuation by non-thermal plasma discharges. *Exp. Fluids* **54**, 1467.

Benard, N. & Moreau, E. 2014 Electrical and mechanical characteristics of surface AC dielectric barrier discharge plasma actuators applied to airflow control. *Exp. Fluids* **55**, 1846.

Boeuf, J. P., Lagmich, Y. & Pitchford, L. C. 2009 Contribution of positive and negative ions to the electrohydrodynamic force in a dielectric barrier discharge plasma actuator operating in air. *J. Appl. Phys.* **106**, 023115.

Boeuf, J. P., Lagmich, Y., Unfer, T., Callegari, T. & Pitchford, L. C. 2007 Electrohydrodynamic force in dielectric barrier discharge plasma actuators. *J. Phys. D: Appl. Phys.* **40**, 652–662.

Bradley, R. 2000 Technology roadmap for the 21st century truck program. *Tech. Rep.* 21CT-001.

Bruun, H. H. 1995 *Hot-wire anemometry principles and signal analysis*. Oxford University Press.

Choi, H., Lee, J. & Park, H. 2014 Aerodynamics of heavy vehicles. *Annu. Rev. Fluid Mech.* **46**, 441–468.

Clauser, F. H. 1956 The turbulent boundary layer. In *Advances in applied mechanics* (ed. H. L. Dryden & T. von Kármán), pp. 1–51. Academics Press Inc.

Coleman, H. W. & Steele, W. G. 2009 *Experimentation, validation, and uncertainty analysis for engineers*, 3rd edn. John Wiley & Sons, Inc., Hoboken, New Jersey.

Corke, T. C., Enloe, C. L. & Wilkinson, S. P. 2010 Dielectric barrier discharge plasma actuators for flow control. *Annu. Rev. Fluid Mech.* **42**, 505–529.

Debien, A., Benard, N., David, L. & Moreau, E. 2012 Unsteady aspect of the electrohydrodynamic force produced by surface dielectric barrier discharge actuators. *Appl. Phys. Lett.* **100**, 013901.

Dynamics, D. 2011 *LDA and PDA reference manual*.

Enloe, C. L., McHarg, M. G., Font, G. I. & McLaughlin, T. E. 2009 Plasma-induced force and self-induced drag in the dielectric barrier discharge aerodynamic plasma actuator. In *47th AIAA Aerospace Sciences Meeting Including The New Horizons Forum and Aerospace Exposition*. Orlando, Florida.

Enloe, C. L., McLaughlin, T. E., Van Dyken, R. D., Kachner, K. D., Jumper, E. J., Corke, T. C., Post, M. L. & Haddad, O. 2004 Mechanisms and responses of a dielectric barrier plasma actuator: Geometric effects. *AIAA J.* **42**, 595–604.

Erfani, R., Zare-Behtash, H. & Kontis, K. 2012 Plasma actuator: Influence of dielectric surface temperature. *Exp. Therm. Fluid Sci.* **42** (C), 258–264.

Forte, M., Jolibois, J., Pons, J., Moreau, E., Touchard, G. & Cazalens, M. 2007 Optimization of a dielectric barrier discharge actuator by stationary and non-stationary measurements of the induced flow velocity: application to airflow control. *Exp. Fluids* **43**, 917–928.

Fransson, J. H. M., Konieczny, P. & Alfredsson, P. H. 2004 Flow around a porous cylinder subject to continuous suction or blowing. *J. Fluid Struct.* **19**, 1031–1048.

Fridman, A. 2008 *Plasma Chemistry*. Cambridge University Press.

Giepman, R. & Kotsonis, M. 2011 On the mechanical efficiency of dielectric barrier discharge plasma actuators. *Appl. Phys. Lett.* **98**, 221504.

Greenblatt, D., Schneider, T. & Schüle, C. Y. 2012 Mechanism of flow separation control using plasma actuation. *Phys. Fluids* **24**, 077102.

Gad-el Hak, M. 2000 *Flow control: passive, active and reactive flow management*. Cambridge University Press.

Hanson, R. E., Houser, N. M. & Lavoie, P. 2014 Dielectric material degradation monitoring of dielectric barrier discharge plasma actuators. *J. Appl. Phys.* **115**, 043301.

Huang, J., Corke, T. C. & Thomas, F. O. 2006 Plasma actuators for separation control of low-pressure turbine blades. *AIAA J.* **44**, 51–57.

Hultgren, L. S. & Ashpis, D. E. 2003 Demonstration of separation delay with glow discharge plasma actuators. In *41st AIAA Aerospace Sciences Meeting and Exhibit*. Reno, Nevada: American Institute of Aeronautics and Astronautics.

Johansson, A. V. & Alfredsson, P. H. 1982 On the structure of turbulent channel flow. *J. Fluid Mech.* **122**, 295–314.

Jørgensen, F. E. 2002 *How to measure turbulence with hot-wire anemometers*.

Jukes, T. N. & Choi, K. S. 2009*a* Control of unsteady flow separation over a circular cylinder using dielectric-barrier-discharge surface plasma. *Phys. Fluids* **21**, 094106.

Jukes, T. N. & Choi, K. S. 2009*b* Flow control around a circular cylinder using pulsed dielectric barrier discharge surface plasma. *Phys. Fluids* **21**, 084103.

Jukes, T. N., Choi, K. S., Johnson, G. A. & Scott, S. J. 2006 Characterization of surface plasma-induced wall flows through velcoity and temperature measurements. *AIAA J.* **44**, 764–771.

Jukes, T. N., Choi, K. S., Segawa, T. & Yoshida, H. 2008 Jet flow induced by a surface plasma actuator. *P. I. Mech. Eng. I-J. Sys.* **222**, 347–356.

Jukes, T. N., Segawa, T. & Furutani, H. 2013 Flow control on a NACA 4418 using dielectric-barrier-discharge vortex generators. *AIAA J.* **51**, 452–464.

Jukes, T. N., Segawa, T., Walker, S., Furutani, H., Iki, N. & Takekawa, S. 2012 Active separation control over a NACA0024 by DBD plasma actuator and FBG sensor. *J Fluid Sci Technol.* **7**, 39–52.

Kim, W., Do, H., Mungal, M. G. & Cappelli, M. A. 2007 On the role of oxygen in dielectric barrier discharge actuation of aerodynamic flows. *Appl. Phys. Lett.* **91**, 181501.

Kotsonis, M. & Ghaemi, S. 2011 Forcing mechanisms of dielectric barrier discharge plasma actuators at carrier frequency of 625 Hz. *J. Appl. Phys.* **110**, 113301.

Kotsonis, M., Ghaemi, S., Veldhuis, L. & Scarano, F. 2011 Measurement of the body force field of plasma actuators. *J. Phys. D: Appl. Phys.* **44**, 045204.

Kriegseis, J., Schwarz, C., Tropea, C. & Grundmann, S. 2013 Velocity-information-based force-term estimation of dielectric-barrier discharge plasma actuators. *J. Phys. D: Appl. Phys.* **46**, 055202.

Labergue, A. 2005 Study of electric discharge in air for plasma actuator development - Application to the control of airflow detachment. PhD thesis, University of Poitiers, France.

Labergue, A., Leger, L., Moreau, E., Touchard, G. & Bonnet, J.-P. 2004 Experimental study of the detachement and the reattachement of an airflow along an inclined wall controlled by a surface corona discharge – application to a plana turbulent mixing layer. *IEEE T. Ind. Appl.* **40**, 1205–1214.

Landahl, M. T. 1980 A note on an algebraic instability of inviscid parallel shear flows. *J. Fluid Mech.* **98**, 1–9.

Langmuir, I. 1928 Oscillations in ionized gases. *Proc. Natl Acad Sci USA* **14**, 627–637.

Leger, L., Moreau, E., Artana, G. & Touchard, G. 2001 Influence of a DC corona discharge on the airflow along an inclined flat plate. *J. Electrostat.* **51**, 300–306.

Leonov, S., Opaits, D., Miles, R. B. & Soloviev, V. R. 2010 Time-resolved measurements of plasma-induced momentum in air and nitrogen under dielectric barrier discharge actuation. *Phys. Plasmas* **17**, 113505.

Ligrani, P. M. & Bradshaw, P. 1987 Spatial resolution and measurements of turbulence in the viscous sublayer using subminiature hot-wire probes. *Exp. Fluids* **5**, 407–417.

Likhanskii, A. V., Shneider, M. N., Macheret, S. O. & Miles, R. B. 2008 Modeling of dielectric barrier discharge plasma actuator in air. *J. Appl. Phys.* **103**, 053305.

Lögdberg, O., Angele, K. & Alfredsson, P. H. 2010 On the robustness of separation control by streamwise vortices. *Eur. J. Mech. B-Fluid* **29**, 9–17.

Mestiri, R., Hadaji, R. & Ben Nasrallah, S. 2010 An experimental study of a plasma actuator in absence of free airflow: Ionic wind velocity profile. *Phys. Plasmas* **17**, 083503.

Moreau, E. 2007 Airflow control by non-thermal plasma actuators. *J. Phys. D: Appl. Phys.* **40**, 605–636.

Moreau, E., Benard, N., Lan-Sun-Luk, J.-D. & Chabriat, J.-P. 2013 Electrohydrodynamic force produced by a wire-to-cylinder dc corona discharge in air at atmospheric pressure. *J. Phys. D: Appl. Phys.* **46**, 475204.

Moreau, E., Leger, L. & Touchard, G. 2006 Effect of a DC surface-corona discharge on a flat plate boundary layer for air flow velocity up to 25 m/s. *J. Electrostat.* **64**, 215–225.

Neumann, M., Friedrich, C., Czarske, J., Kriegseis, J. & Grundmann, S. 2012 Determination of the phase-resolved body force produced by a dielectric barrier discharge plasma actuator. *J. Phys. D: Appl. Phys.* **46**, 042001.

Nishida, H., Nonomura, T. & Abe, T. 2012 Numerical analysis on three-dimensional body force field of DBD plasma actuator. In *43rd AIAA Plasmadynamics and Lasers Conference*. New Orleans, Louisiana: American Institute of Aeronautics and Astronautics.

Örlü, R., Fransson, J. H. M. & Alfredsson, P. H. 2010 On near wall measurements of wall bounded flows – The necessity of an accurate determination of the wall position. *Prog. Aerosp. Sci.* **46**, 353–387.

Post, M. L. & Corke, T. C. 2004 Separation control on high angle of attack airfoil using plasma actuators. *AIAA J.* **42**, 2177–2184.

Roth, J. R. 2007 Physics and phenomenology of plasma actuators for control of aeronautical flows. *J. Phys. D: Appl. Phys.* **40**, Editorial.

Simpson, R. L. 1996 Aspects of turbulent boundary-layer separation. *Prog. Aerosp. Sci.* **32**, 457–521.

Smits, A. J., Monty, J., Hultmark, M., Bailey, S. C. C., Hutchins, N. & Marusic, I. 2011 Spatial resolution correction for wall-bounded turbulence measurements. *J. Fluid Mech.* **676**, 41–53.

Söderblom, D., Elofsson, P., Hjelm, L. & Löfdahl, L. 2012 Experimental and numerical investigation of wheel housing aerodynamics on heavy trucks. *SAE Int.* **5**, 29–41.

Söderblom, D., Löfdahl, L., Elofsson, P. & Hjelm, L. 2009 Heavy vehicle wheel housing flows – a parametric study. *SAE Tech Paper 2009-01-1169* .

Soloviev, V. R. 2012 Analytical estimation of the thrust generated by a surface dielectric barrier discharge. *J. Phys. D: Appl. Phys.* **45**, 025205.

Thomas, F. O., Corke, T. C., Iqbal, M., Kozlov, A. & Schatzman, D. 2009 Optimization of dielectric barrier discharge plasma actuators for active aerodynamic flow control. *AIAA J.* **47**, 2169–2178.

Trip, R. 2014 An experimental study on the wake behind a rectangular forebody with variable inlet conditions. Tekn. Lic. thesis, KTH Royal Institute of Technology, Stockholm, Sweden.

Velkoff, H. R. & Ketcham, J. 1968 Effect of an electrostatic field on boundary-layer transition. *AIAA J.* **6**, 1381–1383.

Versailles, P., Gingras-Gosselin, V. & Vo, H. D. 2010 Impact of Pressure and Temperature on the Performance of Plasma Actuators. *AIAA J.* **48**, 859–863.

Wood, R. 2006 A discussion of a heavy truck advanced aerodynamic trailer system. In *International Forum for Road Transport Technology (IFRTT) 9th International Symposium on Heavy Vehicle Weights and Dimensions*. Pennsylvania State University.

Part II

Papers

1

Paper 1

Phase-averaged measurements of the electric wind induced by a Single Dielectric Barrier Discharge plasma actuator

By Julie A. Vernet, Ramis Örlü, P. Henrik Alfredsson

Linné Flow Centre, KTH Mechanics, SE-100 44 Stockholm, Sweden

Submitted

An experimental study is conducted on the electric wind produced by a Single Dielectric Barrier Discharge (SDBD) plasma actuator placed at the top of a half cylinder. Laser Doppler Velocimetry (LDV) measurements were performed and results show — in accordance with previous studies — that increasing the driving voltage and frequency of the actuator increases the jet velocity and thus the momentum added by the actuator to the wall-jet. The focus of the present study is on the phase-resolved behavior of the electric wind, in particular, its two strokes. Phase-averaged LDV data reveal that while the velocity during both strokes remains positive, it is nearly twice as high as during the other stroke. The difference of behavior between the two strokes and its downstream and wall-normal evolution are mapped for various driving voltages and frequencies. Results indicate that the difference between the two strokes is observed only in the vicinity of the actuator and that it evens out further downstream, thereby justifying the assumption of a steady force in simulations to model the induced force.

1. Introduction

Since the early demonstration of a discharge plasma actuator by Roth *et al.* (2000), Dielectric Barrier Discharge (DBD) plasma actuators have shown interesting abilities for active flow control (Moreau 2007; Corke *et al.* 2010), and have experienced great popularity as apparent from the exponential growth of activities in this field (Roth 2007). A Single DBD (SDBD) is constructed from two electrodes, the active or air-exposed electrode on the top and the grounded, so-called covered, electrode on the bottom, separated by a dielectric material, as depicted in Fig. 1. As an alternating high-voltage current is applied to the active electrode, commonly a sine wave (Enloe *et al.* 2008; Benard & Moreau 2010), electrons drift back and forth between the edge of the exposed electrode and the dielectric surface. During this motion they ionize

the surrounding medium and a plasma is produced. Also the ions are affected by the electric field and the movements and collisions of the ions with the air molecules add momentum to the air. In this way a SDBD can be used for flow control, e.g. drag reduction and lift enhancement by separation control (Post & Corke 2004; Munday & Taira 2013), transition delay (Grundmann *et al.* 2007; Hanson *et al.* 2010) and turbulent boundary layer control (Choi *et al.* 2011) are all being investigated both experimentally and numerically by various research groups.

In order to model DBD plasma actuators and to be able to use them in an optimal way, knowledge of the flow induced by the plasma, *i.e.* the electric wind, and its dependence of various parameters, is necessary, (see e.g. the recent extensive review by Benard & Moreau 2012). Research groups investigate this phenomenon of momentum addition by measuring the body force produced by the actuator either directly through a laboratory balance (Hoskinson *et al.* 2008), or through indirect means, *e.g.* through the spatial evolution of the electric wind obtained through Pitot measurements (Moreau *et al.* 2008) and non-intrusive optical methods such as Particle Image Velocimetry (PIV) (Kotsonis & Ghaemi 2011) and Laser Doppler Velocimetry (LDV) (Neumann *et al.* 2012). Kriegseis *et al.* (2013) review different methods to estimate the force induced by the plasma actuator on its surrounding using the aforementioned pressure and velocity measurement techniques.

Even though the driving parameters and the employed materials for the actuators used by the different research groups differ, the general trends of their results of the time-averaged electric wind are usually in agreement. The driving parameters have been extensively investigated by Forte *et al.* (2007). They showed how the electric wind velocity can be increased by increasing the driving voltage and frequency. However this technique to increase the induced force is limited; a too high voltage value, the so-called saturation voltage (Thomas *et al.* 2009), and/or a too high frequency value, produce high heat losses inside the dielectric material making the electric wind velocity to saturate, which in turn results in a less efficient actuator. This important result has been confirmed through the years by Kotsonis *et al.* (2011) and Kriegseis *et al.* (2013). Thomas *et al.* (2009) and Soloviev (2011) also showed that the use of a dielectric material with a lower dielectric constant increases the voltage saturation of the actuator.

Enloe *et al.* (2004) investigated the influence of different geometric parameters of the DBD plasma actuators and showed that actuators with thinner exposed electrodes give a higher thrust generation. They also studied the width of the grounded electrode and concluded that a too narrow electrode could limit the expansion of the plasma and the induced thrust. Those results were confirmed by Forte *et al.* (2007) who also showed that the thickness of the dielectric also influences the body force production of the actuator as they induce higher electric wind velocities when the dielectric material is thinner, except for low voltages. They also concluded that a small gap between the

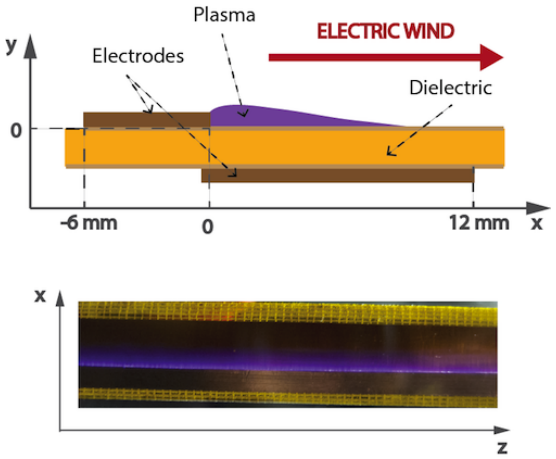

FIGURE 1. Description of the in-house built SDBD plasma actuator and coordinate system description. The bottom picture is a top view of the glowing discharge.

exposed and grounded electrodes is beneficial to the electric wind production. However, according to Post & Corke (2004) a small overlap of the electrodes allow a more homogeneous production of the plasma along the exposed electrode as it is challenging to manufacture actuators with the exact same gap all along the spanwise direction.

Since an alternating high-voltage power supply is necessary to sustain the discharge of the DBD plasma actuators, usually a sine wave or sawtooth wave, the electric wind can be thought of as an unsteady and periodic flow. Early experimental results on the time-resolved electric wind showed a positive velocity during both the forward and the backward strokes of the driving voltage cycle (Enloe *et al.* 2004); the forward stroke corresponding to the negative half-cycle, *i.e.* the exposed electrode is negatively charged, when the backward stroke is the positive half-cycle, *i.e.* the exposed electrode is the cathode. However simulation studies gave confusing results at first as only nitrogen gas was considered in the surrounding of the plasma actuator (Boeuf *et al.* 2007). Thus only positive ions were thought to be responsible for the momentum transfer and these are mainly present during the backward stroke. Kim *et al.* (2007) and Leonov *et al.* (2010) compared electric wind speeds during the two strokes in the presence of air or only nitrogen gas and showed the importance of the negative ions in the momentum transfer action of the plasma actuators. Indeed, in the case of only nitrogen gas, production of negative ions is not possible, positive ions are mainly produced during the backward stroke and almost no momentum is transferred to the surrounding during the forward stroke. When the medium is air, the forward stroke appears to produce more momentum than the backward

stroke highlighting the importance of the negative ions in high concentration during that phase. Simulations of Boeuf *et al.* (2009) confirm those results showing that there are more negative ions during the forward stroke and more positive ions during the backward strokes. Experiments of Thomas *et al.* (2009) and simulations of Soloviev (2011) also highlight the importance of the role of the negative ions in the momentum production process. The results of those studies explain that even though the electrons are moving in different directions during the two strokes, the electric wind production is due to ions with different polarities and thus always in the same direction.

A new challenge of the study of the electric wind is to determine if, even though the electric wind always flows in the same direction, the body force, the so-called electrohydrodynamic (EHD) force induced by the electric wind, is always in the same direction. Most groups working on that question utilize the definition of Corke *et al.* (2010) to qualify the body force induced by their plasma actuators: the force is qualified of a 'push' if it is directed in the positive streamwise direction, thus away from the exposed electrode, and as a 'pull' if it is in the negative streamwise direction. Two types of actuator behaviors emerged from recent studies, although there seem to be a consensus that the forward stroke is producing a strong 'PUSH' — where the capital letters emphasize the fact that the amplitude of the force is stronger — they disagree whether the backward stroke is producing a 'push' or a 'pull'. The studies of Leonov *et al.* (2010) and Neumann *et al.* (2012) show a PUSH-pull behavior, whereas Debien *et al.* (2012) compared DBD plasma actuators built with different electrode geometries and concluded that the type of EHD force produced by the plasma is dependent on the top electrodes shape: plate-shape exposed electrodes induce a PUSH-pull force while a wire-shape exposed electrode gives a PUSH-push behavior. Kotsonis & Ghaemi (2011) show that the type is dependent on the driving voltage waveform, obtaining a PUSH-push force in the case of a sine wave and a positive sawtooth signal, a PUSH-pull force for the square wave and a PUSH-none force for the negative sawtooth signals. Many other studies, both experimental and numerical classified their actuators as a PUSH-push behavior as *e.g.* Forte *et al.* (2007), Likhanskii *et al.* (2008), Enloe *et al.* (2009), Boeuf *et al.* (2009) and Nishida *et al.* (2012). However, since there is a need to look closer into the time-resolved force trace in order to conclude on the type of force it is challenging to do it for several locations in the electric wind and — to the authors' knowledge — no spatial evolution of the behavior of the force has been presented in the literature.

In the present study, the mean streamwise velocity profiles and their streamwise development induced by in-house built DBD plasma actuators are investigated and the effect of driving voltage, frequency and dielectric thickness on the electric wind. In particular, LDV measurements are performed in order to resolve the time evolution and study the probability density distributions of the induced electric wind with the aim to further understand the dependency of

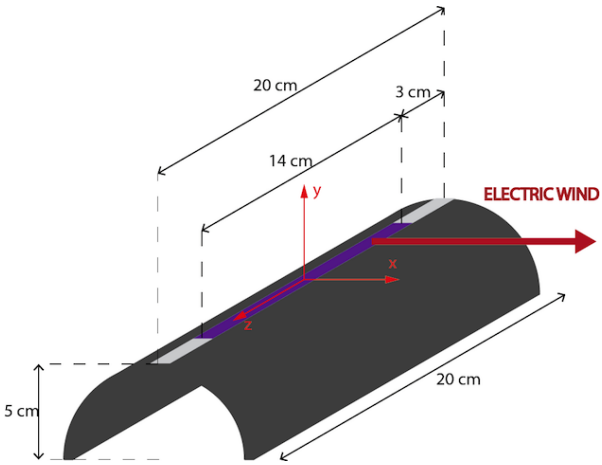

FIGURE 2. SDBD Plasma actuator mounted at the top of the half-cylinder.

these mechanisms on the various involved parameters, the driving parameters but in particular the spatial position. The present mean flow data will also serve for validation purposes of a numerical model of the actuator force used in a companion project (Futrzyncki *et al.* 2013).

2. Experimental setup

2.1. *The SDBD plasma actuator*

In the present study we use 66 μm thick adhesive copper foil for the two 14 cm long rectangular electrodes disposed asymmetrically on each side of the dielectric material. In order to ensure a homogeneous plasma generation along the spanwise direction, the electrodes are overlapping with about 0.5 mm as suggested by Post & Corke (2004). The exposed electrode is 6 mm wide in the streamwise direction whereas the bottom electrode is 13 mm, in order not to limit the streamwise length of the plasma. The dielectric sheet of the actuator is made of two layers of adhesive Kapton, 70 μm thick each, separated by a 0.25 mm thick sheet of Mylar. The dielectric material is thus 0.39 mm thick resulting in a total thickness for the actuator of 0.52 mm. The spanwise length of the dielectric is 6 cm longer than the actuation length, with 3 cm on each side as shown in Fig. 2, to avoid spark generation between the electrodes on the sides of the actuator and to ensure operator safety.

To produce the high-voltage alternating current needed to sustain the discharge produced by the SDBD plasma actuator, a combination of a low amplitude sinusoidal signal generator and a high voltage amplifier is used. The gain of the amplifier is 2000 and it can output peak-to-peak voltages up to

20 kV_{p-p}. However, the slew rate of the present amplifier limits the driving frequency (f_d) to values lower than or equal to 2 kHz. Finally, the amplified high-voltage output, referred to as the driving voltage (V_d), is connected to the exposed electrode of the plasma actuator whereas the covered electrode is grounded.

2.2. *Test case and LDV measurement setup*

For the purpose of the present paper, the SDBD actuator is placed on the top of a half-cylinder made of Plexiglas, as schematized in Fig. 2. The covered electrode is thus embedded between the dielectric and the cylinder surface. This geometry was chosen since it is relevant for forthcoming separation control experiments. The cylinder is placed inside a large Plexiglas box in order to reduce disturbances from the surroundings on the electric wind. The box was mounted on a manual traversing table with a precision of 0.05 mm to be able to translate it in the streamwise direction.

Laser Doppler Velocimetry has been employed to record the velocity of the airflow using a single-component Dantec Dynamic LDV FlowLite system with a BSA 60 processor. The measurement volume is created by the intersection of two 632.8 nm wavelength laser beams. The focal length of the laser optics is 160 mm and the part of the box separating the laser head from the plasma actuator was built in glass in order to minimize optical distortions. The LDV laser head was attached to the vertical axis of an ISEL C142-4 traversing system that could be controlled with the measurement software. As seeding particles, diethylhexylsebacate (DEHS) droplets with a nominal diameter of about 1 μm is produced by a twin-fluid atomizer, and is continuously fed into the bow. DBD plasma actuators induce what is called a 'cold' plasma, *i.e.* the temperature of the plasma is only few degrees higher than the ambient temperature. The relaxation time of the DEHS particles is estimated to be around 2 μs allowing the particles to follow flow oscillations to frequencies higher than 8kHz with a particle response of 99% (Albrecht *et al.* 2003).

2.3. *LDV data analysis and signal reconstruction*

50000 samples were recorded for each measurement point with an average sampling rate of around 2000 particles/sec. The transit-time weighting method has been employed to evaluate statistical quantities (Albrecht *et al.* 2003). Due to the high value of the driving frequency and the limitations of the sampling rate of the LDV system, only few samples could be collected for each cycle or period of the driving current. For the phase, *i.e.* ensemble, averages, the period was divided into 200 bins over which Chauvenet's criterion was applied (Coleman & Steele 2009) to remove eventual outliers; less than 1% of the samples was discarded by the criterion.

3. Electric wind study and description

3.1. *Parametric study of the induced mean flow field*

As outlined in the introduction, the driving voltage and frequency as well as the thickness of the dielectric have been shown to have a strong effect on the electric wind. These parameters will henceforth be investigated in the present study, in particular, the following parameter space will be explored:

- The driving voltage applied between the two electrodes (V_d):
  $4 < V_d < 18$ kV$_{p-p}$,
- The driving frequency (f_d):
  $0.5 < f_d < 2$ kHz,
- The thickness of the dielectric (δ):
  $\delta_1 = 0.39$ mm and $\delta_2 = 0.49$ mm.

3.1a. *Effect of the driving voltage on the mean electric wind.* The mean streamwise component (U) of the wall-normal (or rather vertical) velocity profile for the different driving voltages is depicted in Fig. 3. In this figure, the profiles were recorded 8 mm downstream of the edge of the exposed electrode and with a driving frequency of 1 kHz. For a driving voltage of $V_d = 4$ kV$_{p-p}$ no discharge could be observed on the surface of the actuator and the LDV measurements revealed no induced wind, *i.e.* the driving voltage was too low for the discharge to initiate. However, for $V_d = 6$ kV$_{p-p}$, a small velocity was observed indicating that the breakdown voltage (Corke *et al.* 2010) resides between 4 and 6 kV$_{p-p}$. As shown previously by Forte *et al.* (2007), the flow field induced is similar to wall-jets and the maximum measured velocity of the jet increases with the driving voltage with values from 0.13 m/s to 3.67 m/s for the 6 to 16 kV$_{p-p}$ cases, respectively. However when the driving voltage increased to 18 kV$_{p-p}$, the discharge became unstable, plasma filaments and sparks were visible and after a few minutes the actuator got damaged. Figure 3 also shows that the maximum velocity of the jet moves closer to the surface of the cylinder (which is at $y = -0.66$ mm for $x = 8$ mm) when the voltage increases. The maximum velocities of the jet were not recorded for the cases of $V_d = 14$ and 16 kV$_{p-p}$ since they were closer to the wall than we were able to measure. This would also imply that velocities higher than 3.67 m/s can be induced by the present actuator at the streamwise position of $x = 8$ mm.

3.1b. *Effect of the driving frequency on the mean electric wind.* By increasing the driving frequency at a constant driving voltage the induced jet velocities increased as well, see Fig. 4. The increase of f_d from 0.5 to 1 kHz seems to have a larger effect than the increase from 1 to 2 kHz. However this could be due to the slew rate of the amplifier and thus its abilities to follow the voltage variations for high frequencies.

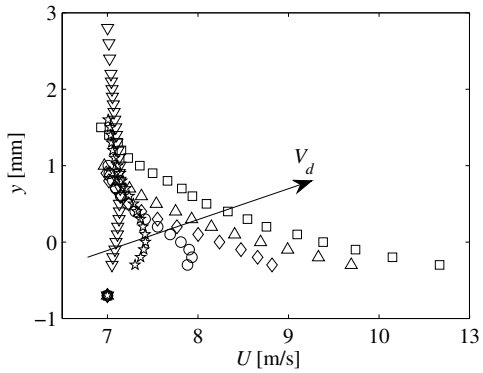

FIGURE 3. Evolution of the mean wall-normal velocity profiles at $V_d = 6$ kV$_{p-p}$ ($\triangledown$), 8 kV$_{p-p}$ ($\star$), 10 kV$_{p-p}$ ($\circ$), 12 kV$_{p-p}$ ($\diamond$), 14 kV$_{p-p}$ ($\triangle$), 16 kV$_{p-p}$ ($\square$), with $f_d = 1$ kHz. The arrow indicates increasing V_d. Profiles are recorded at $x = 8$ mm thus the wall position is at $y = -0.66$ mm.

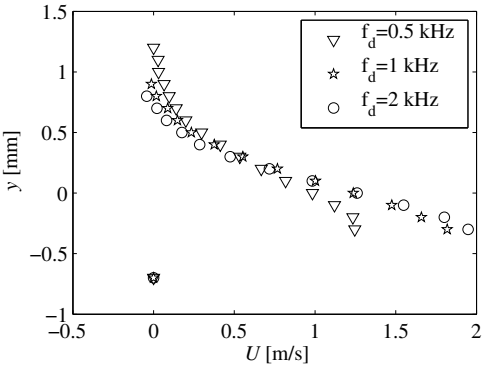

FIGURE 4. Evolution of the mean wall-normal velocity profiles for different driving frequencies, with $V_d = 1$ kV$_{p-p}$. Profiles are recorded at $x = 8$ mm thus the wall position is at $y = -0.66$ mm.

3.1c. *Effect of the dielectric thickness on the mean electric wind.* Only for this part of the study another actuator has been built which will be denoted *Act. 2*. While the dielectric thickness of the actuator used for the whole study (*Act. 1*) is $\delta_1 = 0.39$ mm, *Act. 2* has a 0.49 mm-thick dielectric material (δ_2), using a 0.35 mm-thick Mylar sheet in stead of the one of 0.25 mm thickness. Comparison of results obtained for the two different dielectric thicknesses using driving voltages of 6, 12 and 16 kV$_{p-p}$ are shown in Fig. 5. The wall position was

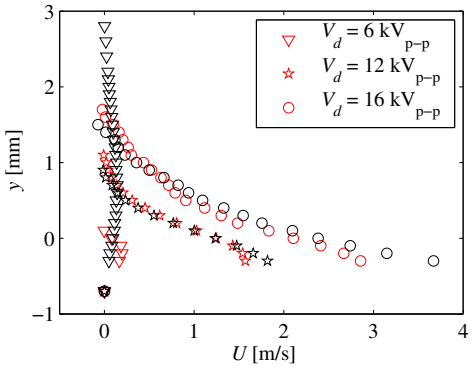

FIGURE 5. Evolution of the mean wall-normal velocity profiles for different dielectric thicknesses at various driving voltages (6, 12 and 16 kV$_{p-p}$) with $f_d = 1$ kHz. The black profiles correspond to the thinner dielectric material (*Act.1* , $\delta_1 = 0.39$ mm) and the red profiles to the thicker dielectric material (*Act. 2*, $\delta_2 = 0.49$ mm). Profiles are recorded at $x = 8$ mm thus the wall position is at $y = -0.66$ mm.

different for the two actuators since the *Act. 2* is 0.1 mm thicker than *Act. 1*. According to the literature (Forte *et al.* 2007), thicker dielectric layers usually allow the use of higher voltages thereby inducing stronger wall jets. However, in our case the discharge of *Act. 2* also became unstable for V_d=18 kV$_{p-p}$, limiting the increase of the driving voltage. Looking at the induced flow field one can notice that slightly lower velocities are induced when using *Act. 1* for the driving voltage 6 kV$_{p-p}$ but for V_d = 12 and 16 kV$_{p-p}$, the reverse conclusion can be drawn. These results are in agreement with the observations of Forte *et al.* (2007). Since *Act. 1* was able to produce stronger wall jets for most of the tested driving voltages, it has been selected as the one that will be used for future separation control experiments.

3.1d. *Streamwise evolution of the mean electric wind.* In Fig. 6, the streamwise development along the cylinder is shown using a driving voltage at 12 kV$_{p-p}$ and a driving frequency of 1 kHz. Unfortunately the present set up did not allow measurements close to the cylinder surface but the results still show that the flow follows the cylinder surface. This is one of the advantages with the flexibility of the actuators, namely that they can be made to adopt to the shape of the surface and can thus produce a jet that is oriented tangentially to the surface.

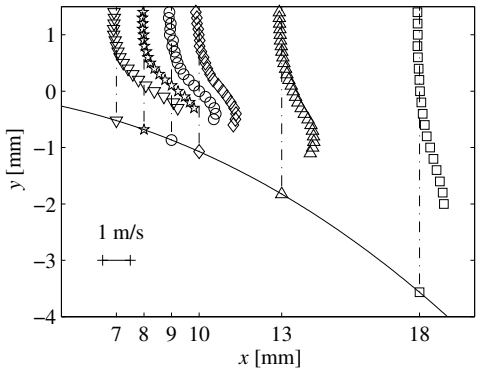

FIGURE 6. Evolution of the mean wall-normal velocity profiles for different x-positions. The cylinder wall is represented by the solid line. $V_d = 12\text{kV}_{p-p}$, $f_d = 1$ kHz.

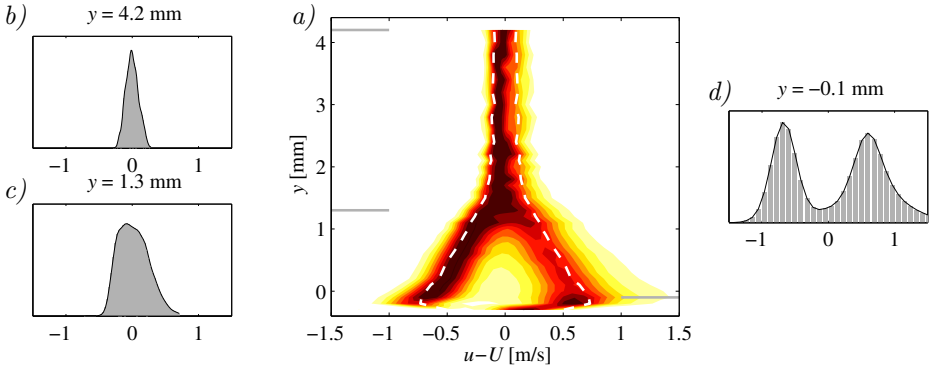

FIGURE 7. *a)* Color map of the velocity pdf (mean velocity substracted) as a function of the y-position for $x = 7$ mm, $V_d = 16$ kV_{p-p} and $f_d = 1$ kHz. The pdf are scaled by their maximal value. The white dashed lines represent the standard deviation around the mean of the time-series. The grey horizontal lines indicate the y-position of the pdf displayed in *b)*, *c)* and *d)*. *b)* 2D-plot of the velocity pdf at $y = 4.2$ mm (example of uni-modal pdf shape). *c)* 2D-plot of the velocity pdf at $y = 1.3$ mm (example of transitional pdf shape). *d)* 2D-plot of the velocity pdf at $y = -0.1$ mm (example of bi-modal pdf shape).

3.2. *Phase-averaged results*

Due to the high frequency driving voltages and the associated low number of samples per cycle, the probability density function (pdf) of the velocity signal is a convenient quantity to be studied instead of the time-series data. We therefore consider the spatial development of the pdf of the streamwise velocity in the following. Figure 7*a)* is a color map showing the variation of the pdf along a vertical direction at the streamwise position $x = 7$ mm. The map shows a bi-modal behavior of the pdf for positions close to the wall ($y \leq 1$ mm) and seems to disappear as we go away from the cylinder surface. Three characteristic types of pdf have been highlighted depending on the measurement point location: a narrow (or pointy) uni-modal pdf as can be observed in Fig. 7*b)*, a broad uni-modal pdf as present in Fig. 7*c)* and a bi-modal one as evident in Fig. 7*d)*. Note that the mean value of the velocity (2.84 m/s in the case of Fig. 7*d)*) has been subtracted). This shows that the velocity is always in the positive x-direction confirming the common belief as described in the introduction.

In order to study how the DBD excites the flow, the time signal from the LDV was used to reconstruct the velocity waveform during one period and was then phase, *i.e.* ensemble, averaged yielding the results shown in Fig. 8*a)*. This figure shows both the phase averaged variations in white and the normalised pdf of the velocity in each bin (colormap) giving an indication of the spread of the data. One can appreciate how the signal is divided into two different segments, a large increase in velocity is observed during the first half of the period (forward stroke), whereas after the decay a second but smaller increase can also be observed (backward stroke). The pdf plots in Figure 8*b)* clearly show that the bi-modal behavior is coupled to the forward and backward strokes of the driving signal.

Orlov *et al.* (2008) studied the three-dimensionality of the plasma discharge using images of the plasma taken with high-speed cameras. Similar effects were studied in the numerical model of Nishida *et al.* (2012). The discharge is different during the forward and backward stroke of the driving current; inspection by eye shows that the discharge appears homogeneous but during the forward stroke it is made of glow-type discharges while during the backward stroke the plasma is composed of filaments. Both the glow-type discharges and the filaments appear at discrete locations along the exposed electrode inducing three-dimensional variations in the plasma formation and those locations vary from one driving cycle to another resulting in cycle-to-cycle variations. The spread of the pdf around the phase-averaged mean value is most probably a result of those cycle-to-cycle variations of the plasma generation.

Fig. 8*c)* shows the acceleration derived from the phase-averaged velocity using a fourth-order central-difference scheme. As apparent, the induced flow shows a positive acceleration twice during a period, one during each stroke, with the first (in the figure) acceleration being much stronger than the second.

This clearly indicates a PUSH-push behavior of the present set up. Research groups noticing a PUSH-pull behavior of their actuator observe an increase of the velocity of the electric wind only during the forward stroke; there is no positive acceleration of the electric wind during the backward stroke. Thus the terms PUSH-push and PUSH-pull are employed to differentiate two 'types' of set up but the full behavior of the electric wind cannot be reduced to this simple description. As apparent from Fig. 8 the two 'push' phases are counteracted by two 'pull' phases appearing at the middle of each stroke probably due to the quenching of the plasma and the drag force on the cylinder surface.

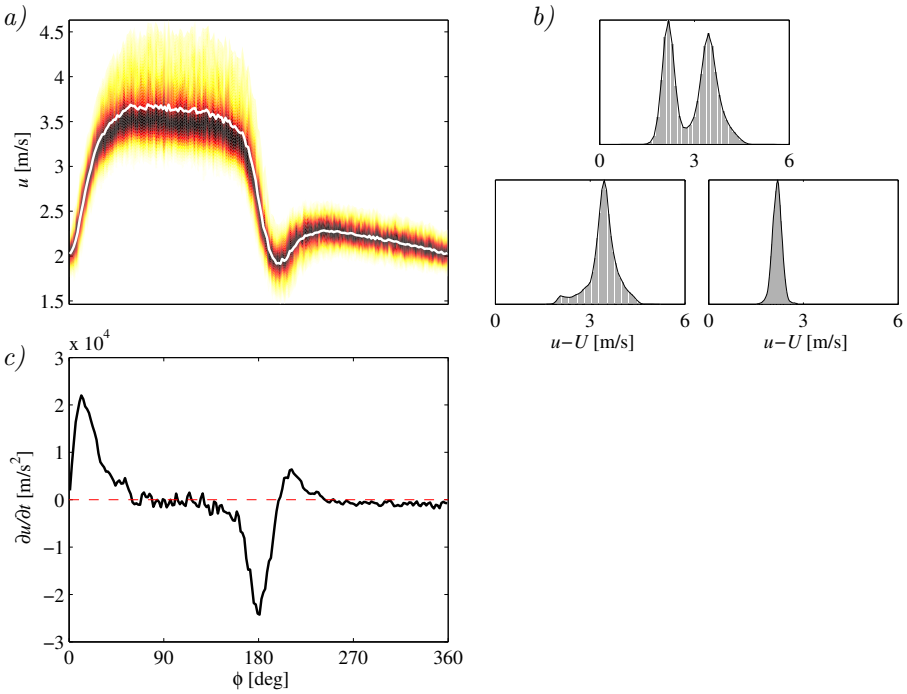

FIGURE 8. *a)* Colormap of the pdf of the data in each bin the signal has been decomposed into after applying the Chauvenet's criterion and phase-averaged velocity in white. Time-series recorded at $x = 7$ mm, $y = -0.1$ mm with $V_d = 16$ kV$_{p-p}$ and $f_d = 1$ kHz.*c)* Flow acceleration obtained from derivation of the phase-averaged velocity signal. *b) Top:* Pdf of the entire set of data. *Bottom left:* Pdf of the data recorded during the forward stroke (from 0 to 180 deg). *Bottom right:* Pdf of the data recorded during the backward stroke (from 180 to 360 deg).

The PUSH-push behavior is only noticeable when a bimodal pdf is evident. On the other hand, when the velocity pdf is unimodal, the velocity is constant along the period showing that the electric wind reached a more stable state at this position, independent from the driving current. To further understand how the jet is becoming stable or fully developed, a spatial map of the velocity pdf has been compiled in Fig. 9; in this case the mean value has not been subtracted, *i.e.* the pdf of the absolute signal is considered. This also avoids misinterpreting the cause for the bimodal behaviour of the pdf; the non-presence of the electric wind as for high y-positions obviously also results in an unimodal behavior but is not of interest. It can be observed that the PUSH-behavior is clearly visible for the most upstream profiles, the closest to the actuator and become weaker until it totally disappears advancing downstream. This is also visible on Fig. 10 where the pdf of the velocity at three different downstream positions has been plotted for two different driving voltages, 12 and 16 kV_{p-p}. It is clearly seen that for the higher voltage the bi-modal distribution is sustained further downstream than for the lower voltage; simply due to the higher velocity which causes the wall-jet to prevail further downstream. For the most upstream position, $x = 7$ mm, both pdfs are bi-modal while at $x = 10$ mm the pdf at $V_d = 12$ and 16 kV_{p-p} is uni-modal. This indicates that even though the body force produced by DBD plasma actuators is unsteady, few millimetres downstream the exposed electrode it can be considered as steady which is an advantage for both experimental use and to model the plasma actuation for simulation purposes.

Finally the variations of the pdf at a specific position for different driving voltages and for driving frequencies are illustrated in Figs. 11–12. It is shown that the development length of the wall jet changes with the strength of the driving voltage, a low voltage will result in a shorter penetration length of the

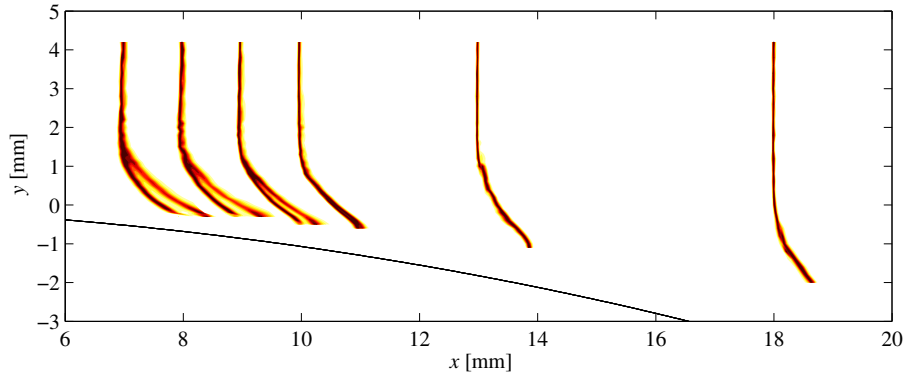

FIGURE 9. Map of the spatial evolution of the velocity pdf. Measurements realized with $V_d = 16$ kV_{p-p} and $f_d = 1$ kHz.

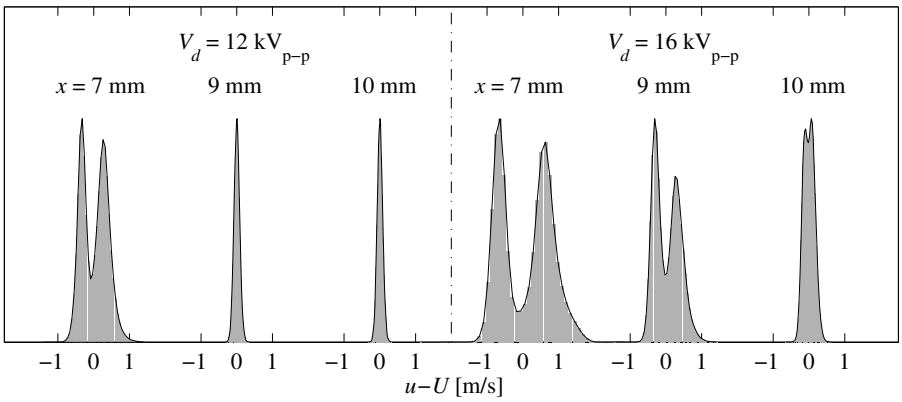

FIGURE 10. Pdf of velocity at three downstream positions (x = 7, 9, 10 mm), $y = -0.1$ mm, for two different driving voltages; at the left of the dashed line 12 kV, at the right 16 kV.

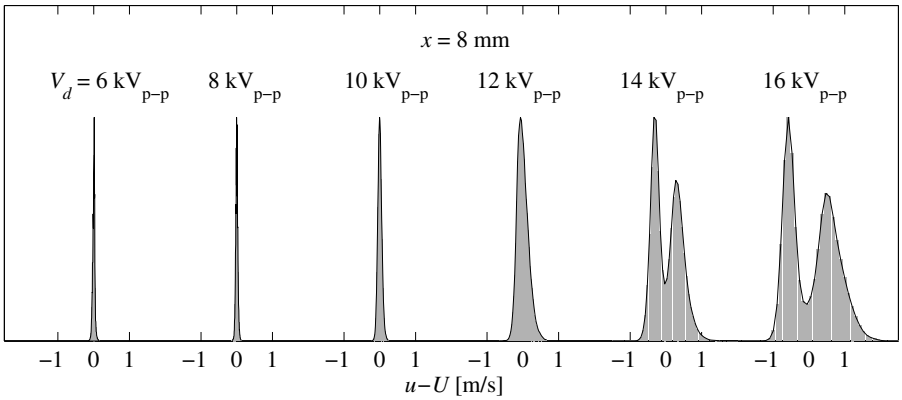

FIGURE 11. Pdf of velocities for different driving voltages at the driving frequency f_d = 1 kHz and position x = 8 mm and y = –0.1 mm.

wall jet and a smaller variation around the mean. However, recall that the mean velocity decreases with decreasing strength of the voltage. On the other hand, the opposite happens when increasing the driving frequency. For f_d = 2kHz, the electric wind reaches a more stable state faster than for f_d = 0.5 kHz and in this case the mean velocity increases with the driving frequency.

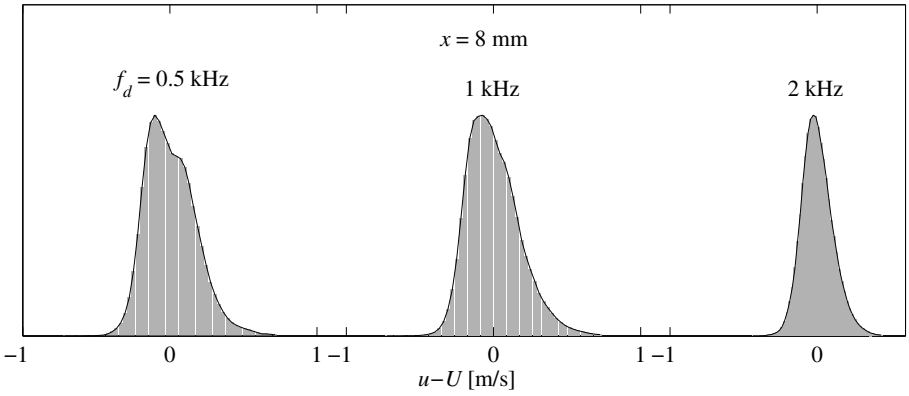

FIGURE 12. Pdf of velocities for different frequencies at the driving voltage $V_d = 12$ kV_{p-p} and position $x = 8$ mm and $y = -0.2$ mm.

4. Summary and conclusions

In this work a DBD plasma actuator has been developed and the induced airflow characterized through LDV measurements. The results and conclusions can be summarized as follows:

- Jet velocities increase with driving voltage and frequency. The extremity of the wall jet (maximum velocity) moves closer to the wall when the driving voltage increases.
- The thinner dielectric used produces higher jet velocities for almost all the voltages of interest.
- The jet is found to follow the surface of the cylinder.
- The bi-modal behavior of the pdf as well as the phase-averaged measurements are in accordance with the two strokes (forward and backward) of the voltage cycle. This shows that for the present configuration the actuator behaves according to the PUSH-push mechanism with two accelerations of the electric wind during each cycle.
- The measurements for each cycle display a large spread around the ensemble averaged data, which is probably related to the three-dimensional character of the plasma discharge.
- As we move downstream the bi-modal character of the electric wind vanishes and thus it becomes more stable. This development length depends on the driving parameters of the actuation: the electric wind is longer to become stable when the driving voltage is high and the driving frequency low.

In our future work the present actuator set up will be used to control separation in a bluff body experiment, and to develop a numerical model of the force produced by the actuators for implementation in numerical control studies.

Acknowledgments

The work was financially supported by the Swedish Energy Agency within the project Flow Research on Active and Novel Control Efficiency (FRANCE), project number 34186-1. Per Elofsson and Guillaume Mercier of Scania AB are acknowledged for useful input to the project. Professors Andrea Cristofolini, Alessandro Talamelli, Gabriele Neretti as well as Alessandro Rossetti, Luca Ginepri and Matteo Motecchia are acknowledged for discussion on the SDBD plasma actuator design and demonstration of their setup in the wind tunnel in Forli. The authors are thanking Dr. Hans Edin from KTH School Electrical Engineering for lending the high-voltage amplifier.

References

Albrecht, H.-E., Borys, M., Damaschke, N. & Tropea, C. 2003 *Laser Doppler and Phase Doppler Measurements Techniques*. Springer.

Benard, N. & Moreau, E. 2010 Capabilities of the dielectric barrier discharge plasma actuator for multi-frequency excitations. *J. Phys. D: Appl. Phys.* **43**, 145201.

Benard, N. & Moreau, E. 2012 EHD Force and Electric Wind Produced by Plasma Actuators Used for Airflow Control. In *6th AIAA Flow Control Conference*. New Orleans, Louisiana: American Institute of Aeronautics and Astronautics.

Boeuf, J. P., Lagmich, Y. & Pitchford, L. C. 2009 Contribution of positive and negative ions to the electrohydrodynamic force in a dielectric barrier discharge plasma actuator operating in air. *J. Appl. Phys.* **106**, 023115.

Boeuf, J. P., Lagmich, Y., Unfer, T., Callegari, T. & Pitchford, L. C. 2007 Electrohydrodynamic force in dielectric barrier discharge plasma actuators. *J. Phys. D: Appl. Phys.* **40**, 652–662.

Choi, K. S., Jukes, T. N. & Whalley, R. D. 2011 Turbulent boundary-layer control with plasma actuators. *Phil. Trans. R. Soc. A* **369**, 1443–1458.

Coleman, H. W. & Steele, W. G. 2009 *Experimentation, Validation, and Uncertainty Analysis for Engineers*, 3rd edn. John Wiley & Sons, Inc.

Corke, T. C., Enloe, C. L. & Wilkinson, S. P. 2010 Dielectric Barrier Discharge Plasma Actuators for Flow Control. *Annu. Rev. Fluid Mech.* **42**, 505–529.

Debien, A., Benard, N., David, L. & Moreau, E. 2012 Unsteady aspect of the electrohydrodynamic force produced by surface dielectric barrier discharge actuators. *Appl. Phys. Lett.* **100**, 013901.

Enloe, C. L., McHarg, M. G., Font, G. I. & McLaughlin, T. E. 2009 Plasma-induced force and self-induced drag in the dielectric barrier discharge aerodynamic plasma actuator. In *47th AIAA Aerospace Sciences Meeting Including The New Horizons Forum and Aerospace Exposition*. Orlando, Florida.

Enloe, C. L., McHarg, M. G. & McLaughlin, T. E. 2008 Time-correlated force production measurements of the dielectric barrier discharge plasma aerodynamic actuator. *J. Appl. Phys.* **103**, 073302.

Enloe, C. L., McLaughlin, T. E., Van Dyken, R. D., Kachner, K. D., Jumper, E. J., Corke, T. C., Post, M. L. & Haddad, O. 2004 Mechanisms and

Responses of a Dielectric Barrier Plasma Actuator: Geometric Effects. *AIAA J.* **42**, 595–604.

Forte, M., Jolibois, J., Pons, J., Moreau, E., Touchard, G. & Cazalens, M. 2007 Optimization of a dielectric barrier discharge actuator by stationary and non-stationary measurements of the induced flow velocity: application to airflow control. *Exp Fluids* **43**, 917–928.

Futrzyncki, R., Efraimsson, G. & Alfredsson, P. H. 2013 Numerical simulation of a plasma actuator on a half-submerged cylinder. In *Proc. 4th Int. Conf. on Jets, Wakes and Separated Flows (ICJWSF–4), September 17–21*. Nagoya, Aichi, Japan.

Grundmann, S., Klumpp, S. & Tropea, C. 2007 Experimental and Numerical Investigations of Boundary-Layer Influence Using Plasma-Actuators pp. 1–13.

Hanson, R. E., Lavoie, P., Naguib, A. M. & Morrison, J. F. 2010 Transient growth instability cancelation by a plasma actuator array. *Exp Fluids* **49**, 1339–1348.

Hoskinson, A. R., Hershkowitz, N. & Ashpis, D. E. 2008 Force measurements of single and double barrier DBD plasma actuators in quiescent air. *J. Phys. D: Appl. Phys.* **41**, 245209.

Kim, W., Do, H., Mungal, M. G. & Cappelli, M. A. 2007 On the role of oxygen in dielectric barrier discharge actuation of aerodynamic flows. *Appl. Phys. Lett.* **91**, 181501.

Kotsonis, M. & Ghaemi, S. 2011 Forcing mechanisms of dielectric barrier discharge plasma actuators at carrier frequency of 625 Hz. *J. Appl. Phys.* **110**, 113301.

Kotsonis, M., Ghaemi, S., Veldhuis, L. & Scarano, F. 2011 Measurement of the body force field of plasma actuators. *J. Phys. D: Appl. Phys.* **44**, 045204.

Kriegseis, J., Schwarz, C., Tropea, C. & Grundmann, S. 2013 Velocity-information-based force-term estimation of dielectric-barrier discharge plasma actuators. *J. Phys. D: Appl. Phys.* **46**, 055202.

Leonov, S., Opaits, D., Miles, R. B. & Soloviev, V. R. 2010 Time-resolved measurements of plasma-induced momentum in air and nitrogen under dielectric barrier discharge actuation. *Phys. Plasmas* **17**, 113505.

Likhanskii, A. V., Shneider, M. N., Macheret, S. O. & Miles, R. B. 2008 Modeling of dielectric barrier discharge plasma actuator in air. *J. Appl. Phys.* **103**, 053305.

Moreau, E. 2007 Airflow control by non-thermal plasma actuators. *J. Phys. D: Appl. Phys.* **40**, 605–636.

Moreau, E., Sosa, R. & Artana, G. 2008 Electric wind produced by surface plasma actuators: a new dielectric barrier discharge based on a three-electrode geometry. *J. Phys. D: Appl. Phys.* **41**, 115204.

Munday, P. M. & Taira, K. 2013 On the lock-on of vortex shedding to oscillatory actuation around a circular cylinder. *Phys. Fluids* **25**, 013601.

Neumann, M., Friedrich, C., Czarske, J., Kriegseis, J. & Grundmann, S. 2012 Determination of the phase-resolved body force produced by a dielectric barrier discharge plasma actuator. *J. Phys. D: Appl. Phys.* **46**, 042001.

Nishida, H., Nonomura, T. & Abe, T. 2012 Numerical Analysis on Three-dimensional Body Force Field of DBD Plasma Actuator. In *43rd AIAA Plasmadynamics and Lasers Conference*. New Orleans, Louisiana: American Institute of Aeronautics and Astronautics.

Orlov, D. M., Font, G. I. & Edelstein, D. 2008 Characterization of Discharge Modes of Plasma Actuators. *AIAA J.* **46**, 3142–3148.

Post, M. L. & Corke, T. C. 2004 Separation Control on High Angle of Attack Airfoil Using Plasma Actuators. *AIAA J.* **42**, 2177–2184.

Roth, J. R. 2007 Physics and phenomenology of plasma actuators for control of aeronautical flows. *J. Phys. D: Appl. Phys.* **40**.

Roth, J. R., Sherman, D. M. & Wilkinson, S. P. 2000 Electrohydrodynamic Flow Control with a Glow-Discharge Surface Plasma. *AIAA J.* **38**, 1166–1172.

Soloviev, V. R. 2011 Analytical estimation of the thrust generated by a surface dielectric barrier discharge. *J. Phys. D: Appl. Phys.* **45**, 025205.

Thomas, F. O., Corke, T. C., Iqbal, M., Kozlov, A. & Schatzman, D. 2009 Optimization of Dielectric Barrier Discharge Plasma Actuators for Active Aerodynamic Flow Control. *AIAA J.* **47**, 2169–2178.

2

Paper 2

A turbulent boundary layer with pressure gradient, curvature and separation – results from hot-wire measurements

By Julie A. Vernet, Ramis Örlü, P. Henrik Alfredsson

Linné Flow Centre, KTH Mechanics, SE-100 44 Stockholm, Sweden

Technical Report

Most flows of relevance in technical applications are exposed to the combined effect of surface curvature and pressure gradient. The applicability of knowledge from canonical wall-bounded flows is hence limited when it comes to these complex flows and geometries. The present investigation is an attempt to contribute to this topic by experimentally investigating the turbulent boundary layer developing upstream, over, and downstream a wall-mounted cylinder section. Hot-wire anemometry is used and although such measurements are impaired in the separated region, we show here how to exploit the readings to get information on the separated region. Single-point streamwise velocity statistics and spectra are presented and discussed with focus on the effect of back flow (separation) on the statistics and the emergence of an internal boundary layer.

1. Introduction

The quest for more fuel-efficient ground vehicles such as trucks and trains as well as airplanes and ships, is directly coupled to reducing the form and/or friction drag without compromising the other. A prototype of a canonical flow on which our understanding of friction drag has been developed is the zero-pressure gradient boundary layer for which drag can be reduced if the laminar boundary layer region can be extended to high Reynolds numbers, before transition to turbulence occurs. When the boundary layer has become turbulent there is little to do in order to reduce drag, except keeping the surface as smooth as possible or maybe to employ miniature streamwise oriented riblets in form of plastic sheets to the surface (Garcia-Mayoral & Jimenez 2011). Most flows of relevance in technical applications are however exposed to surface curvature and related pressure gradients, that lead to other phenomena and new challenges when it comes to the design of low-drag bodies. For such cases form drag or pressure drag may be the main contributor to the overall drag and it is especially significant for bodies which experience large regions of separated flows. As a comparison between the different vehicles the form drag of cars and

trucks is typically 80-90% of the total aerodynamic drag, whereas for commercial aircraft it is 30–40% and for large ships may amount to only 10-20% of the total drag during 'cruise' conditions.

The applicability of knowledge from canonical wall-bounded flows is hence limited when it comes to these complex flows and geometries (Patel & Sotiropoulos 1997). While the effect of pressure gradient and surface curvature have been the focus of much attention, their combined effect is not a simple superposition and therefore deserves special attention (Webster *et al.* 1996; Cavar & Meyer 2011).

In an attempt to make a general contribution to this field, the turbulent boundary layer developing upstream, over, and downstream a wall-mounted cylinder section is here studied experimentally. The aim of the present study is to provide mean and turbulence statistics including higher order moments and spectra obtained through single-component hot-wire anemometry for two Reynolds numbers. The streamwise evolution of the turbulence statistics and spectra in the vicinity of the bump, where separation occurs, is mapped in detail and a special focus has been laid on the interpretation of the hot-wire results which are impaired due to back flow. Methods to discern the boundary layer edge as well as the region of back flow have been proposed and successfully applied on the available data. Additionally, the data will also provide well-documented inflow and reference data for a companion numerical study in which the same flow case is studied by means of Large Eddy Simulations Futrzynski & Efraimsson (2014). The work is performed within the FRANCE (Flow Research on Advanced and Novel Control Efficiency) project, which aims to investigate possible methods to control the flow around the front of a truck in order to reduce form drag due to separation at the A-pillar. Hence, the present work can be seen as providing detailed statistics for a generic geometry that shares the main flow features with the flow around an A-pillar. A feasibility study of the control is presented in Vernet *et al.* (2014) and will not be discussed in the present work.

The paper is organised as follows: Section 2 presents the experimental setup and employed measurement techniques, section 3 presents and discusses the results consisting of inflow conditions, separation detection and of the mean flow and turbulence statistics. The paper is finally summarised and concluded in section 4. An appendix also discusses the effect of a rectified hot-wire signal on the spectral behaviour.

2. Experimental Setup

The experimental setup was designed in such a way that a turbulent boundary layer developing on a flat plate approaches an obstacle mounted on the plate surface, accelerates over it and separates at the downstream side of the obstacle and thereafter reattaches on the flat plate. In the control part of the project the cylinder is equipped with Dielectric Barrier Discharge (DBD) plasma actuators

producing an electric wind in form of a wall jet to control and reduce the separated region. The setup was realised through a 1.50 m long flat plate with an elliptical leading edge and flap at the trailing edge. The plate was mounted horizontally and placed at a height of 0.20 m from the floor of the test-section (0.5 m (height) $\times$ 0.4 m (width) cross-sectional area) in the NT2011, open-loop wind tunnel in the Fluid Physics Laboratory, KTH Mechanics. A cylinder with a diameter (L) of 0.1 m is mounted 0.5 m downstream the leading edge of the flat plate such that a 2D bump (with height $h = L/2$) protrudes out of the plate as schematically shown in figure 1*a)*. In order to establish a two-dimensional flow over the cylinder it is equipped with end-plates to avoid interference with the boundary layers that develop on the test-section walls. The initially laminar boundary layer developing on the test plate is tripped with *DYMO* tapes embossed with the letter "V", where the apex is pointing in the flow direction, to fix the transition location.

The plate, including the cylinder, is equipped with pressure taps along the streamwise direction, which are connected through plastic tubings to a 48 channel, mechanical Scanivalve. The pressures from the Scanivalve were read by a high accuracy *MKS 120A Baratron* pressure transducer (full scale 10 Torr). Streamwise velocity measurements were performed by means of a single hot-wire probe with a special design adapted to the current geometrical constraints, depicted in figure 1*b)* which enabled measurements close to the cylinder. To allow traversing in the vertical direction, the hot-wire probe was mounted at the bottom of a sting attached to a traversing system that was fixed on the roof of the test-section. Traversing was performed using a lead screw traverse driven by

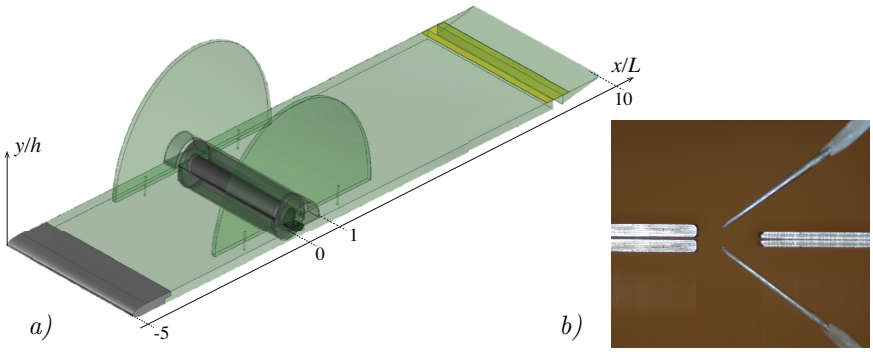

FIGURE 1. *a)* Schematic of used setup, where the flow direction is aligned with the $x-$axis, *i.e.* from left to right. *b)* Photograph of in-house built hot-wire as well as an illustration of the "mirrored image technique" (Örlü *et al.* 2010) employed to determine the wall position using two gauge heights of 0.5 and 1 mm thickness.

a stepper motor yielding a minimum step size of around 2 microns.The hot wire itself is a stubless Platinum wire of $\ell = 300$ micron length and nominal diameter of 1.3 micron that is soldered to the conical prongs (facing the flat plate) with a nominal tip diameter of around 50 micron. The calibration was performed *in situ* in the free stream at the inlet of the test section against a Pitot-static tube connected to a micromanometer of type *Furness Controls Limited FC012* (full scale 2 kPa). The hot-wire anemometer system used is a *Dantec StreamLine* 90N10 frame in conjunction with a 90C10 constant temperature anemometer module operated at a resistance overheat of 80%. In order to avoid aliasing an inbuilt analog low-pass filter was set up with 30 kHz cut-off frequency prior to the data acquisition (sampled at 60 kHz with a 16-bit A/D converter).

3. Results and Discussion

The experiments have been performed at two velocities at the test-section inlet, *viz.* $U_0 = 8$ and 16 m/s. Measurements of the pressure distribution along the plate as well as the vertical distribution of the streamwise velocity have been made at several locations upstream, on and downstream the cylinder. In the following, first the turbulent boundary layer constituting the inflow is described (section 3.1), upon which the method to detect measurement points in the separation region is outlined (section 3.2), before the mean flow development (section 3.3) and turbulence statistics are presented (section 3.4).

3.1. *Inflow conditions*

Since the experiments will also provide reference data for ongoing simulations of the same geometry, but also in order to ensure that the cylinder is approached by a well-developed turbulent boundary layer, special attention has been given to provide detailed inflow details. As apparent from figure 2, the turbulent boundary layer adheres to well established wall-turbulence scaling relations, *i.e.* the linear and logarithmic velocity profiles (albeit in its infancy, due to the low Reynolds number) are present in the mean streamwise velocity (U) profiles. Similarly, the root-mean-square (rms) profile of the streamwise velocity component (u') exhibits a peak at around $y^+ = 15$. Here and henceforth, the superscript + indicates scaling with wall units, *i.e.* the friction velocity (u_τ) and the viscous length scale (ℓ_*). Since the skin friction has not been measured directly, the friction velocity was determined from a Clauser chart (Clauser 1956) using constants of 0.41 and 5.2 and the deduced value was checked against common indicators following Örlü *et al.* (2010).

For a better understanding of the inlet profile, the experimental data were compared with results from a Direct Numerical Simulations (DNS) of a zero-pressure gradient (ZPG) turbulent boundary layer at matched momentum-loss thickness Reynolds numbers, Re_θ, *viz.* the data by Komminaho & Skote (2002) and Schlatter & Örlü (2010) for the low and higher Re_θ cases, respectively. Table 1 summarizes the parameters of the two physical and two numerical

experiments. As apparent from the comparison with the DNS data, shown as solid lines in figure 2, the measured mean streamwise velocity profiles agree with the DNS throughout the inner layer. There are, however, discrepancies in the wake region. Despite a matched Re_θ, the friction Reynolds numbers differ and indicate that the wake regions have evolved differently. It should be noted that both DNS data sets behave as canonical TBLs as evident from their agreement with the skin friction relation by Smits *et al.* (1983) or other integral and global parameters as shown in Schlatter & Örlü (2010, 2012). One explanation for the different behaviour in the experimental data might be related to the short development length downstream the tripping device as well as different upstream histories, *i.e.* the possible presence of a weak favourable pressure gradient (FPG). The latter is, in particular, apparent from the fact that the experimental profile has a lower wake strength. The suspicion of a mild FPG can also be inferred from the rms profiles. Here, the rms values in the near-wall region appear attenuated compared to the DNS data. One reason for this could have been insufficient spatial resolution (Örlü & Alfredsson 2010), but as apparent from the relatively short length of the hot wire (*cf.* Table 1) and

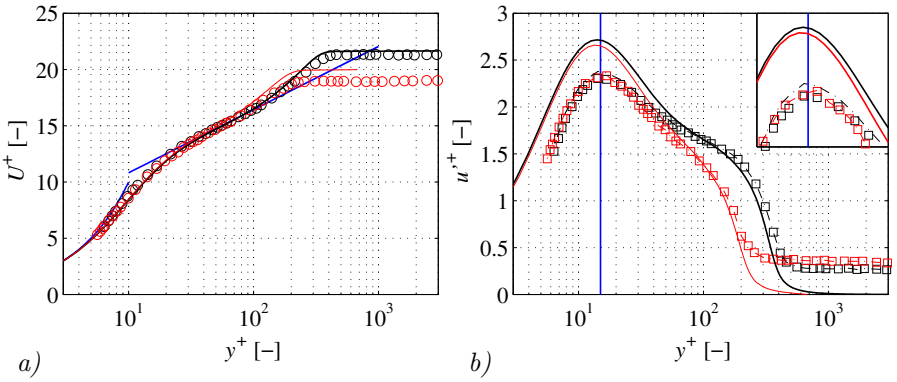

FIGURE 2. *a)* Inner-scaled mean and *b)* rms profiles of the streamwise velocity component for the profiles at the most upstream position, *i.e.* $x/L = -2.5$. Hot-wire measurements for $U_0 = 8$ (○, □) and 16 m/s (○, □) are given as symbols, while solid lines represent the DNS, *i.e.* Komminaho & Skote (2002) (red) and Schlatter & Örlü (2010) (black) for the low and higher Re cases, respectively. Blue solid lines represent the linear and logarithmic ($\kappa = 0.41$ and $B = 5.2$) velocity profile in *a)*, while it indicates the presumed location of the inner-peak in the rms in *b)*. The dashed lines in *b)* represents the rms corrected for spatial resolution effects (following the scheme by Smits *et al.* 2011).

	U_0 $[\frac{m}{s}]$	u_τ $[\frac{m}{s}]$	Δz^+	Re_θ	Re_τ	$Re_h \cdot 10^3$
present study (red)	8	0.42	8	490	245	25
DNS (red)	–	–	–	490	210	–
present study (black)	16	0.76	14	970	420	50
DNS (black)	–	–	5	940	360	–

TABLE 1. Parameters for hot-wire experiments and DNS (Komminaho & Skote 2002; Schlatter & Örlü 2010). Besides, the free-stream velocity at the test-section inlet (U_0), deduced friction velocity (u_τ) and spanwise resolution (*i.e.* viscous-scaled hot-wire length ℓ^+ and grid resolution), also the various Reynolds numbers are given, *viz.* based on the momentum-loss thickness Re_θ, the friction Reynolds number Re_τ and the one based on outer scales Re_h.

the rms values corrected for spatial resolution effects (utilising the correction scheme by Smits *et al.* 2011), it is very unlikely that this can explain the attenuated rms values. Consequently, the observed differences in the mean and rms profile could probably be related to mild FPG conditions (*cf.* Nickels 2004).

3.2. *Separation detection*

Since a single hot-wire probe is insensitive to the direction of the flow it will give erroneous measurements of the mean and the rms (or any other quantity for that matter) of the velocity in the low velocity region close to the wall where reverse flow occurs. While several workarounds are known for laminar separated flows to infer the separated region from hot-wire data (see *e.g.* Häggmark *et al.* 2000), these are less applicable in turbulent separated flows, where "flying hot-wires" (Watmuff *et al.* 1983) or "pulsed wires" (Bradbury & Castro 1971) are more suitable (but seldom employed). In order to discern the region in which the hot-wire measurements can be trusted several quantities, compared in figure 3, have been inspected. As apparent from the probability density function (pdf) map, the instantaneous velocity does not reach zero velocity, due to wall interference and buoyancy effects, besides the aforementioned directional insensitivity. Due to signal rectification, the measured velocity distribution is more skewed towards the positive side than the actual velocity distribution and reaches values that are otherwise only found in the viscous sublayer or at the boundary layer edge for canonical wall-bounded flow (*i.e.* $S_u > 1$). In accordance with previous observations, the extremal points of the rms (maximum), skewness (zero-crossing) and flatness (minimum) coincide (Eitel-Amor

et al. 2014). Contrary to canonical wall turbulence profiles, which exhibit this behaviour at around $y^+ = 15$ (relating it to the near-wall cycle and the peak of turbulence production), here it is related to the inflection point in the measured mean velocity profile as apparent from the 1st and 2nd derivative shown in figure 3*c)*. This diagnostic tool, will here be utilised to discern measurement points that are within the separated region.

3.3. *Mean flow development*

The surface static pressure coefficient is defined as

$$C_p = \frac{p_i - p_1}{\frac{1}{2}\rho U_0^2},$$

where p_1 is the pressure measured by the most upstream pressure tap (at $x/L = -3.2$) on the plate and U_0 the velocity measured by the Pitot-static probe at the inlet of the test section. The streamwise C_p distribution shown in figure 4, indicates that the turbulent boundary layer is first exposed to a nearly zero pressure gradient (up to approximately $x/L = -2.5$) and is thereafter successively exposed to an adverse pressure gradient up to the start of the cylinder and then favourable pressure gradient over the first quarter of the exposed cylinder surface.

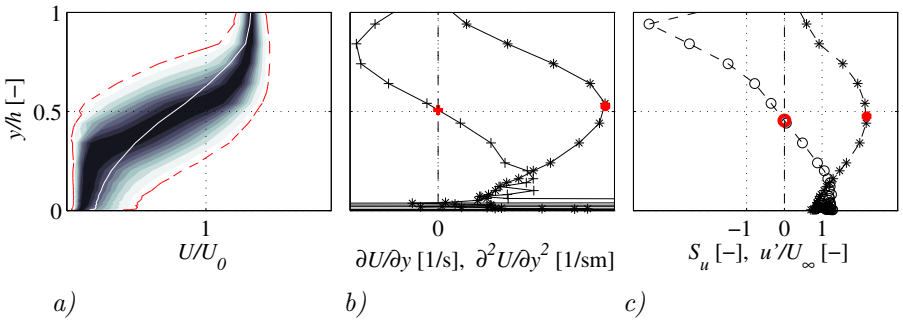

FIGURE 3. *a)* Contour map of the measured velocity pdf for the profile at $x/L = 2$ (thus including a flow separated region) and $U_0 = 16$ m/s. The pdf is normalized by its maximum value at each y-position and the red dashed lines represent the contour at 1% of the maximal value. The white solid line depicts the mean value. *b)* First ($*$) and second ($+$) derivative of the measured mean streamwise velocity along the y direction. Red symbols are maximum of first derivative and zero-crossing of second derivative. *c)* Skewness ($\circ$) and rms ($*$) of the streamwise velocity. The red symbols are the maximum value of the rms and the zero crossing of the skewness.

The mean velocity profiles at several positions upstream, on and downstream the cylinder at both U_0=8 and 16 m/s are shown in figure 5. The measurement positions are at $x/L = -2.5$, -1.3, -0.19, 0.5, 0.8, 2.0, 3.5, 5.0 and 6.8. In the figure the positions where the flow was determined to have instantaneous back flow (although it is not fully separated) are marked in red. These positions were determined from the different criteria discussed previously, *viz.* the inflection point in the measured average velocity, the maximum in the rms and the zero-crossing of the skewness. These criteria often gave the same position for the occurrence of back flow, and in a few cases where they did not coincide the criterion that gave the largest distance from the wall was used instead. As can be seen from figure 5 for both velocities there is a back-flow region in front of the cylinder as expected, the flow reattaches on the front part of the cylinder and separation occurs again beyond the 90 degree point of the cylinder. Downstream the cylinder there is again reattachment on the flat plate but there is a distinct difference for the two different free-stream velocities, with the higher velocity having a significantly smaller separated region and earlier reattachment. Although differences in effective blockage can have effect on the separation, we found that such differences in effective blockage are small, since the velocity at $y/h = 3$, when normalised with the inlet velocity, *i.e.* U_0, did not differ with more than 1 % for the two cases upstream and on top of the cylinder. Differences up to 5 % are, on the other hand, present downstream the cylinder, *i.e.* for $x/L > 1$, and it is hypothesised that these differences are mainly due to the difference in Reynolds number; as expected the recovery

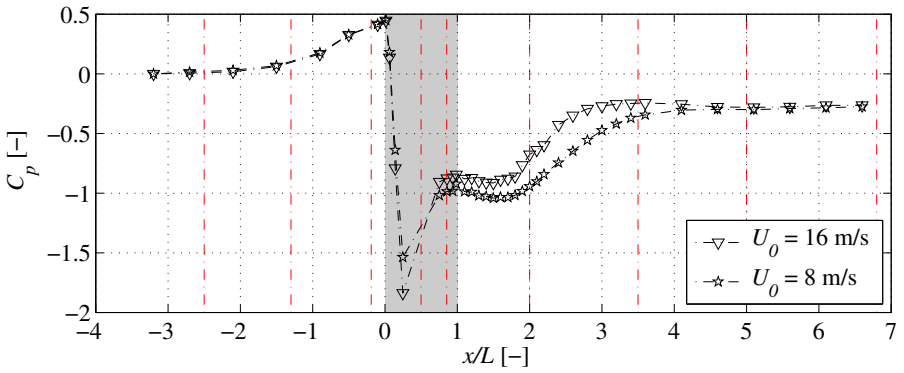

FIGURE 4. Streamwise evolution of the pressure coefficient C_p profile for $U_0 = 8$ and 16 m/s. Grey area represents the position of the bump and the vertical dashed lines the position where streamwise velocity profiles were measured via hot-wire anemometry.

after separation would be faster at a higher Reynolds number, which become also clear in the next paragraph.

When it comes to the shape of the mean velocity profiles, the profile and therefore its shape factor (H_{12}) changes from a turbulent one at $x/L = -2.5$ and -1.3 (with $H_{12} = 1.55$ and 1.50, respectively) to a separated one (with H_{12} values beyond the laminar value) when approaching the concave intersection and re-attains the shape and shape factor of a turbulent boundary layer for the two most downstream stations. As pointed out by Spalart & Watmuff (1993), the classical definitions of the boundary layer thicknesses obtained through

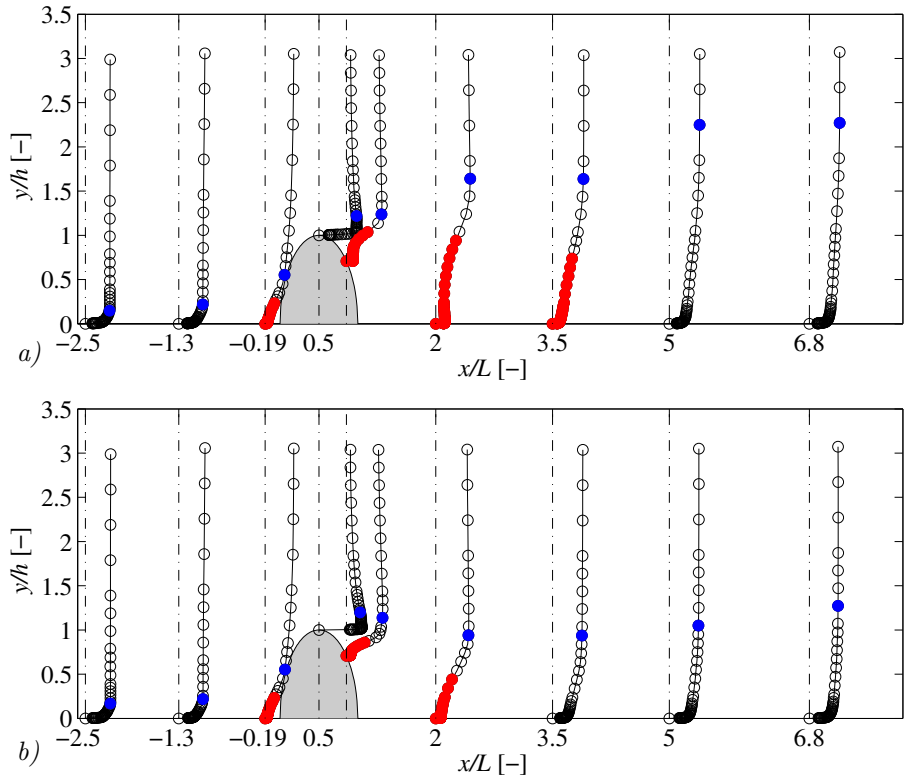

FIGURE 5. Overview of the streamwise evolution of the measured velocity at *a)* $U_0 = 8$ m/s and *b)* $U_0 = 16$ m/s. Filled red measurement points indicate positions detected to have back flow, while those in blue mark the boundary layer edge. The circular cylinder is marked as the grey body, which here is deformed since the x-axis is in the same scale as the y-axis.

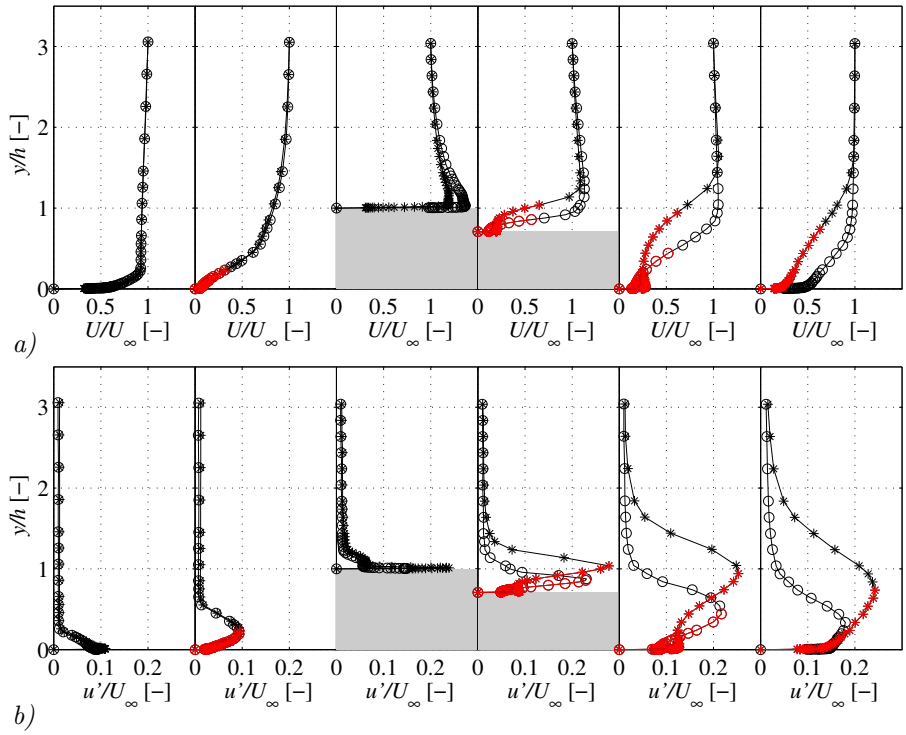

FIGURE 6. Direct comparison of the *a)* mean velocity and *b)* rms profiles for the two velocities $U_0 = 8$ m/s ($*$) and 16 m/s ($\circ$) at x/L =-1.3, -0.19, 0.5, 0.80, 2.0 and 3.5. Both types of profiles are normalised by the mean velocity at y/h=3.

integration of the boundary layer profile with $y \to \infty$ are not applicable here, and truncated integrals are therefore necessary in order to obtain meaningful values for the shape factor or even boundary layer thickness. While Spalart & Watmuff (1993) utilised the Reynolds shear stress and streamwise vorticity as remedies, here — due to the inaccessibility of these quantities — the edge of the boundary layer was determined based on the skewness and flatness values which attain extrema at the turbulent/non-turbulent interface. Similar to the detections of measurement points that exhibit back flow both criteria yielded nearly the same position, and only in a few exceptional cases where they did not coincide the criterion that gave the largest distance from the wall was used instead.

3.4. *Turbulence statistics*

In figure 6 the mean and rms profiles for six different x/L positions (-1.3, -0.19, 0.5, 0.80, 2.0 and 3.5) are directly compared for the two Reynolds number

cases. The two cases are nearly identical upstream the cylinder (as also confirmed from their shape factors), but differ slightly at the 90 degree position; a difference that is further pronounced on the downstream side of the cylinder. The agreement upstream the cylinder in both mean and rms values in outer scaling — despite doubling of the Reynolds number — indicates that the boundary layer can be considered both fully developed and free of changed boundary conditions (*e.g.* blockage effects). The influence of the surface curvature and the induced pressure gradient is apparent from the peak location of the rms of the streamwise velocity component: while the peak location is related to the turbulence production for the most upstream station, the peak location is further away from the wall and coincides with the location of the inflection point (this effect is enhanced due to the directional insensitivity of the hot wire) as apparent from the color-marked (back flow) measurement points.

For a more detailed comparison of the profiles on the top of the cylinder, figure 7 shows an expanded view close to the cylinder surface, together with the associated skewness and flatness factors. As pointed out by Baskaran *et al.* (1987), the flatness factor gives further evidence for the existence of an internal boundary layer: while the edge of the boundary layer can be discerned from a positive extremum of the flatness factor (and negative extremum of the skewness factor for that matter), the flatness factor exhibits an additional inner extremal value (again associated with a minimum in the skewness factor) at the edge of the internal boundary layer. As apparent, the internal boundary layer is thinner for the $U_0 = 16$ m/s case and also the velocity excess is larger; which will be discussed in the following. It is also interesting to note that the thickness of the internal boundary layer is around the height of the momentum loss thickness (θ) of the external boundary layer in accordance with observations by Webster *et al.* (1996) and Wu & Squires (1998), where the thickness of the internal layer was obtained from the location of the so called knee points of the turbulent stresses.

To further illuminate the effect of surface curvature on the turbulence, figure 8 shows the spectral maps for the same x-positions as in figure 6. The abscissa shows the frequency in outer scaling, *i.e.* multiplied by an outer time scale based on the boundary layer thickness (δ) and velocity at the edge of the boundary layer, which corresponds to the Strouhal number, while the ordinate is the outer-scaled y-position (here scaled by h instead of δ in order to ease comparison with figure 6). The figure is compiled from the spectra measured at all y-positions and for each x-position the map is normalised with the highest spectral value at that x-position. Data below the dashed red line correspond to positions where back flow occurs. In these cases it is interesting to note that the dashed line corresponds to the y-position with the widest spectral content, below that position the width of the spectral map decreases. The effect of back flow on spectra obtained from hot-wire measurements is further discussed in the appendix. For the two cases measured on the cylinder the figure also shows

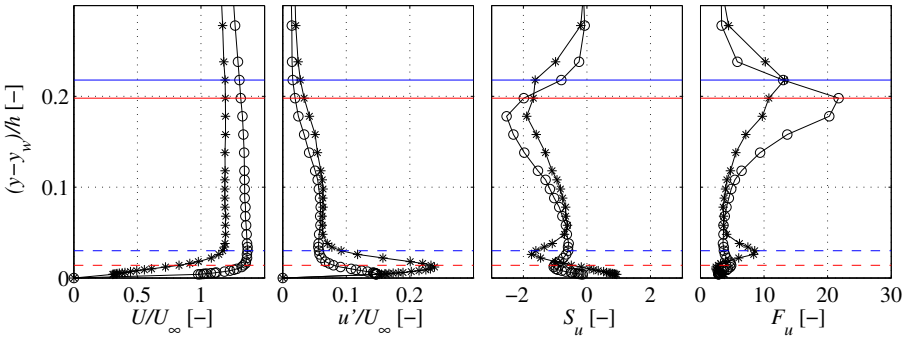

FIGURE 7. Close up of the mean and rms profiles on the top of the cylinder together with the related profiles of the skewness and flatness factors. $*$: $U_0 = 8$ m/s (—); $\circ$: $U_0 = 16$ m/s (—). Solid and dashed lines indicate the external and internal boundary edge, respectively.

an expanded view of the space above the grey marked area so that it is possible to see the distribution of the spectral content in some detail. A clear difference between the attached boundary layers upstream and downstream the cylinder is the shift of the energy maximum from near the wall towards the outer part of the boundary layer as can also be observed in figure 6. From the spectra we can furthermore see that the energy content is shifted towards lower frequencies having its minimum on top of the cylinder, probably reflected by energetic large-scale motions created in the separated region and that the boundary layer thickness downstream the cylinder has increased. At the same time, the spectral peak being located close to $y^+ = 15$ (*i.e.* $y/h < 0.01$) upstream the cylinder ($x/L \leq -1.3$), first gets pushed away from the wall due to the separated region ($x/L = 0.19$), but it is then again submerged in the internal boundary layer while on top of the cylinder ($x/L = 0.5$), before it is entirely dislocated from the near-wall cycle or the internal boundary layer and location at the edge of the external boundary layer (*i.e.* $y/\delta = \mathcal{O}(1)$) for $x/L \geq 0.8$. Once the boundary layer is re-attached (*cf.* the U_0 =16 m/s case for $x/L = 3.5$), the spectral energy content protrudes into the inner layer of the boundary layer but is far from being recovered from its upstream history; this can further be confirmed from the turbulence statistics and spectra at $x/L = 6.8$ (not shown here).

4. Summary and Conclusion

A turbulent boundary layer developing upstream, over and downstream a cylindrical 2D bump has been realised experimentally and assessed by means of hot-wire measurements. Hot-wire anemometry, albeit limited in its applicability in

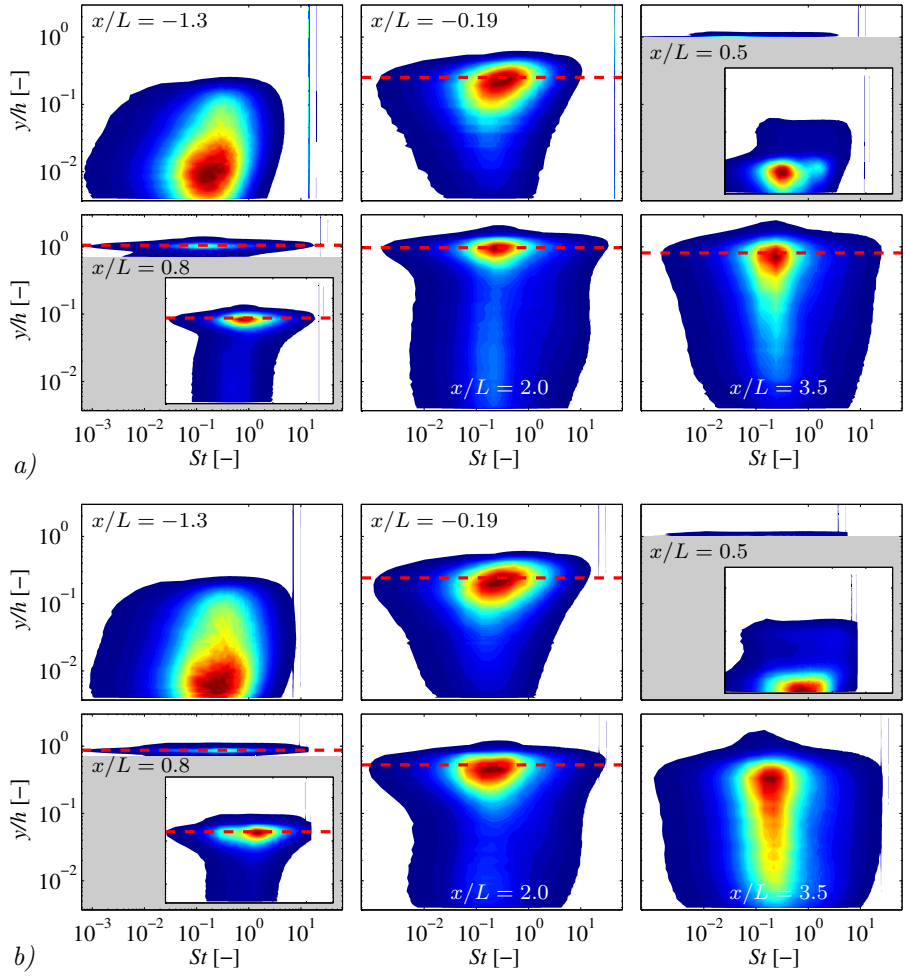

FIGURE 8. (Pre-multiplied) Spectral maps of the velocity at *a)* $U_0 = 8$ m/s and *b)* $U_0 = 16$ m/s for the same x-positions as in figure 6. The Strouhal number is based on the thickness and velocity of the boundary layer edge as indicated in figure 5. Data below the dashed red line correspond to positions where the occurrence of back flow is expected.

separated flows, has here nonetheless been utilized to provide one-point statistics and spectral information of the streawise velocity component in regions without back flow. To cope with the separated flow region, various criteria to discern back flow in turbulent flows have been assessed and a coherent view on detection criteria has been provided. In particular, it turned out that the

extrema of the measured mean velocity profile (maxima of 1^{st} and zero-crossing of the 2^{nd} derivative) coincide with the zero-crossing of the skewness factor and maximum of the flatness factor, while the latter two quantities could be explained through the behaviour of the bounding contour of the pdf. Application of these criteria provided a clear demarcation of the separated region.

Skewness and flatness factors were furthermore exploited — in the absence of multi-point measurements — to discern the edge of the boundary layer. Analysis of the mean and turbulence statistics revealed evidence for an internal boundary layer that develops on the cylinder where the flow is attached. In agreement with previous studies, the internal layer exhibits its own near-wall dynamics irrespective of the external boundary layer.

The present experiments also provide reference data for ongoing flow control study aiming at delaying the separation of a turbulent boundary layer over a cylinder section by means of plasma actuation. Furthermore, the results will serve as a validation for large-eddy simulations that are performed within the FRANCE project.

Acknowledgments

FRANCE project leader is Prof. Gunilla Efraimsson, KTH (also task leader for the numerical part of the project). The project is carried out in collaboration with Scania CV AB (Dr. Per Elofsson) and is partially financed by the Swedish Energy Agency.

Appendix

In the following, an experiment was made in order to understand how the spectra are affected by the rectifying effect of the hot wire. For this purpose, a hot-wire signal without back-flow was utilised and two synthetic signals were generated, one where the "correct" velocity (*i.e.* with back flow) could be measured and one where the back-flow readings are rectified. These two signals are depicted in figure 9 together with their pre-multiplied spectra. Because the signal is rectified the mean value increases and hence the rms level decreases. This can be clearly seen from the premultiplied spectra where the area below the spectra for the synthetic signal is much smaller than for the original signal. The high-frequency end is however not affected by the rectifying process. A similar observation can be seen in the spectra shown in figure 8, however since the spectra in that figure is normalised with highest spectral energy level these spectral maps are affected both at the high and low frequency ends.

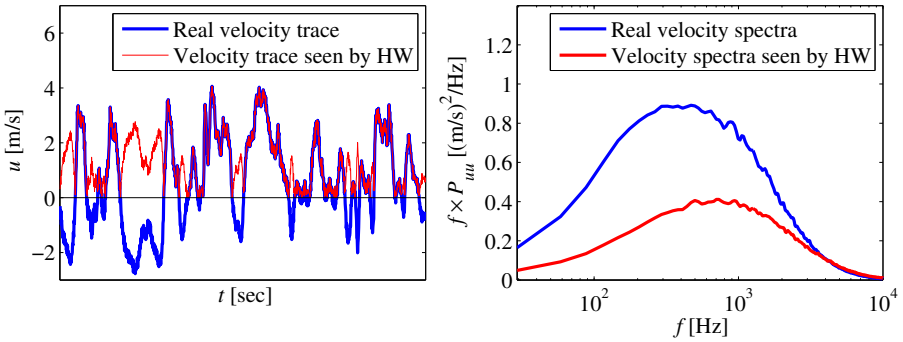

FIGURE 9. *Left*: A velocity trace (blue) and a corresponding synthetic velocity trace (red) for which all velocity readings below 0 m/s have been rectified. *Right*: Calculated spectra for the two signals shown in premultiplied form.

References

Baskaran, V., Smits, A. J. & Joubert, P. N. 1987 A turbulent flow over a curved hill. Part 1. Growth of an internal boundary layer. *J. Fluid Mech.* **182**, 47–83.

Bradbury, L. J. S. & Castro, I. P. 1971 A pulsed-wire technique for velocity measurements in highly turbulent flows. *J. Fluid Mech.* **49**, 657–691.

Cavar, D. & Meyer, K. E. 2011 Investigation of turbulent boundary layer flow over 2D bump using highly resolved large eddy simulation. *J. Fluids Eng.* **133**, 111204.

Clauser, F. H. 1956 The turbulent boundary layer. In *Advances in applied mechanics* (ed. H. L. Dryden & T. von Kármán), pp. 1–51. Academics Press Inc.

Eitel-Amor, G., Örlü, R. & Schlatter, P. 2014 Simulation and validation of a spatially evolving turbulent boundary layer up to Re_θ=8300. *Int. J. Heat Fluid Fl.* **47**, 57–69.

Futrzynski, R. & Efraimsson, G. 2014 Effect of a SDBD on the drag of a half-submergedd cylinder in crossflow. In *ASME 2014 4th Joint US-European Fluids Engineering Division Summer Meering and the 11th International Conference on Nanochannels, Mircrochannels and Minichannels FEDSM 2014*, pp. 1–10. Chicago, Illinois, USA.

Garcia-Mayoral, R. & Jimenez, J. 2011 Drag reduction by riblets. *Philos. T. Roy. Soc. A* **369**, 1412–1427.

Häggmark, C. P., Bakchinov, A. A. & Alfredsson, P. H. 2000 Measurements with a flow direction boundary-layer probe in a two-dimensional laminar separation bubble. *Exp. Fluids* **28**, 236–242.

Komminaho, J. & Skote, M. 2002 Reynolds stress budgets in couette and boundary layer flows. *Flow Turbul. Combust.* **68**, 167–192.

Nickels, T. B. 2004 Inner scaling for wall-bounded flows subject to large pressure gradients. *J. Fluid Mech.* **521**, 217–239.

Örlü, R. & Alfredsson, P. H. 2010 On spatial resolution issues related to time-averaged quantities using hot-wire anemometry. *Exp. Fluids* **49**, 101–110.

Örlü, R., Fransson, J. H. M. & Alfredsson, P. H. 2010 On near wall measurements of wall bounded flows – The necessity of an accurate determination of the wall position. *Prog. Aerosp. Sci.* **46**, 353–387.

Patel, V. C. & Sotiropoulos, F. 1997 Longitudinal curvature effets in turbulent boundary layers. *Prog. Aerosp. Sci.* **33**, 1–70.

Schlatter, P. & Örlü, R. 2010 Assessment of direct numerical simulation data of turbulent boundary layers. *J. Fluid Mech.* **659**, 116–126.

Schlatter, P. & Örlü, R. 2012 Turbulent boundary layers at moderate Reynolds numbers: inflow length and tripping effects. *J. Fluid Mech.* **710**, 5–34.

Smits, A. J., Matheson, N. & Joubert, P. N. 1983 Low-Reynold-number turbulent boundary layers in zero and favorable pressure gradients. *J. Ship Res.* **27**, 147–157.

Smits, A. J., Monty, J., Hultmark, M., Bailey, S. C. C., Hutchins, N. & Marusic, I. 2011 Spatial resolution correction for wall-bounded turbulence measurements. *J. Fluid Mech.* **676**, 41–53.

Spalart, P. R. & Watmuff, J. H. 1993 Experimental and numerical study of a turbulent boundary layer with pressure gradients. *J. Fluid Mech.* **249**, 337–371.

Vernet, J., Örlü, R. & Alfredsson, P. H. 2014 Flow separation delay on trucks A-pillars by means of Dielectric Barrier Discharge plasma actuation. *Submitted* .

Watmuff, J. H., Perry, A. E. & Chong, M. S. 1983 A flying hot-wire system. *Exp. Fluids* **1**, 63–71.

Webster, D. R., DeGraaff, D. B. & Eaton, J. K. 1996 Turbulence characteristics of a boundary layer over a two-dimensional bump. *J. Fluid Mech.* **320**, 53–69.

Wu, X. & Squires, K. D. 1998 Numerical investigation of the turbulent boundary layer over a bump. *J. Fluid Mech.* **362**, 229–271.

Paper 3

3

Flow separation delay on trucks A-pillars by means of Dielectric Barrier Discharge plasma actuation

By Julie A. Vernet, Ramis Örlü, P. Henrik Alfredsson

Linné Flow Centre, KTH Mechanics, SE-100 44 Stockholm, Sweden

Submitted

The flow around a half cylinder (*i.e.* an immersed cylinder in a flat plate) approached by a turbulent boundary layer is studied, with the aim to control separation via steady Dielectric Barrier Discharge (DBD) plasma actuation. The geometry is chosen as a generic model of the flow around the front corners (A-pillars) of a truck cabin and the work is performed with the long-term vision to be able to reduce drag on trucks. The electric wind induced by a single DBD plasma actuator is studied in quiescent air to understand the role of the different driving parameters and how the cylindrical shape influences the downstream development of the induced electric wind. A double DBD plasma actuator is placed on the cylinder and the influence of the position of the actuator is studied in order to find the best achievable control. Comparison of the controlled and uncontrolled cases, using both hot-wire anemometry as well as pressure measurements, show that a reduction of the separation bubble is possible. By optimising the position of the double actuator, a reduction of up to 30% of the drag is achieved.

1. Introduction

When considering a 40 ton truck-trailer combination driving at 80 km/h on a level road, the aerodynamic drag counts for more than 20% of the total energy loss of the vehicle and 70% of this drag is induced by the tractor when considering a zero degree yaw angle[1]. One of the contributions to the aerodynamic drag comes from the flow separation from the truck's surface while passing the A-pillars (front corners) of the tractor. Since the 80's, solutions to decrease the drag of the tractor, such as rounded corners, have been extensively investigated and developed. It has been shown that rounded corners with a radius of about 0.3 m are optimal to delay this separation (Barnard 2009). However this

[1]Personal communication with Dr. Per Elofsson, Senior Technical Manager, Aerodynamics, Scania CV AB

value is only appropriate for a zero degree yaw angle. Active control methods with potential feedback control loop can improve the separation delay when considering that trucks on the road are subjected to varying yaw angles. The present project focuses on the study of Dielectric Barrier Discharge (DBD) plasma actuators with the objective of using the induced electric wind to investigate if turbulent boundary layer separation occurring on the A-pillars can be controlled with such devices.

Research on plasma actuators for flow control started about 20 years ago (Roth *et al.* 1998) when the so called electric wind was identified as a possible candidate able to produce a wall jet with a substantial streamwise momentum that could be used for flow control purposes. Flow control fields to which DBD plasma actuators are applied to and show promising results are nowadays numerous including noise control (Thomas *et al.* 2008; Inasawa *et al.* 2013), skin-friction drag reduction both controlling laminar (Grundmann *et al.* 2007; Hanson *et al.* 2010; Duchmann *et al.* 2013; Osmokrovic *et al.* 2014) and turbulent boundary layers (Choi *et al.* 2011) and vortex shedding manipulation (Nati *et al.* 2013; Munday & Taira 2013; Kotsonis *et al.* 2014). Separated flow controlled by means of DBD plasma actuation also already gave interesting results on geometries as the inclined flat-plate (Greenblatt *et al.* 2012), airfoils (Post & Corke 2004; Corke *et al.* 2011; Jukes *et al.* 2012) and cylinders (Thomas *et al.* 2006; Jukes & Choi 2009; Benard & Moreau 2013).

DBD plasma actuators are made of two electrodes asymmetrically placed on each side of a dielectric material as schematically shown in figure 1*a)*. They present, among others, the advantage of not having any moving parts making them potentially more robust than other types of actuators. By applying a high-frequency, alternating-current (AC) high-voltage signal between the electrodes a plasma region is formed on the surface of the dielectric. This plasma is a consequence of accelerated electrons which ionise the surrounding medium: repulsion of ions during the ionisation process induce momentum similar to a wall jet which is called the electric wind. The electric wind induced by DBD plasma actuators has previously been investigated in the case of actuators placed on a flat surface (Forte *et al.* 2007; Kotsonis *et al.* 2011). For a more detailed review of both the mechanism of DBD plasma actuators and their applications, the reader is referred to review articles by Moreau (2007) and Corke *et al.* (2010).

In the present study a half-cylinder bump has been chosen as a generic model of the rounded A-pillar corner of a truck and the capability of DBD plasma actuators to delay separation and reduce the drag in the case of a separated boundary layer on the cylindrical 2D bump is investigated. A parametric study is conducted on the location of the actuator but also on the driving voltage to optimize drag reduction. Additionally, a study of the electric wind produced by a single DBD plasma actuator in quiescent air on top of a cylinder

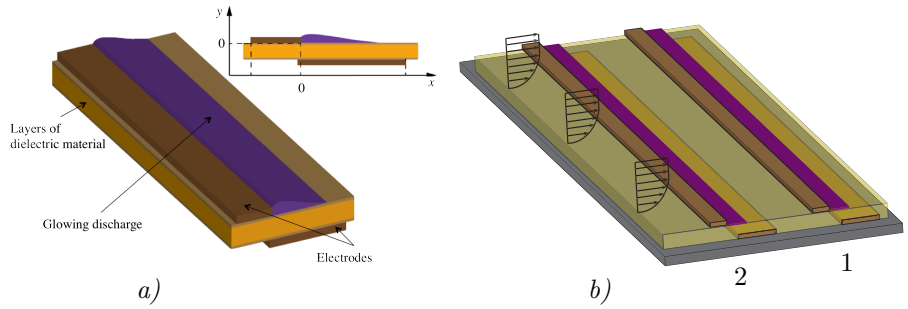

FIGURE 1. *a)* Schematic of a single DBD plasma actuator (thickness of the electrodes and dielectric material have been emphasized for clarity). *b)* Schematic of a double DBD plasma actuator mounted on a flat plate (with embedded grounded electrode) and numbering of the plasma actuators according to the flow direction; Actuator 1 is the downstream actuator, Actuator 2 is the upstream actuator.

is carried out whereby the relative location between the actuator and measurement plane is varied by rotating the cylinder to get insight into the development of the produced wall jet. The obtained experimental database is also utilized in a companion numerical project with the aim of calibrating a model for the body force induced by DBD plasma actuators (Futrzynski *et al.* 2013).

2. Experimental setup and measurement techniques

2.1. *In-house built DBD plasma actuators and electrical arrangements*

The in-house built DBD plasma actuators used for this study were manufactured using 66 microns thick copper tape for the rectangular electrodes. Previous work, among others Enloe *et al.* (2004), showed that the important geometric parameters for the electrodes concerning the efficiency of the actuators were the thickness of the exposed electrode that should be kept as thin as possible and the width of the grounded electrode that should be wide enough (in the streamwise, *i.e.* x, direction; *cf.* figure 1*a)*) not to limit the expansion of the plasma; the later can only develop on the dielectric surface where the grounded electrode is present below. Here, the grounded electrode was 8 mm wide thereby ensuring that the plasma expansion was self-limited. A small overlap of about 0.5 mm was kept between the electrodes to induce a more homogeneous plasma along the actuator length (in the spanwise, *i.e.* z, direction) as suggested by Post & Corke (2004). The electrodes were overlapping along 0.14 m in the spanwise direction for the study of the electric wind in quiescent air and along 0.26 m for the separation control study. The dielectric sheet was made of different layers of polyimide and polytetrafluoroethylene (PTFE) tape

with a nominal total thickness of 434 microns for the electric wind study and 396 microns for the separation control study.

In a proof-of-concept study it was found that a single DBD actuator worked to some extent but only gave a moderate control effect on the separation and in order to achieve a stronger effect (*cf.* Appendix), a double DBD actuator was used for the flow separation control study. The double actuator consists of simply two single actuators mounted in tandem as can be seen in figure 1*b)*. Special care was taken to build this actuator and ensure that no plasma was induced between the exposed electrode of Actuator 1 and the grounded electrode of Actuator 2. As discussed in Forte *et al.* (2007), this would induce an electric wind in the opposite direction and would therefore decrease the efficiency of the double DBD actuator. A gap of 6 mm between the grounded electrode of Actuator 1 and the exposed electrode of Actuator 2 was found to be sufficient to avoid a counter-directional electric wind.

For both studies the AC high-voltage was provided to the single or double plasma actuator using a high-voltage generator of type *Minipuls2* (*GBS Elektronik*). This generator was connected to a laboratory low-voltage generator and fed the exposed electrodes of the actuators with a high-frequency sine-like wave with an amplitude of several kilo Volts. A high-voltage probe (*Pintek Electronics HVP-39PRO*) connected to an oscilloscope (*Tektronix TDS 2014C*) was used to measure the sine-wave amplitude and frequency between the high-voltage generator and the exposed electrodes. Peak-to-peak driving voltages (V_d) between 6 and 10 kV_{p-p} with a driving frequency (f_d) of 6 kHz were tested.

2.2. *Setup of the electric-wind experiment*

Since the geometry of a half-cylinder has been selected for the flow separation control study, first the electric wind induced by a single DBD plasma actuator placed at the apex of a Plexiglas cylinder as shown in figure 2, has been measured. The cylinder was placed in a large Plexiglas box to be able to measure only the airflow induced by the actuator and limit disturbances from the surroundings.

Laser Doppler Velocimetry (LDV) was employed to record the electric wind velocity using a single-component Dantec Dynamic LDV FlowLite system with a BSA 60 processor. The measurement volume is created by the intersection of two 632.8 nm wavelength laser beams. The nominal focal length of the laser optics is 160 mm and the part of the box separating the laser head from the plasma actuator was built in glass in order to minimize optical distortions. The resulting ellipsoidal measurement volume was 0.08 mm in the diameter and 0.64 mm long. As seeding particles, diethylhexylsebacate (DEHS) droplets with a nominal diameter of about 1 μm were produced by a twin-fluid atomizer, and are continuously fed into the box, which was emptied and cleaned from particles

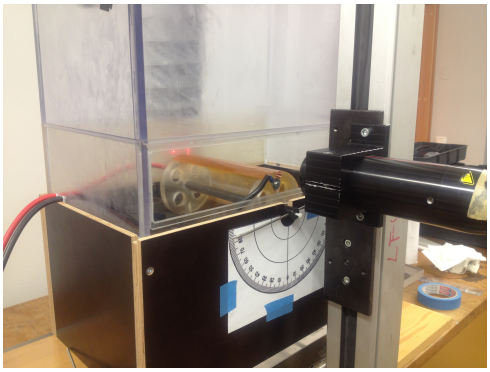

FIGURE 2. Photograph of the setup for the electric wind measurements.

after each wall-normal profile measurement. The relaxation time of the DEHS particles is estimated to be around 2 μs allowing the particles to follow flow oscillations to frequencies higher than 10 kHz with a particle response of 99% (Albrecht *et al.* 2003).

The LDV laser head was mounted to a vertical axis of an ISEL C142-4 traversing system that could be controlled with the measurement software. The cylinder could be rotated around its centre in order to change the angular position of the actuator. Then, by recording the wall-normal velocity profile, *i.e.* azimuthal component, at the apex of the cylinder using the vertical traversing system for different angular positions of the actuator, the downstream development of the electric wind could be mapped.

2.3. *Setup of the separation control experiment*

The separation control experiments were conducted in the NT2011 open-circuit wind tunnel of the Fluid Physics Laboratory, at KTH Mechanics. The test section is 1.5 m long with a cross-sectional area of 0.5 m $\times$ 0.4 m (height $\times$ width). The chosen flow case is a turbulent boundary layer developing upstream a two-dimensional (2D) cylindrical bump. The boundary layer separates while passing over the bluff body and reattaches on the flat plate downstream (see figure 3 for a schematic of the setup). The 20 mm thick Plexiglass plate is 1.5 m long, 0.4 m wide and was mounted 0.2 m above the bottom wall of the test section allowing access for the pressure tubings and electric cables from below. Tripping tape and a wire are fixed on the elliptic leading edge of the plate to trigger transition and fix the transition location of the boundary layer. The wire has a diameter of 0.26 mm and was fixed along the spanwise direction at a height of approximately 0.5 mm. *DYMO* tape, also along the spanwise direction, with the letter "V" (apex oriented in the flow direction), is placed

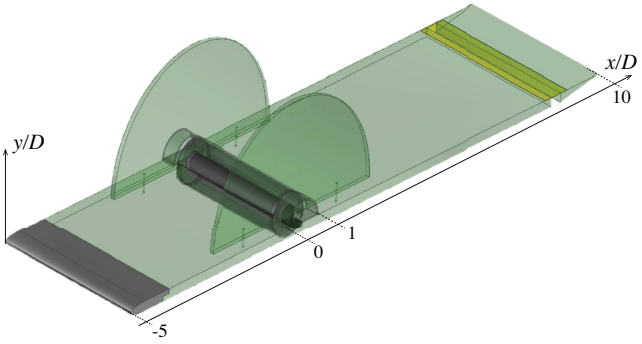

FIGURE 3. Sketch of the setup used in the open-circuit wind-tunnel for the separation control experiments.

downstream the wire to break down possible vortex shedding induced by the wire.

Although the bluff body was chosen to be a half cylinder, it was constructed from a full cylinder that enabled a change in the position of the double DBD plasma actuator by rotating the cylinder around its centre in a similar manner as for the electric wind measurements. A 0.1 m diameter (D) cylinder is thus mounted 0.5 m downstream the leading edge of the plate in a way that its axis is at the same level than the top surface of the flat plate to get a half-cylindrical bump protruding out from the plate. The embedded electrodes were first taped on the Plexiglas cylinder in the spanwise direction and the dielectric sheet was covering the entire surface of the cylinder to avoid that the dielectric created a step that could modify the flow behaviour. As can be seen in figures 4 and 5, the downstream edge of the downstream actuator exposed electrode – henceforth denoted as Actuator 1 – is at the angle θ from the leading edge of the cylinder. The downstream edge of the upstream actuator exposed electrode – Actuator 2 – is at the position $\theta - 20°$. Rectangular end plates made of Plexiglas were mounted on each side of the active part of the double actuator (separated by 0.26 m) in order to improve the two-dimensionality of the flow. To avoid abrupt changes in the spanwise direction, dummy half-cylinders with a radius of 0.05 m were placed between the end-plates and the test-section walls.

Constant-temperature hot-wire anemometry was used to perform streamwise velocity measurements of the baseline, *i.e.* uncontrolled, case at $x/D = -2.5$, as indicated in figure 4*b)*, in order to document the turbulent boundary layer approaching the cylindrical bump. The prongs of the in-house built hot-wire probe can be seen in figure 6*a)*, where it is also illustrated how the wall position was determined through the "mirror image technique" (Örlü *et al.* 2010). The hot-wire itself was a 2.5 microns diameter tungsten wire with a

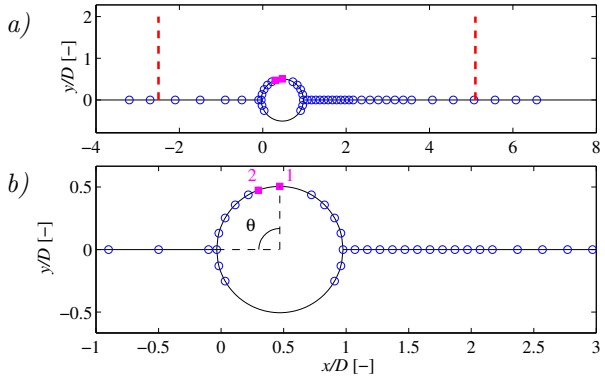

FIGURE 4. Sketch of the setup used for the separation control study. Flow is from left to right. The blue symbols represent the position of the pressure taps. The two magenta squared symbols indicate the location of the plasma actuators. The red dashed lines in *a)* are the upstream and downstream positions at which hot-wire and pressure measurements have been conducted to obtain the velocity profiles. *b)* is a close-up view of *a)*, Actuator 1 is the downstream actuator, and Actuator 2 is the upstream actuator.

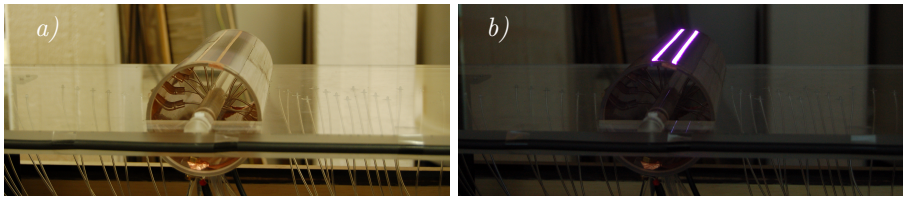

FIGURE 5. Pictures of the double actuator mounted on the top of the cylinder. *a)* actuators OFF, *b)* actuators ON. Flow is from the left to the right.

length of 0.75 mm and was welded to the tip of the prongs. To allow traversing in the vertical direction, the hot-wire probe was mounted at the bottom of a sting attached to a traversing system that was fixed on the roof of the test section. Traversing was performed using a lead screw traverse driven by a stepper motor yielding a minimum step size of around 2 microns. The calibration was performed *in situ* in the free stream at the inlet of the test section against a Pitot-static tube connected to a micro manometer of type *Furness Controls Limited FC012* (full scale 2 kPa), which was also used to monitor the free-stream velocity during the experiments. The hot-wire anemometer system used is a *Dantec StreamLine* 90N10 frame in conjunction with a 90C10 constant

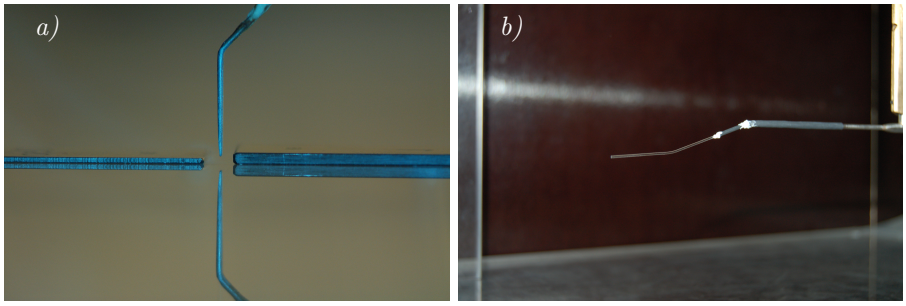

FIGURE 6. *a)* Photograph of the in-house built hot-wire used with the "mirrored image technique" (Örlü *et al.* 2010) employed to find the wall position using 0.5 mm and a 1 mm gauge heights. *b)* Photograph of the glass-Pitot tube used for total pressure measurements in the wake of the cylinder. Flow is from left to right.

temperature anemometer module operated at a resistance overheat of 80%. In order to avoid aliasing an in-built analog low-pass filter was set up with 10 kHz cut-off frequency prior to the data acquisition, with a sampling frequency and time of 20 kHz and 20 to 40 sec, respectively, the latter depending on the wall-normal position.

Both for the controlled and uncontrolled cases, the streamwise evolution of the static pressure at the wall was measured using 46 pressure taps: 7 on the flat plate upstream the cylinder, 25 downstream the cylinder and 14 pressure taps on the cylinder as depicted in figure 4. The number of pressure taps on the cylinder was limited by the presence of the double actuator but their position could be varied by rotating the cylinder and only 8 taps at a time were exposed to the flow. The pressure taps were connected through vinyl tubings to a 48 channels mechanical *Scanivalve*. The pressure from the *Scanivalve* was read by a high accuracy *MKS 120S Baratron* pressure transducer (full scale 10 Torr) against the atmospheric pressure with a sampling time of 8 to 14 sec depending on streamwise position.

The measured static wall pressure data were used to evaluate the evolution of the pressure coefficient at the wall defined as

$$C_p = \frac{p_i - p_1}{\frac{1}{2}\rho U_0^2} \,,$$

where p_i denotes the static pressure at the pressure tap number i, hence p_1 is the pressure at the most upstream pressure taps ($x/D = -3.2$), ρ is air density and U_0 is the free-stream velocity monitored by the Pitot-static probe at the inlet of the test section. For the present experiment, the free-stream velocity was set to $U_0 = 5$ m/s, yielding a Reynolds number based on D of $Re_D = 33000$.

Total, but also static, pressure measurements were measured in the wake of the cylinder, since it was observed that the static pressure profile was not uniform downstream the re-attachment point. The same traversing system as for the hot-wire measurements was used to traverse the pressure probes in the wall-normal direction. The pressure from both tubes was also read by the high accuracy *MKS 120S Baratron* pressure transducer against the atmospheric pressure with a sampling time of 32 sec. A glass capillary tube with an inner diameter of 0.56 mm was used as a total pressure tube (see figure 6) in order to make measurements close to the DBD plasma actuator without igniting sparks between the actuator and the probe. Once no risk of spark had been ensured at the position downstream the reattachment point ($x/D = 5$), a Pitot-static probe could be used to record the static pressure variations along the wall-normal direction.

The drag (D_x) on the upper side of the plate (including skin-friction drag on the flat plate and cylinder surfaces as well as the pressure drag on the cylinder), from the start of the plate (denoted by subscript 0) to a chosen cross-sectional position (denoted by subscript 2, here chosen as $x/D = 5$) is calculated according to

$$\frac{D_x}{q_0} = \int_{A_2} \frac{p_{tot,0} - p_{tot,2}}{q_0} dA - \int_{A_2} \left(1 - \frac{U_2}{U_0}\right)^2 dA \,,$$

where $q_0 = \frac{1}{2}\rho U_0^2$ is the dynamic pressure at the inlet, $p_{tot,0}$ and $p_{tot,2}$ are the total pressures at the inlet and the downstream position, and U_0 and U_2 are the corresponding streamwise mean velocity components. A_2 is the area at the downstream position, which stretches from the wall to the undisturbed free stream. This expression was derived from Maskell (1972) and can be found in Onorato *et al.* (1984). Since the flow here is assumed two-dimensional it is sufficient to do the integration in the direction normal to the plate, from the wall ($y = 0$) to some position y_2 far away from the plate. The drag per unit span (d_x) then becomes

$$\frac{d_x}{q_0} = \int_0^{y_2} \frac{p_{tot,0} - p_{tot,2}}{q_0} dy - \int_0^{y_2} \left(1 - \frac{U_2}{U_0}\right)^2 dy \,,$$

and we denote the drag coefficient as

$$C_d = \frac{d_x}{q_0(D/2)} \,,$$

i.e. where the normalisation of C_d is made with the height of the bump.

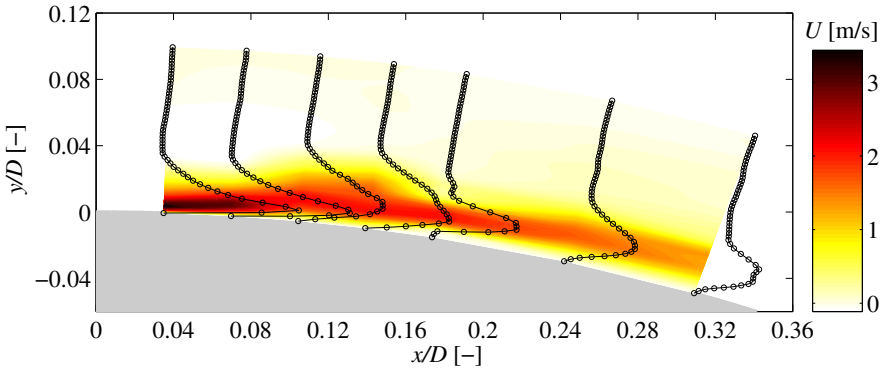

FIGURE 7. Contour plot of the mean electric wind – azimuthal component – induced by the DBD plasma actuator in quiescent air using a driving voltage of 8 kV_{p-p} at a driving frequency of 6 kHz at $\theta = 2$, 4, 6, 8, 10, 14 and 18°. The grey area represents the cylinder. The downstream edge of the actuator exposed electrode is at $x = 0$ mm, $y = 0$ mm.

3. Results

3.1. *Single DBD plasma actuator induced electric wind*

The results from the LDV measurements of the electric wind are presented in this section. The downstream evolution of the azimuthal mean velocity profiles of the induced electric wind of the in-house built single DBD plasma actuator can be observed in figure 7 for a driving voltage (V_d) of 8 kV_{p-p} and a driving frequency (f_d) of 6 kHz. The position $\theta = 0°$ ($x = 0$, $y = 0$) denotes the position of the downstream edge of the exposed electrode. The first profile is evaluated at $\theta = 2°$ in order not to perform measurements in the region of the plasma, thus to avoid errors induced by a possible effect of the plasma on the particle path or the Doppler shift value of the laser used for the LDV. It can be seen that the plasma actuator is able to produce electric winds forming wall jets with velocities of several meters per seconds; exceeding 3 m/s. As anticipated, the profile closest to the actuator exhibits the highest amplitude of the azimuthal velocity component and the wall jet appears to expand slightly in the wall-normal direction due to entrainment of the surrounding air and the amplitude of the velocities is thus decreasing due to momentum conservation. The wall jet also reduces in strength due to losses from surface friction and the adverse gradient created by the curvature but it is still detectable with velocities up to 1.2 m/s for the profile recorded at $\theta = 18°$. Moreover, the electric wind is found to follow the surface of the cylinder, which Thomas *et al.* (2006) named a Coanda-like effect, and can be seen as an advantage for separation control here.

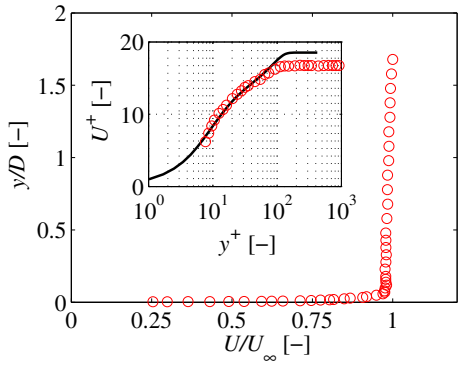

FIGURE 8. Mean streamwise velocity component at the position $x/D = -2.5$ for the uncontrolled case, in both outer and in inner scale (inserted plot). The black line in the inner-scale plot represents the DNS data from Spalart (1988).

3.2. *Baseline case of the separation control study*

The streamwise velocity profile upstream the cylinder at the position $x/D = -2.5$, depicted in figure 4*a)*, was measured to document the inflow profile approaching the cylinder. The mean velocity profile is shown in figure 8 in both outer and inner units. In absence of an established logarithmic law, where the classical Clauser chart method (Clauser 1956) could be applied, the friction velocity (u_τ) has been deduced from a fit to a law of the wall description as outlined in Örlü *et al.* (2010). The Reynolds number based on the momentum-loss thickness (Re_θ) was found to be equal to 200, and Direct Numerical Simulation (DNS) data from Spalart (1988) with $Re_\theta = 300$ were used for comparison. It is worth noting that the Reynolds number obtained here matches the critical Reynolds number for a flat plate boundary layer (*i.e.* 520 based on the displacement thickness, see *e.g.* Schlichting 1979) and is lower than the values given in Fernholz & Finley (1996) for the minimum Reynolds number for sustained turbulence; however, its existence was there coupled to the presence of a logarithmic region, which is not a necessary criterion. The utilised tripping via a trip wire ensured, however, that the boundary layer transitioned as evident from its shape factor ($H_{12} = 1.7$).

The evolution of the pressure coefficient C_p along the flat plate and on the cylinder was measured for the uncontrolled case and is shown together with the streamwise mean velocity profile at $x/D = 5$ in figure 9. The C_p evolution shows that the flow has a nearly zero pressure gradient followed by an adverse pressure gradient (APG) upstream the cylinder. As the flow evolves from the leading edge of the half-cylinder, the change of curvature induces a strong favorable pressure gradient (FPG) followed by a strong APG. The

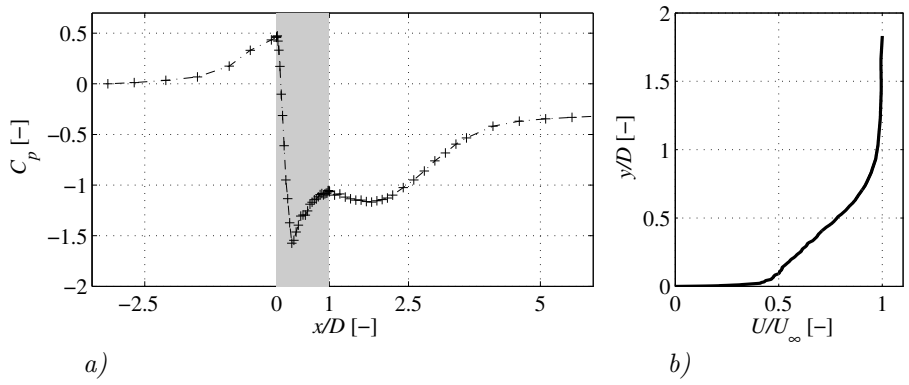

FIGURE 9. *a)* C_p profile along the flat plate and on the cylinder (cylinder is represented by the grey area) for the uncontrolled case. *b)* Streamwise component of the velocity profile downstream the cylinder for the uncontrolled case ($x/D = 5$).

latter is causing the boundary layer of the flow to separate from the cylinder surface and a wake is clearly visible downstream the cylinder. The separation point – although its exact location is hardly discernible from the wall-static pressure measurements – is estimated to be close to 105°. The FPG caused by the presence of the flat plate downstream the cylinder causes the flow to reattach. It can be seen in the velocity profile at the $x/D = 5$ station, shown in figure 9*b)*, that the flow reattaches to the surface of the flat plate but does not fully recover since the velocity profile does not resemble a canonical turbulent boundary layer.

3.3. *Separation control – controlled flow and drag reduction*

In this part, results on the separation control of the flow using the double DBD plasma actuator are presented. The driving voltage and driving frequency were set to 10 kV_{p-p} and 6 kHz, respectively, and the position of the actuator was varied by rotating the cylinder in an attempt to find the optimal position for the control. Results are presented in figure 10. While figure 10*a)* recalls how the angle θ for the position of the actuator is defined (*cf.* Section 2.3), figure 10*b)* shows the results of the drag coefficient C_d evaluated as described in section 2.3. It can be seen that the uncontrolled C_d is equal to 0.96 and actuation allows a decrease of the drag coefficient down to 0.66 for the case of $\theta = 95°$. The control seems to be the most effective for θ–positions of 95, 100, 110 and 115°.

The "W" shape of the curve expressing the drag coefficient as a function of the angular position of the plasma actuator, depicted in figure 10*b)*, is most probably related to the nature of the actuator, which consists of two DBD

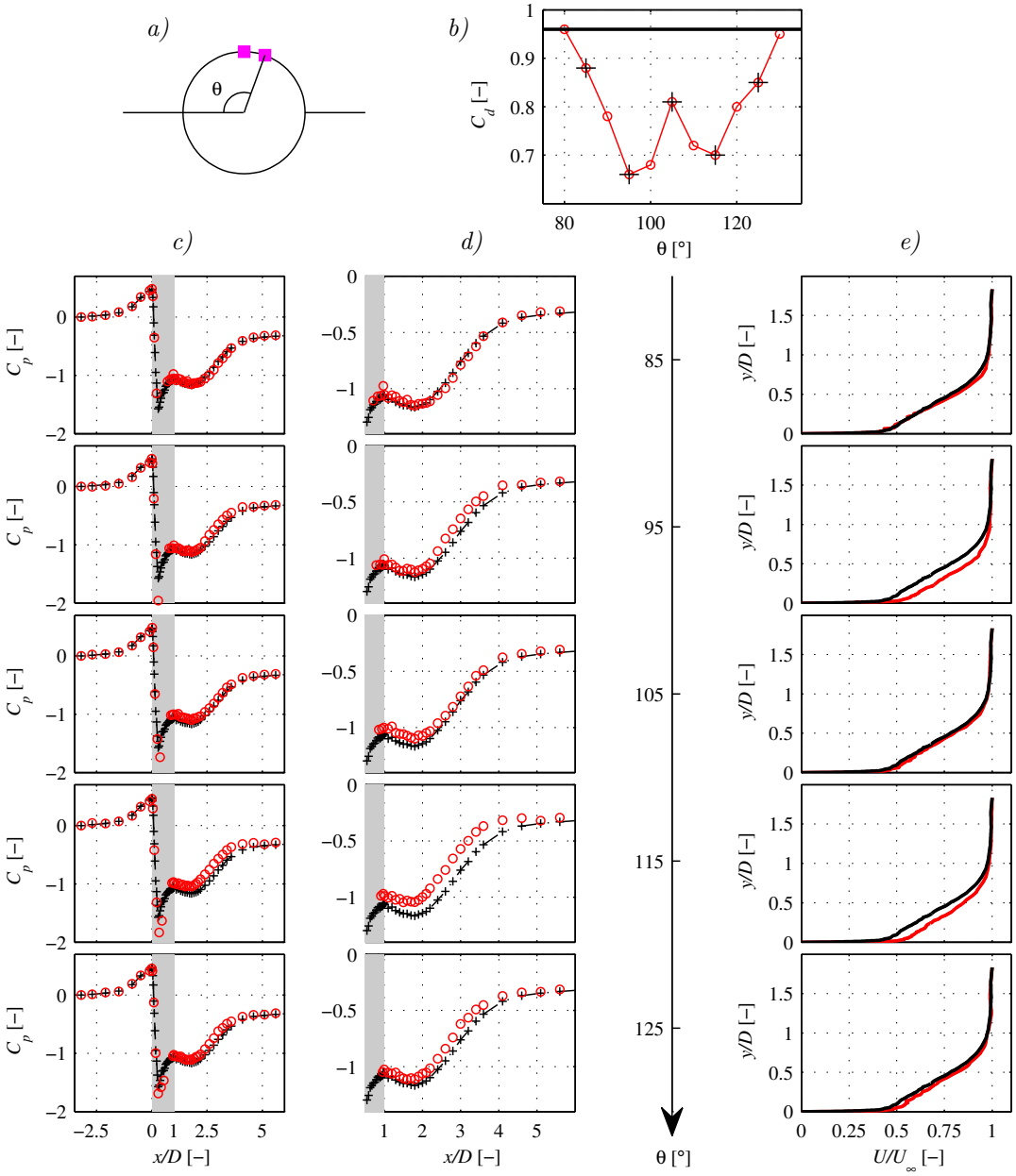

FIGURE 10. For caption, see next page.

FIGURE 10. *a)* Schematic of the cylinder and the positions of the downstream edge of the two exposed electrodes of the double DBD plasma actuator (magenta square). *b)* In red is the drag coefficient evaluated at different positions of the actuator (θ) for the controlled case, the black horizontal line corresponds to the drag coefficient of the uncontrolled flow case. The black cross corresponds to the position cases showed below in *c)*, *d)*, *e)*. *c)* Pressure coefficient upstream, on and downstream the cylinder for different θ and for the uncontrolled case (black) and controlled (red). *d)* Zoom of *c)* around the wake region. *e)* Streamwise-component velocity profile at the position $x/D = 5$ for the uncontrolled (black) and controlled (red) case. Controlled studies were realized with $V_d = 10$ kV$_{p-p}$ and $f_d = 6$ kHz.

plasma actuators, spaced by 20°. Since the most effective location for separation control is upstream and close to the separation point (Huang *et al.* 2006) – *i.e.* close to 105° for the present baseline case, *cf.* Section 3.2 – it is reasonable that the most effective locations for drag reduction due to separation delay are 95° and 115° (in that case Actuator 2 is located at 95°), in which case one of the actuators is around 9 mm upstream the separation location.

The evolution of the pressure coefficient along the plate and on the cylinder for the uncontrolled and controlled cases at different θ positions is depicted in figure 10*c)* together with a close-up of the separated region (figure 10*d)*). It can be noticed that the plasma actuation is not affecting the flow upstream the cylinder which retains the same pressure distribution in the streamwise direction as the uncontrolled case. Furthermore, the results are in accordance with those of the drag coefficient, as the base pressure for the $\theta = 95$ and 115° cases is higher than for the other cases and the length of the separation region is shorter.

Similar conclusions can also be drawn from figure 10*e)* presenting the velocity profile at the downstream position $x/D = 5$; the difference between the controlled and uncontrolled profile is noticeable for $\theta = 95$ and 115°. Comparing cases at $\theta = 85°$ and $\theta = 125°$, which both give a similar reduction of the drag coefficient – about 0.1 –, seems to show two different processes. Indeed, looking at the velocity profile for $\theta = 85°$, it is the higher part of the boundary layer – between $y/D = 0.5$ and 1 – that seems to be accelerated while it is the lower part in the case of $\theta = 125°$. Also comparing the C_p-curves for those two cases, the separation length does not seem to be affected by the control for the case at 85° while it is for the highest angle. This shows that for the low angle the double DBD plasma actuator is probably placed too much upstream the separation point in order to affect the separation. Although it was shown that

the electric wind was able to follow the surface of the cylinder in still air, it is here probably separating from the surface together with the boundary layer but still adds streamwise momentum to the flow. Hence, the apparent drag is reduced because the velocity of the measured downstream profile is higher than for the uncontrolled case, but the actuation is not affecting the separation region.

In the case of the higher angle, *i.e.* $\theta = 125°$, the plasma actuation is at a position that affects the separation, the base pressure is increased and the reattachment point is moved upstream. The measured velocity profile is thus fuller close to the wall when compared with the uncontrolled case, showing that the boundary layer has been recovering along a longer length. This can also be observed for the case $\theta = 115°$ for which the increase of the base pressure and the decrease of the separation length is much more important than for the case $\theta = 95°$ although the latter shows a higher drag reduction.

A conclusion that can be drawn from these results is that special care should be taken while evaluating the efficiency of DBD plasma actuators, but also other control techniques, since a study of the whole separated region is necessary in order to be able to conclude on their effect.

4. Summary and future work

A proof-of-concept study has been made where DBD plasma actuators have been used for separation flow control. The case studied consists of a bluff body object (half cylinder) that is approached by a turbulent boundary layer on a flat plate, where the flow is strongly separated on the downstream side of the cylinder. The electric wind produced by the plasma actuators has been shown to be able to hamper the effects of separation and to facilitate a faster reattachment and flow recovery behind the bluff body object approached by a turbulent boundary layer on a flat plate.

A first part of the study deals with the electric wind itself, and how it interacts with the curved cylinder surface in still air. Using LDV for the velocity measurements it was shown that the produced wall jet follows the surface up to at least 18°, from the downstream edge of the exposed electrode, without separating from the surface. At a voltage of 8 kV_{p-p} the present DBD actuator can produce peak velocities above 3 m/s in the neighbourhood of the actuator.

For the flow control studies the DBD plasma actuators were mounted on the half-cylinder in the region of the separation, *i.e.* in the top region of the cylinder. In this study we used a double actuator since preliminary tests showed that a single actuator produced a limited (although positive) control effect (see Appendix).

The position of the actuation could be varied with respect to the separation point by rotating the cylinder. A parametric study of the influence of the position on the control efficiency was made and was studied through measurements

of the pressure distribution on the flat plate both upstream and downstream the cylinder as well as on the cylinder itself. There was a clear influence on the pressure distribution for the controlled cases showing a faster pressure recovery, however from this it is not possible to give quantitative information on the drag reduction.

Velocity and pressure measurements were made at $x/D = 5$ in order to check the status of the reattached boundary layer and to also evaluate the change in drag. At this position the boundary layers for both the uncontrolled and controlled cases were reattached, but there were distinct differences between the cases of successful control and the uncontrolled case. The total drag (including both friction and pressure drag) up to the point $x/D = 5$ was also determined for the different cases by integrating the total pressure and velocity profiles at $x/D = 5$. Strong effects of the control could be detected where total drag reductions of more than 30% was observed for the best actuator position. Since the evaluated drag also involves the skin friction in front of the cylinder the drag reduction due to the separation control is even larger.

The present study clearly shows the potential for separation control on curved surfaces where an adverse pressure gradient leads to boundary layer separation. However there are still many open questions whether this can be used in practice for *e.g.* flow control around the A-pillar of a truck. The present experiments were made at low velocities around the obstacle and the control efficiency at higher velocities needs to be studied. On the other hand the curvature of the cylinder in the experiment was high ($R = 50$ mm) which is higher than in a typical practical application and also the geometry itself is different and gives a more severe separation and hence the flow under investigation here is also harder to control. Future studies will be done in a similar setup in a closed-loop wind tunnel where the velocity field will be measured with particle image velocimetry which enables faster data collection of the full velocity field, not only downstream but also close to the cylinder itself. In addition we also plan experiments where plasma actuators will be used as vortex generators to produce streamwise vortices which can be used for separation control.

Acknowledgements

The work was financially supported by the Swedish Energy Agency within the project Flow Research on Active and Novel Control Efficiency (FRANCE), project number 34186-1. Per Elofsson and Guillaume Mercier of Scania AB and Gunilla Efraimsson and Romain Futrzynski from KTH Aeronautical and Vehicle Engineering (Linné FLOW Centre) are acknowledged for useful input to the project. Tomas Modéer from KTH Electrical Energy Conversion, is greatly acknowledged for his help with the electrical setup.

Appendix. Influence of driving voltage and single versus double actuator

In this Appendix we illustrate the influence of the driving voltage as well as the difference between a single and a double actuator on the control efficiency.

Figure 11 shows a comparison of the induced electric wind for two different driving voltages V_d, 6 kV_{p-p} and 8 kV_{p-p} both with $f_d = 6$ kHz. It is clear that increasing the driving voltage of the actuator increases the electric wind velocity. The highest amplitude of the azimuthal component of the velocity is almost doubled in the case of $V_d = 8$ kV_{p-p} compared to the 6 kV_{p-p} case. Moreover, the low-voltage induced electric wind contains less momentum from the beginning, thus the wall jet amplitude is more sensible to the adverse pressure gradient and friction losses at the wall and is almost not visible anymore at the most downstream station ($\theta = 18°$). This result implies that the control action is probably stronger as the driving voltage is increased since the induced electric wind velocity is higher and furthermore that the region of action – downstream the actuator – is wider for higher voltages as the wall jet is sustained for longer distances.

In the flow control study the angle $\theta = 95°$ showed the largest difference in the velocity profile at the streamwise position $x/D = 5$ between the uncontrolled and controlled case, and this position was chosen as the fixed position to test how the amplitude of the applied voltage affects the flow control. Results using lower voltages – $V_d = 6$ and 8 kV_{p-p} – can be compared to the previous

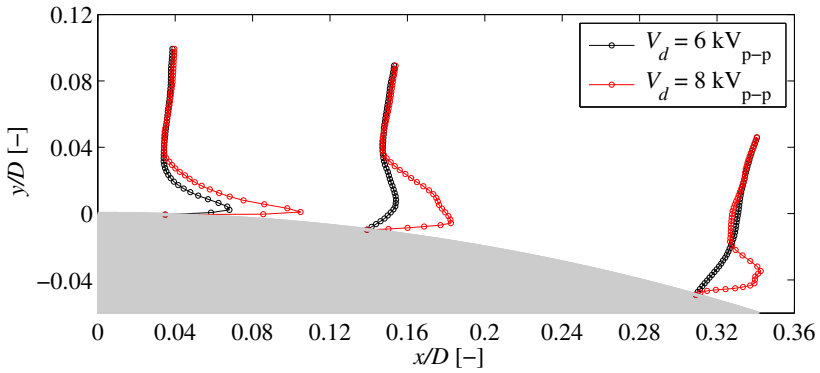

FIGURE 11. Mean flow profiles – azimuthal component – of the electric wind induced by the DBD plasma actuator in quiescent air using a driving voltage of 6 kV_{p-p} and 8 kV_{p-p} at a driving frequency of 6 kHz at $\theta = 2$, 8 and 18°. The grey area represents the cylinder. The downstream edge of the actuator exposed electrode is at $x = 0$ mm, $y = 0$ mm.

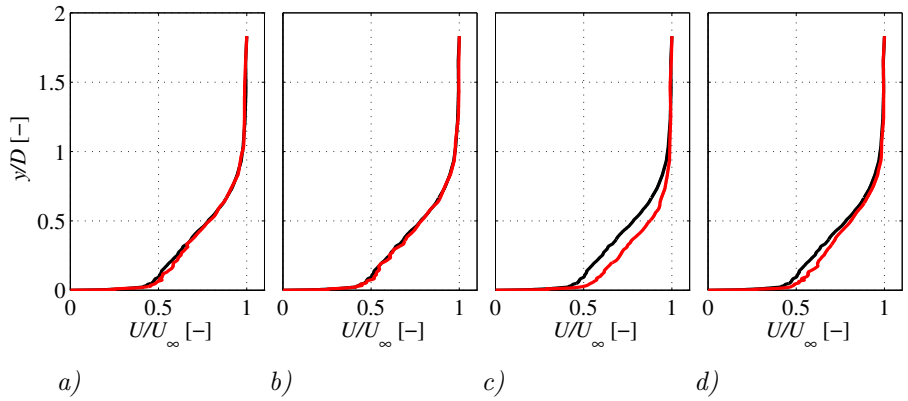

FIGURE 12. Comparison of the uncontrolled (black) and controlled (red) streamwise velocity profile at position $x/D = 5$ with $f_d = 6$ kHz and *a)* $V_d = 6$ kV$_{p-p}$, *b)* $V_d = 8$ kV$_{p-p}$, *c)* $V_d = 10$ kV$_{p-p}$, *d)* $V_d = 10$ kV$_{p-p}$, where *d)* corresponds to a single DBD plasma actuator.

results with $V_d = 10$ kV$_{p-p}$ in figure 12*a–c)*. As can be seen it seems that effect on the separation for the lower voltages is almost negligible if judged from the mean velocity distribution at $x/D = 5$. This shows that one needs a certain threshold amplitude to obtain a substantial control effect.

The difference between the single and double actuators can be seen in figure 12*c–d)*. Although both cases show an effect, it is clear that the control effect of the double actuator is substantially stronger.

References

Albrecht, H.-E., Borys, M., Damaschke, N. & Tropea, C. 2003 *Laser Doppler and phase Doppler measurement techniques*. Springer.

Barnard, R. H. 2009 *Road vehicle aerodynamic design*, 3rd edn. MechAero Publishing.

Benard, N. & Moreau, E. 2013 Response of a circular cylinder wake to a symmetric actuation by non-thermal plasma discharges. *Exp. Fluids* **54** (2), 1467.

Choi, K. S., Jukes, T. N. & Whalley, R. D. 2011 Turbulent boundary-layer control with plasma actuators. *Philos. T. Roy. Soc. A* **369** (1940), 1443–1458.

Clauser, F. H. 1956 The turbulent boundary layer. In *Advances in applied mechanics* (ed. H. L. Dryden & T. von Kármán), pp. 1–51. Academics Press Inc.

Corke, T. C., Bowles, P. O., He, C. & Matlis, E. H. 2011 Sensing and control of flow separation using plasma actuators. *Philos. T. Roy. Soc. A* **369** (1940), 1459–1475.

Corke, T. C., Enloe, C. L. & Wilkinson, S. P. 2010 Dielectric barrier discharge plasma actuators for flow control. *Annu. Rev. Fluid Mech.* **42**, 505–529.

Duchmann, A., Grundmann, S. & Tropea, C. 2013 Delay of natural transition with dielectric barrier discharges. *Exp. Fluids* **54** (3), 1461.

Enloe, C. L., McLaughlin, T. E., Van Dyken, R. D., Kachner, K. D., Jumper, E. J., Corke, T. C., Post, M. L. & Haddad, O. 2004 Mechanisms and responses of a dielectric barrier plasma actuator: Geometric effects. *AIAA J.* **42**, 595–604.

Fernholz, H. H. & Finley, P. J. 1996 The incompressible zero-pressure-gradient turbulent boundary layer: An assessment of the data. *Prog. Aerosp. Sci.* **32**, 245–311.

Forte, M., Jolibois, J., Pons, J., Moreau, E., Touchard, G. & Cazalens, M. 2007 Optimization of a dielectric barrier discharge actuator by stationary and non-stationary measurements of the induced flow velocity: application to airflow control. *Exp. Fluids* **43**, 917–928.

Futrzynski, R., Efraimsson, G. & Alfredsson, P. H. 2013 Numerical simulation of a plasma actuator on a half-submerged cylinder. In *Proc. of the Int. Conf. on Jets, Wakes and Separated Flows, ICJWSF-2013*. Nagoya, Japan.

Greenblatt, D., Schneider, T. & Schüle, C. Y. 2012 Mechanism of flow separation control using plasma actuation. *Phys. Fluids* **24**, 077102.

Grundmann, S., Klumpp, S. & Tropea, C. 2007 Experimental and numerical investigations of boundary-layer influence using plasma-actuators. In *Active flow control, notes on numerical fluid mechanics and multidisciplinary design (nnfm)* (ed. K. R), pp. 56–68. Springer Berlin Heidelberg.

Hanson, R. E., Lavoie, P., Naguib, A. M. & Morrison, J. F. 2010 Transient growth instability cancelation by a plasma actuator array. *Exp. Fluids* **49** (6), 1339–1348.

Huang, J., Corke, T. C. & Thomas, F. O. 2006 Plasma Actuators for Separation Control of Low-Pressure Turbine Blades. *AIAA J.* **44** (1), 51–57.

Inasawa, A., Ninomiya, C. & Asai, M. 2013 Suppression of tonal trailing-edge noise from an airfoil using a plasma actuator. *AIAA J.* **51**, 1695–1702.

Jukes, T. N. & Choi, K. S. 2009 Control of unsteady flow separation over a circular cylinder using dielectric-barrier-discharge surface plasma. *Phys. Fluids* **21** (9), 094106.

Jukes, T. N., Segawa, T., Walker, S., Furutani, H., Iki, N. & Takekawa, S. 2012 Active separation control over a NACA0024 by DBD plasma actuator and FBG sensor. *J Fluid Sci Technol.* **7**, 39–52.

Kotsonis, M., Ghaemi, S., Veldhuis, L. & Scarano, F. 2011 Measurement of the body force field of plasma actuators. *J. Phys. D: Appl. Phys.* **44**, 045204.

Kotsonis, M., Pul, R. & Veldhuis, L. 2014 Influence of circulation on a rounded-trailing-edge airfoil using plasma actuators. *Exp. Fluids* **55** (7), 1772.

Maskell, E. C. 1972 Progress towards a method for the measurement of the components of the drag of a wing of finite span. *Tech. Rep.* 72232.

Moreau, E. 2007 Airflow control by non-thermal plasma actuators. *J. Phys. D: Appl. Phys.* **40**, 605–636.

Munday, P. M. & Taira, K. 2013 On the lock-on of vortex shedding to oscillatory actuation around a circular cylinder. *Phys. Fluids* **25** (1), 013601.

Nati, G., Kotsonis, M., Ghaemi, S. & Scarano, F. 2013 Control of vortex shedding from a blunt trailing edge using plasma actuators. *Exp. Therm. Fluid Sci.* **46**, 199–210.

Onorato, M., Costelli, A. F. & Garrone, A. 1984 Drag measurements through wake analysis. *SAE Tech. Paper* p. 840302.

Örlü, R., Fransson, J. H. M. & Alfredsson, P. H. 2010 On near wall measurements of wall bounded flows – The necessity of an accurate determination of the wall position. *Prog. Aerosp. Sci.* **46**, 353–387.

Osmokrovic, L. P., Hanson, R. E. & Lavoie, P. 2014 Laminar boundary-layer response to spanwise periodic forcing by dielectric-barrier-discharge plasma-actuator arrays. *AIAA J.* p. In Print.

Post, M. L. & Corke, T. C. 2004 Separation control on high angle of attack airfoil using plasma actuators. *AIAA J.* **42** (11), 2177–2184.

Roth, J. R., Sherman, D. & Wilkinson, S. 1998 Boundary layer flow control with a one atmosphere uniform glow discharge surface plasma. In *36th AIAA*

Aerospace Sciences Meeting and Exhibit. Reno, N.V., USA: American Institute of Aeronautics and Astronautics.

Schlichting, H. 1979 *Boundary-layer theory*, 7th edn. McGraw-Hill.

Spalart, P. R. 1988 Direct simulation of a turbulent boundary layer up to $R_\theta = 1410$. *J. Fluid Mech.* **187**, 61–98.

Thomas, F. O., Kozlov, A. & Corke, T. C. 2006 Plasma actuators for bluff body flow control. In *3rd AIAA Flow Control Conference*. San Francisco, California: American Institute of Aeronautics and Astronautics.

Thomas, F. O., Kozlov, A. & Corke, T. C. 2008 Plasma actuators for cylinder flow control and noise reduction. *AIAA J.* **46** (8), 1921–1931.